UNDERSTANDING CRYSTALLOGRAPHIC DEFECTS IN HARD MATERIALS;

A STUDY IN ECCI AND EBSD

by Brooke Matat Jablon

University of Strathclyde

A thesis submitted to

The Department of Physics

University of Strathclyde

For the degree of

Doctor of Philosophy

April 20th, 2020

Declaration of Authenticity and Author's Rights

This thesis is the result of the author's original research. It has been composed by the author and has not been previously submitted for examination which has led to the award of a degree.

Signed: Date:

Abstract

This thesis investigates the crystallographic defects inherent in two hard materials, tungsten carbide embedded in a cobalt matrix (WC-Co) and diamonds. The scanning electron microscopy (SEM) techniques of electron channelling contrast imaging (ECCI), cathodoluminescence (CL) imaging and electron backscatter diffraction (EBSD) allowed for the investigation of the crystallographic defects.

Initial work on WC identified the dislocations and subgrain structures in grains of known crystallographic orientation. By combining ECCI and EBSD, new insights into the microstructure of WC grains were revealed. The advantage of using these techniques over the more common TEM based techniques is that ECCI and EBSD allow for analysis over a large field of view, in this case 75 μm × 75 μm. These large scale analyses reveal the microstructure and misorientation and dislocations throughout an entire WC grain. ECCI exposed dislocations while EBSD data revealed small changes in crystallographic orientation resulting from dislocations and subgrains, thereby corroborating the ECCI data.

Further investigation of dislocations in WC categorized the type of dislocations found in grains of known crystallographic orientation using ECCI and EBSD. Dislocations and their Burgers vectors are described. The type of dislocations found in a particular grain are discussed in relation to their orientation with respect to neighbouring grains. Using ECCI and EBSD to categorize dislocations in the basal and prismatic planes helps explain how WC grains deform plastically.

Plastic deformation is studied by indenting WC grains and studying the damage with ECCI and EBSD analysis. Misorientation surrounding the indent is investigated by EBSD for two different indenter tips. Using ECCI to reveal slip

bands around indents in grains exposes different defects and deformation depending on the crystallographic orientation of grains. This novel ECCI work agrees with previous TEM data on slip systems in indented WC grains. Using ECCI presents an advantage over TEM in this case in that damage in grains can be imaged over a wider field of view with simpler sample preparation.

The characterization of twinned gem-quality diamonds, also known as macles, using ECCI, EBSD and CL reveals that twinned diamonds are all composed of two sibling twins with around 180° between the siblings. CL is helpful in understanding the initial twin nucleation and distinct periods of crystallization in the diamond's history while EBSD is used to corroborate CL. This study shows that the twinning plane is not linear, but jagged, corroborating previous research indicating that these are not true contact twins, rather they contain some intergrowths. EBSD confirms that these are undeniable twins as the plane separating the two siblings is a twin Coincident Site Lattices (CSL) grain boundary. CL and EBSD together are powerful tools for characterizing the twinning plane and growth mechanism in diamonds and this work describes the novel use of these techniques to understand diamond crystallization.

Acknowledgments

I would like to thank my supervisor, Dr. Carol Trager-Cowan, for her support throughout my studies. Her insistence that I investigate every nook and cranny of this field, on my own, has made me the scientist that I am today. I am also grateful for my second supervisor, Professor Robert Martin. His calm and collected approach to academia and guidance throughout my studies was a stable force. I am also indebted to my supervisor at the National Physical Laboratory in Teddington, Dr. Ken Mingard, for his contribution to my understanding of material science. He made my visits to the national laboratory enjoyable and educational.

I am thankful to my colleagues at the University of Strathclyde for the pleasant three years that we spent together. I would also like to thank my colleagues at the Hebrew University of Jerusalem, specifically Professor Oded Navon and Dr. Omri Dvir. Without their guidance, support and encouragement over the last eight years, I would not have pursued a PhD. I will always cherish their advice and friendship.

Most importantly, I would like to thank my family. Hazel, Cari, Mya, Yaron, Arthur and Fannette shaped and moulded me over the last three decades into the person I am today. Finally, I dedicate this thesis to Pierre-Elie and Boaz, to whom I dedicate my life.

List of Publications

B.M. Jablon, K. Mingard, A. Winkelmann, G. Naresh-Kumar, B. Hourahine, C. Trager-Cowan. *Subgrain structure and dislocations in WC-Co hard metals revealed by electron channelling contrast imaging* International Journal of Refractory Metals and Hard Materials **87**

B. M. Jablon, K. Mingard, C. Trager-Cowan. *Dislocation analysis of basal and prismatic tungsten carbide grains,* in preparation

A. Winkelmann, B.M. Jablon, V. Tong, C. Trager-Cowan, K. Mingard. *Improving EBSD precision by orientation refinement with full pattern matching* Journal of Microscopy, 2020

F. De Luca, H. Zhang, V. Tong, K. Mingard, B.M. Jablon, C. Trager-Cowan, M.G. Gee, Nanomechanical behaviour of individual domains in WC-Co cemented carbides from ambient to high temperature, submitted

List of conference contributions

National Physical Laboratory (NPL) Postgraduate institute meeting-London, December 2016

Conference attendee

RMS EBSD meeting-Oxford, April 2017

Conference attendee

National Physical Laboratory (NPL) Postgraduate institute meeting-London, December 2017

Contribution of a conference poster.

RMS EBSD meeting-Plymouth, April 2018

Contribution of a conference lecture.

EMAS meeting-Bristol, August 2018

Invited speaker on cathodoluminescence in the Earth Sciences

Contribution of a conference abstract and invited lecture.

National Physical Laboratory (NPL) Postgraduate institute meeting-Glasgow, December 2018

Contribution of a conference poster.

RMS EBSD meeting-London, April 2019

Contribution of a conference poster and lecture

EMAS meeting-Trondheim, May 2019

Contribution of a conference poster

RMS EBSD meeting-Sheffield, April 2021

Contribution of a conference poster

List of abbreviations

- WC-Co: Tungsten carbide grains embedded in a cobalt matrix
- SEM: scanning electron microscopy
- TEM: transmission electron microscopy
- EBSD: electron backscatter diffraction
- EBSP: electron backscatter pattern
- ECCI: electron channelling contrast imaging
    - ECC image: electron channel contrast image (sometimes used)
- CL: cathodoluminescence
- IPF: inverse pole figure
- BSE: backscatter electrons
- SE: secondary electrons
- FIB: focused ion beam
- wt%: weight percent

Table of contents

Declaration of Authenticity and Author's Rights 2
Abstract 3
Acknowledgments 3
List of Publications 6
List of conference contributions 7
List of abbreviations 8
1.Introduction 12
1.1. Introduction 12
1.2. Introduction to hard materials 12
1.2.1. Tungsten carbide-cobalt (WC-Co) hardmetal 13
1.2.2. Twinned diamonds 16
1.3. Motivation 17
1.4. Thesis overview 18
2.Methodology 20
2.1. Introduction to crystallographic defects 20
2.1.1. Stacking faults 20
2.1.2. Grain boundaries 21
2.1.3. Twin boundaries 21
2.1.4. Dislocations 21
2.1.5.Slip 22
2.2. Materials 23
2.2.1. Tungsten carbide-cobalt (WC-Co), a hardmetal 23
2.2.2. Diamonds 26
2.3. Sample preparation 29
2.3.1. Sample preparation for WC 29
2.3.2. Sample preparation for diamond 30
2.4. Analytical techniques 31
2.4.1. SEM and EPMA 31
2.4.2. SE 32
2.4.3. BSE 32
2.4.3.1. ECCI 33
2.4.3.2. EBSD 35

2.4.4. CL 40
3.Subgrain structure and dislocations in indented tungsten-carbide cobalt 43
3.1. Introduction 43
3.2. Sample specifications and experimental details 44
3.3. Results 45
3.3.1. ECCI and EBSD 45
3.3.2. Preliminary Dislocation Observations 51
3.4. Discussion 57
3.4.1. Ramifications of sample preparation 57
3.4.2. Subgrain structure 58
3.4.3. Pattern matching 60
3.5. Summary 61
4.Dislocation analysis in basal and prismatic tungsten carbide grains 62
4.1. Introduction 62
4.2. Sample specifications and experimental details 64
4.3. Results and discussion 68
4.4. Conclusions 77
5.Crystallographic defects in indented tungsten carbide grains 78
5.1. Introduction 78
5.2. Slip plane identification in the literature 78
5.3. Sample specifications and experimental details 80
5.3.1. Choosing grains for analysis 80
5.3.2. Indenting WC grains 82
5.4. Results and Discussion 82
5.4.1. ECCI and EBSD of 0001, 1100 and 1120 oriented grains using a Berkovich indenter 82
5.4.1.1. 0001 82
5.4.1.2. 1010 87
5.4.1.3. 1120 93
5.4.2. ECCI of 0001 and 1120 oriented grains using a spherical indenter 99
5.5. Summary 101
6.Crystallographic defects in twinned, gem-quality diamonds ..... **Error! Bookmark not defined.**
6.1. Introduction 103

6.2. Sample specifications and experimental details 104
6.2.1. Choosing samples 104
6.2.2. Sample preparation 105
6.2.3. Acquiring images: ECCI, CL, EBSD 106
6.3. Twinning 107
6.3.1. The crystallography of twinning 107
6.3.2. Twinning in natural diamonds; contact twins 108
6.4. Results and Discussion 109
6.5. Summary 118
7.Conclusions 119
7.1. Techniques and materials 119
7.2. Tungsten carbide grains 119
7.2.1. Conclusions on tungsten carbide 119
7.2.2. Future work on tungsten carbide 124
7.3. Twinned diamonds 124
7.3.1. Conclusions on twinned diamonds 124
7.3.2. Future work on twinned diamonds 125
List of Figures 126
List of Tables 128
References 129

1. Introduction

1.1. Introduction

The field of electron microscopy is developing quickly and its techniques are being applied in situations for which they were not originally intended and on materials which were traditionally difficult to analyse. The goal of this project is to demonstrate how electron channelling contrast imaging (ECCI) and electron backscatter diffraction (EBSD) can be combined to provide an alternative to traditional crystallographic defect analysis using transmission electron microscopy (TEM) on materials such as hardmetals and diamond for which TEM analysis techniques have proved difficult in the past. The analysis of the defects identified using these techniques as well as the influence of these defects on their crystal lattice is also a part of this work.

In this study, tungsten carbide (WC) and naturally occurring diamonds are analysed to understand how crystallographic defects manifest themselves in two hard materials. The crystallography of these two materials and analytical techniques are discussed in chapter 2. The results chapters (3, 4, 5 and 6) categorize the defects inherent in WC and diamond and new observations are recorded.

1.2. Introduction to hard materials

Hard materials are those with resistance to localized plastic deformation. This generally reflects strong intermolecular bonds. Hardness depends on a number of factors. Two of these, plasticity and strain, will be discussed in chapters 4 and 5. Hardness can be measured by scratch tests, indentation and rebound. These three tests each reflect different characteristics of hardness. Scratch tests are commonly used in mineralogy. The Mohs scale is arranged by hardness and determined by which mineral can scratch other minerals(Britannica, 2017). The Mohs scale ranges from 1 to 10 with defining minerals at each numerical integer.

Diamond measures 10 and is the hardest mineral on the Mohs scale. WC, while not a naturally occurring mineral, is a 9.5 on the scale (TACA). Indentation tests measure deformation due to constant compression from a sharp object (Smith & Sandland, 1922). These tests measure the dimensions of indents left by a specific indenter tip. The load displacement data can then be used to determine different material characteristics like hardness and wear properties.

1.2.1. Tungsten carbide-cobalt (WC-Co) hardmetal

WC belongs to a class of materials known as hardmetals. Hardmetals are ceramic aggregates surrounded by a metal binder phase, as seen in Figure 1. Common examples of hardmetal ceramics are tungsten carbide, titanium carbide and tantalum carbide (Kurlov & Gusev, 2013). Hardmetals are known for their stiffness and hardness and are used in industries where resistance to abrasion is crucial. Stiffness is the extent to which an object resists deformation, while hardness is resistance to localized plastic deformation (Chinn, 2009; Baumgart, 2000). WC hardmetals are used for machining wood, which exposes them to intermittent high impact forces; metal machining, where high compressive strength and abrasive wear resistance is crucial; circular shearing and cutting blades, which require reliable sharp edges and in dental applications, which necessitate high wear resistance and toughness.

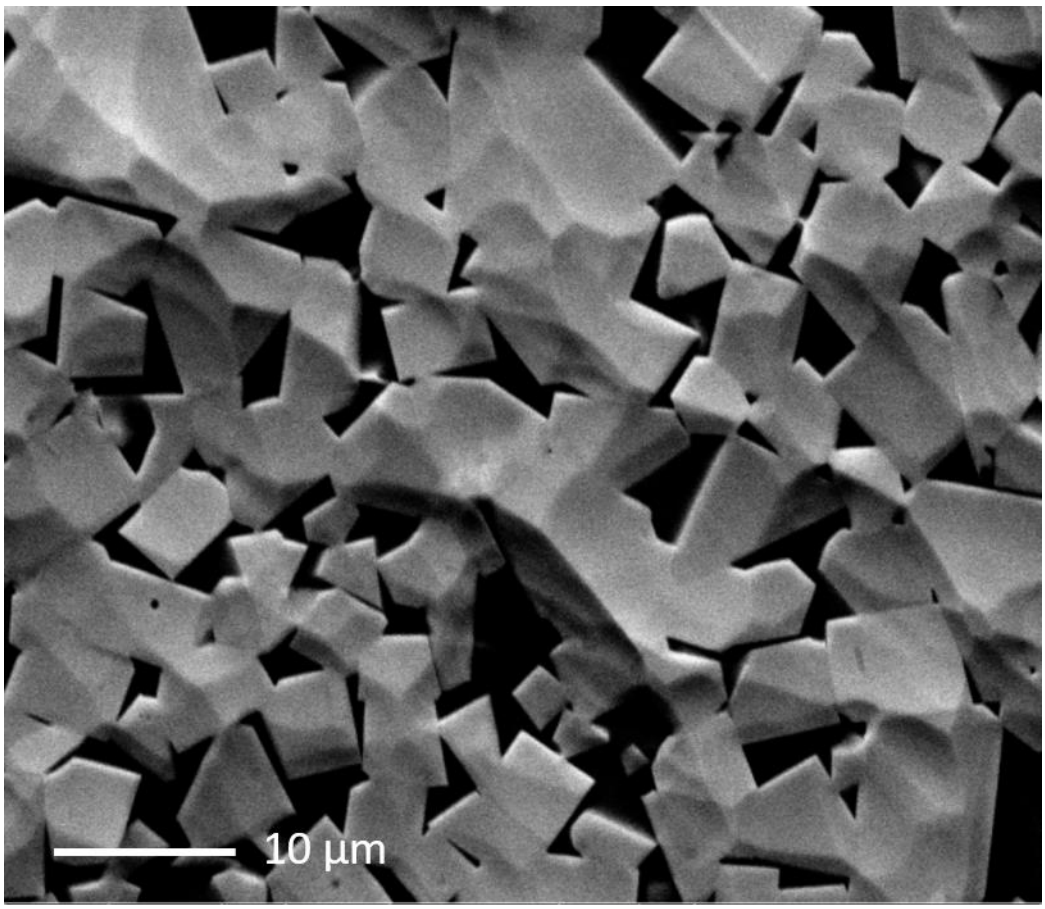

Figure 1. A backscatter electron image of WC grains (grey) embedded in a cobalt binder phase (black).

WC is used as a hard metal for its strength and wear resistance while the cobalt (Co) binder phase contributes toughness and ductility. Toughness is the ability of a material to absorb energy and plastically deform without fracturing, and ductility is the ability to deform under stress (Prakash, 1995). The toughness and hardness of WC-cobalt hardmetals can be manipulated by controlling WC grain size and cobalt concentration (Prakash, 1995). In WC-Co hardmetals, WC grain size varies from 0.3 to 40 µm and the hardmetal contains at least 3 weight percent (wt%) cobalt which comprises the skeleton (Prakash, 1995). Coarser grains, greater than 2 µm, are used in the mining industry while the metal cutting industry requires WC grains to be between 1-2 µm (Prakash, 1995). Grains of less than one micron are characterized by high abrasive wear resistance and hardness (Prakash, 1995).

WC hardmetals are synthesized using powder metallurgy and liquid phase sintering. The material is created by mixing about 90% WC powder with 10% of a binder metal, sometimes iron, nickel, cobalt or copper. The WC powder is created by reducing WO_3 and then exposing the material to a carbon-bearing material like charcoal (Roebuck & A. Almond, 1988). The WC is then milled to reduce clumps of powder particles so that the subsequent material is homogeneous in size. Alcohol is used to lubricate the WC as it is milled in stainless steel containers. The slurry is spray dried resulting in grains with a spherical shape. These grains are then pressed into their final shape at pressures between 150-990 MPa (Weidow, 2010; Porat *et al.*, 1996). Next the material is sintered to increase the density of the final product and to bind the powder grains. The binder phase, generally cobalt or nickel, is introduced into the pressed WC powder and then heated to 1300-1350° at which point liquid phase sintering begins. WC grains are dissolved into the binder phase. When the binder phase is fully saturated with WC, the WC precipitates out of solutions. WC continues to crystallize during cooling. A few atomic weight percent of WC remains dissolved in the binder phase (Weidow & Andrén, 2011).

The interaction of WC grains and the cobalt matrix affects the mechanical properties, chemistry and microstructure of the final product. WC is hexagonal while cobalt is face centred cubic in WC-Co hardmetals (Kurlov & Gusev, 2013). The crystallography of the cobalt matrix has not been widely studied, despite its influence on crystallization during sintering and its role in deformation and fracture of the final material. Crystallographic information of the cobalt is difficult to acquire because it is much softer than the WC grains and is often damaged during sample preparation.

Crystallographic defects are apparent in WC grains after sintering. Transmission electron microscopy (TEM) and X-Ray diffraction (XRD) studies show that the density and type of dislocations depends on both the grain size of the initial WC

powder and how it was initially milled. Different milling conditions lead to higher densities of dislocations and stacking faults in the final material (Lay, 2013). Studies have shown that dislocation density in metals is directly related to the principal characteristics of the material such as damage, phase transformation and recrystallization (Gutierrez-Urrutia & Raabe, 2012). Therefore, identifying the presence of dislocations and the types of dislocations in WC grains is crucial to understanding the material's characteristics.

1.2.2. Twinned diamonds

Diamond is the hardest naturally occurring substance (Fritsch, 1998). Naturally occurring gem-quality diamonds are octahedral with smooth, even faces. The octahedral habit can be distorted, reflecting stresses or dissolution during crystallization. Dissolution leads to the development of pseudo-rhombic-dodecahedral and pseudo-cubic forms. The single octahedral form represents equilibrium crystallization and a slow growth rate from a saturated medium (Sunagawa, 1984). Sometimes during the growth of monocrystalline diamonds, twinning is observed.

Twinning during crystallization can result in two different kinds of twins, contact twins and penetration twins. In the diamond industry, contact twins are called macles. Just as human identical twins start from the same egg twinned gem quality diamonds start from the same nucleus.. Using x-ray topographs, previous work has shown that twinning in macles starts at the beginning of the diamond's crystallization (Yacoot *et al.*, 1998; Machado *et al.*, 1998; Friedel, 1926). Macles are characterized by enhanced growth on the (111) planes leading to triangular crystal with two (111) dominant faces parallel to the twin plane as illustrated in Figure 2 (Yacoot *et al.*, 1998). A better understanding of their microstructure using ECCI and EBSD could elucidate the growth processes of natural diamonds. Using the same methods applied to WC grains, analysis on twinned diamonds using ECCI, cathodoluminescence imaging (CL) and EBSD

provides information on the internal microstructure of naturally-occurring, gem-quality diamond. Understanding the role of dislocations in twinning using CL, EBSD and ECCI demonstrates the power of minimally invasive techniques as an alternative for the more destructive TEM analysis.

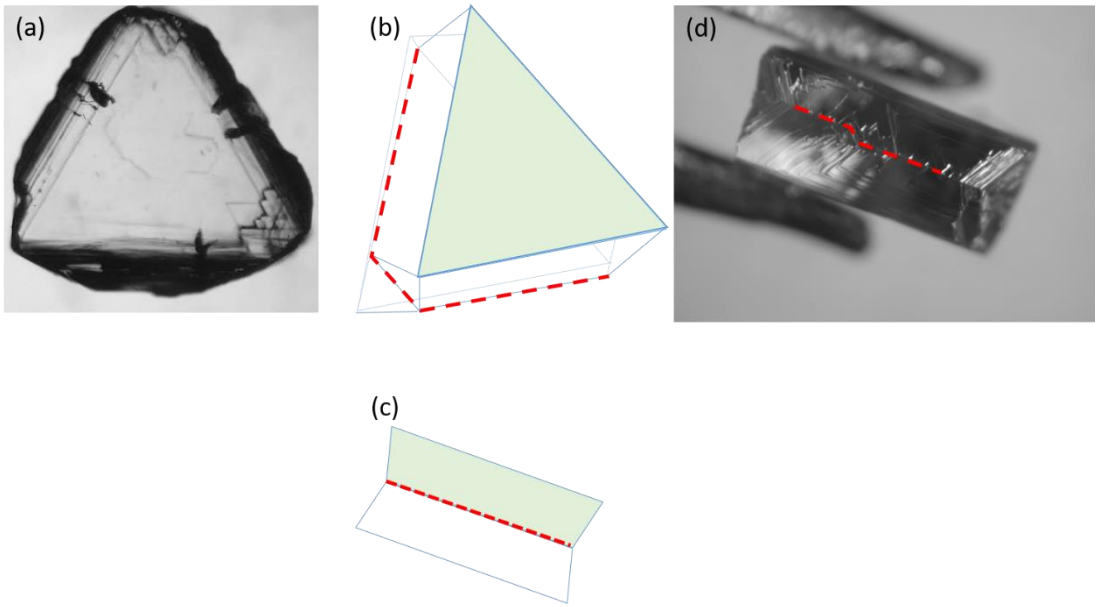

Figure 2. Introduction to macles
(a) One of the two dominant (**111**) *faces in an unpolished macle.*
(b) One of the two dominant (**111**) *faces coloured in green. The two faces are parallel to a twinning plane which separated here by a red dotted line.*
(c) A macle turned on its side. The twinning plane is traced by a dotted red line. One twin is green while the other is white.
(d) An unpolished macle turned on its side with the non-linear twinning plane traced in red.

1.3. Motivation

Hardmetals are used in high heat, high stress and high abrasion environments because of their high melting point, hardness and wear resistance. However, these high heat, stress and abrasive environments damage the grains. The wear in materials is called plastic deformation, which is the deformation of a material undergoing some force (Bolton & Redington, 1980; Johannesson & Lehtinen, 1973). Plastic deformation builds up in materials until a critical point is reached. After this critical value, the grain fragments and ultimately the grain fails and cracks (Gee *et al.*, 2009). Studying the damage built up in hardmetals improves

the hardmetal community's understanding of wear during abrasion and helps in developing new materials (Mingard & Gee, 2007).

Twinned diamonds are fascinating for the information they reveal about the earth's mantle billions of years ago (Jablon & Navon, 2016). Their twinning has been studied for nearly a century (Machado *et al.*, 1998; Yacoot *et al.*, 1998; Friedel, 1926) using non-destructive X-Ray techniques. Combining, modern electron microscopy techniques, reveals new information about the growth of macles, the role of dislocations in twinning and intergrowth between supposed contact twins (Yacoot *et al.*, 1998).

1.4. Thesis overview

This thesis consists of seven chapters.

1. The first chapter briefly introduces the materials covered in this thesis, describes the motivation for this study and outlines the objectives and structure of this work.

2. The second chapter describes methodology; sample preparation, crystallography, data acquisition and data analysis techniques. The data analysis techniques include scanning electron microscopy, cathodoluminescence imaging, electron backscattered diffraction and electron channelling contrast imaging.

3. The third chapter discusses identifying dislocations and subgrains in tungsten-carbide grains using scanning electron microscopy techniques.

4. Chapter four extends the results from chapter three by studying the dislocations present in as-sintered basal and prismatic WC grains.

5. In chapter five, basal and prismatic WC grains were indented using a Berkovich and a spherical indenter. ECCI and EBSD data were collected before and after indentation and crystallographic defects are identified. The defects due to indentation in these grains are compared to the existing data.

6. The sixth chapter discusses twinning in naturally occurring, gem-quality diamonds. ECCI is used to identify the twinning plane. Cathodoluminescence imaging and EBSD help identify growth history and strain on either side of the twining plane.

7. The seventh chapter presents the conclusions of this thesis and proposes suggestions for future work on this subject.

2. Methodology

2.1. Introduction to crystallographic defects

This chapter introduces crystallographic defects in crystalline materials, the materials in this study and the analytical techniques used. Crystallographic defects disturb the local arrangement of atoms in a crystal. These defects include;

- point defects, intrinsic defects like atomic vacancies or self-interstitial atoms
- stacking faults, localized interruptions in the stacking sequence of atomic layers
- grain boundaries, the atomic arrangement at the border between two randomly oriented grains
- twin boundaries, a boundary within a grain separating two regions with identical crystallography
- dislocations, a change in the arrangement of atoms in a crystal. The movement of dislocations explains the plastic deformation in single crystals

The defects of most relevance to this work are discussed below.

2.1.1. Stacking faults

Stacking faults are planar defects where the local arrangement of atoms is interrupted. As an example, in face-centred cubic lattices, intrinsic faults are the removal of a layer in the stacking sequence. Extrinsic faults are insertions where an additional layer that does not belong in the pattern is inserted into the crystal lattice. Stacking faults can play a role in the plasticity of crystals (Hirth *et al.*, 1992).

2.1.2. Grain boundaries

Polycrystalline materials are composed of many randomly oriented grains separated by grain boundaries. The atomic arrangement along the grain boundary can be affected by the interaction between neighbouring grains. This is most obvious when the misorientation between the two neighbours is large. The effect of this misorientation is generally limited to a few atomic layers on either side of the grain boundary (Hall, 1951).

2.1.3. Twin boundaries

Twinning occurs when a new crystal is added to the face of an existing crystal. The twins are separated by a twinning plane, where they share lattice points. The twinned domain is crystallographically rotated, in a new orientation, from the parent crystal (Nelson, 2013). Twinning is discussed extensively in Chapter 6.

2.1.4. Dislocations

Dislocations are a change in the arrangement of atoms in a crystal. Dislocations can be further characterized by their Burgers vector which is denoted with the symbol $\boldsymbol{b}$ and line direction, where the Burgers vector describes the path necessary to form a closed loop around the dislocation as discussed in Figure 1 (Hull & Bacon, 2001*b*). An edge dislocation is as an extra half plane of atoms inserted into the regular arrangement of atoms. Edge dislocations have a Burgers vector perpendicular to the line direction as seen in Figure 1a. A screw dislocation can be described by displacing half a crystal plane while leaving the other half intact. Screw dislocations have a Burgers vector parallel to the line direction as illustrated in Figure 1b. Mixed dislocations have edge and screw characteristics. Their Burgers vectors and line directions are neither perpendicular nor parallel to each other. Partial dislocations bind either side of a stacking fault.

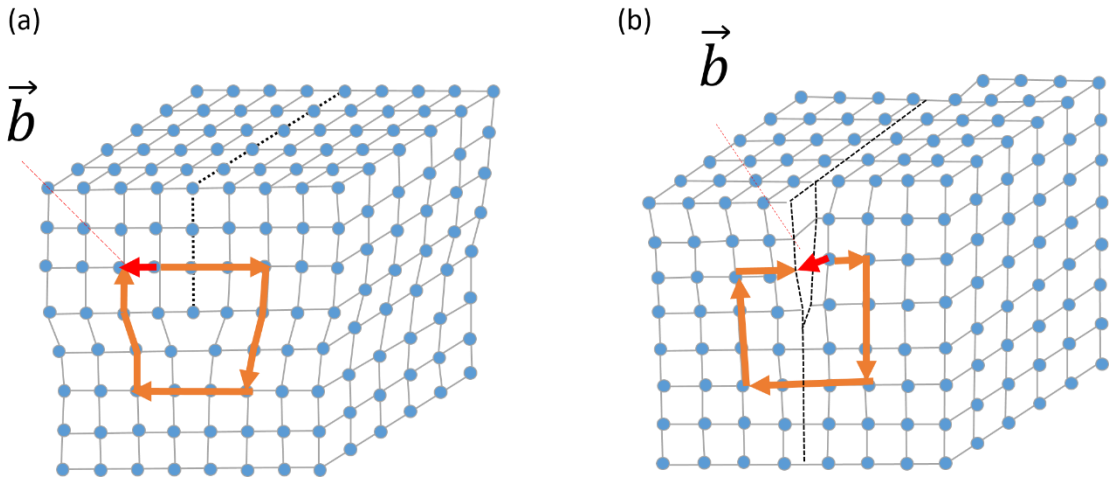

Figure 1. Model of dislocations in a simple cubic lattice
(a) The edge dislocation is formed by inserting a half plane of atoms into the lattice. To understand the Burgers vector, a full circuit with three steps in each of the four two-dimensional directions is drawn around the dislocation with orange arrows. At the end of the circuit, the circuit does not close. This gap is called the Burgers vector and is indicated by the red arrow. The Burgers vector in edge dislocations is perpendicular to the inserted half plane of atoms.
(b) The screw dislocation is formed by shifting faces relative to each other. The circuit in this case is a spiral and the Burgers vector is parallel to the shifted faces.
Figures 1 is adapted from
https://www.jeol.co.jp/en/words/emterms/search_result.html?keyword=dislocation

2.1.5. Slip

The movement of dislocations in the plane containing both its line and Burgers vector is glide. Slip occurs when many dislocations move in a crystal and is a common example of plastic deformation in crystalline materials. Slip planes are the successive sliding of atomic planes. Slip generally takes place on the planes with the highest density of atoms and the direction of slip is most frequently in planes with the shortest lattice translation vectors (Hull & Bacon, 2001c). Chapters 3, 4 and 5 will discuss exceptions to this generalization. Dislocations are crystallographic defects that forms a boundary within the crystal of a slipped area (Bilby, 1954). Slip systems describe the set of planes and associated directions upon which dislocations and plastic deformation occur. When an

external force acts upon a material, parts of the crystal lattice glide along each other (Hull & Bacon, 2001*a*). Depending on the crystal lattice and the material, different slip systems can manifest themselves.

2.2. Materials

2.2.1. Tungsten carbide-cobalt (WC-Co), a hardmetal

The composition and basic crystallization mechanism of WC was described above. A better understanding of the microstructure of WC can contribute to improved performance. This understanding can come from greater knowledge of the dislocation and defect structures inherent in as-sintered WC.

As introduced in chapter 1, WC has a hexagonal crystal structure. The hexagonal crystal system is described in Miller-Bravais notation by four axes. Three coplanar axes; a_1, a_2 and a_3, lie in the basal plane, separated by 120°. The fourth axis, c, is the principal axis with the highest rotational symmetry in a hexagonal material and lies normal to the basal plane (Edington, 1976). The basal plane, or c-plane, in hexagonal WC, is the plane perpendicular to the principal axis, the c axis, Figure 2a and Figure 2e. The primary prismatic plane, or m plane, intersects the a_1^+ and a_3^- axes by the unit distance a, and lies parallel to the third a_3^- axis, depicted here as the $(10\bar{1}0)$ plane in Figures 2b and 2f. A second order prismatic plane, depicted here as the $(11\bar{2}0)$ plane in Figures 2c and 2f, intercepts two of the a-axes and is perpendicular to the third. In Figure 2f, the secondary plane intersects the a_1^+ and a_2^+ axes and is perpendicular to the third a-axis, a_3. A third order prismatic plane, depicted here as the $(21\bar{3}0)$ plane in Figure 2f, intercepts all of the a-axes (Peck & Ostrander, 2018). The third order prismatic plane is not discussed in this study. Pyramidal planes, Figure 2d are inclined planes, intercepting the c-axis at only one point, and are not discussed in this study. A ball and stick model of the hexagonal crystal structure with carbon atoms in grey and tungsten atoms in blue is depicted below in Figure 2g.

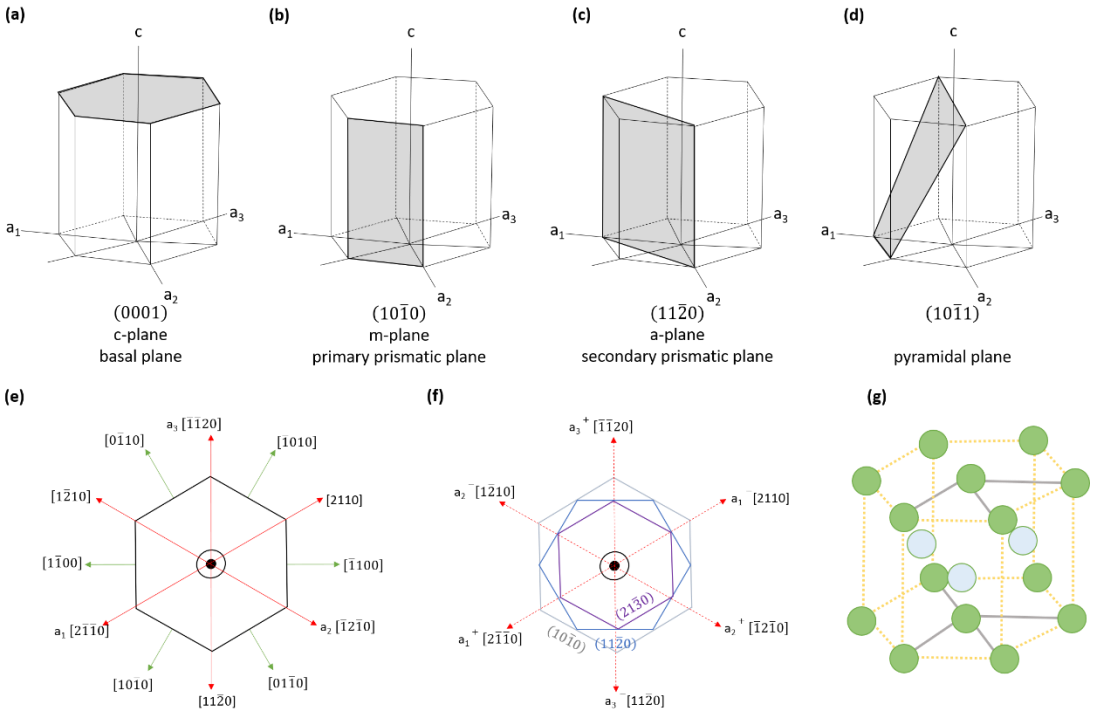

Figure 2. Crystallography of hexagonal materials
(a) The basal plane
(b) the primary prismatic plane
(c) the secondary prismatic plane
(d) a pyramidal plane
(e) directions on the basal plane, with the central dot indicating the c plane coming out of the plane
(f) 1st (outer grey hexagon), 2nd (middle blue hexagon), and 3rd (inner purple hexagon), order prisms as seen from the basal plane in the hexagonal system, with the central dot indicating the c plane coming out of the plane.
(g) *A ball and stick model of the hexagonal crystal structure with carbon atoms in grey and tungsten atoms in blue.*

In the theoretical model of a perfect hexagonal material, the ratio of the length of the c and a axes is 1.633. This ratio in most hexagonal materials lies between 1.5 and 1.89. The difference in ratio arises from the difference between the different types of atoms (Hull & Bacon, 2001*b*) in the unit cell. In WC, the c/a ratio is 2.837 *Å*/2.906 *Å*, leading to an unusually low ratio of 0.98 (Kurlov & Gusev, 2013). Nonetheless, WC has a stable configuration due to the formation of strong nearest-neighbour W-C bonds (Lay & Missiaen, 2014; Mattheiss & Hamann, 1984). The length of the c and a axes also plays a role in the movement of crystallographic defects in the crystal lattice. Describing the physical

manifestation of dislocations and slip for WC grains facilitates an understanding of the complexity of dislocation behaviour in the material.

Dislocations in as-sintered WC grains can result from the stress relating to the compression of grains that grew next to each other, or grain boundary coalescence. The grain boundaries in WC-Co, the rotation angle between grains and the observed grain boundary plane is categorized in detail by Lay and Missiaen, 2014. They discuss how one ideal grain boundary between WC grains, a twist boundary, on the $[10\bar{1}0]$ plane shows the most continuity between crystal lattices except at regularly placed steps. These steps are accompanied by dislocations which rectify the c/a ratio. These dislocations on the $[10\bar{1}0]$ plane have a Burgers vector of $^1/_6\langle\bar{1}2\bar{1}3\rangle$. Other dislocations on the $[10\bar{1}0]$ plane have a Burgers vector of $^1/_3\langle\bar{1}2\bar{1}0\rangle$ or $\langle 0001\rangle$ (Vicens *et al.*, 1988). Previous studies have found that many of these boundaries were inherent in the WC powder before sintering (Kim *et al.*, 2003; Kumar *et al.*, 2006; Lay & Loubradou, 2003).

The current model for dislocations and slip in WC is primarily based on studies where WC grains were indented and the induced defects in the crystal lattice were categorized (Takahashi & Freise, 1965; Hibbs & Sinclair, 1981). In these studies, the slip plane is identified as $[10\bar{1}0]$, Figure 3a. Luyckx, Johannesson and Lehtinen and Hibs and Sinclair subsequently suggested a slip direction of $\langle 11\bar{2}3\rangle$, Figure 3b. In undeformed WC grains, dislocations with Burgers vectors of $\langle 0001\rangle$, $^1/_3\langle 1\bar{2}10\rangle$ and $^1/_3\langle 1\bar{2}13\rangle$ are mobile on a variety or dislocation planes (Greenwood *et al.*, 1982). As most of the work in this field has focused on intentionally damaging WC grains with indenters and observing the induced defects (Rowcliffe *et al.*, 1988; Takahashi & Freise, 1965; Hibbs & Sinclair, 1981; Johannesson & Lehtinen, 1973), these dislocations do not necessarily describe dislocations inherent in the material after sintering.

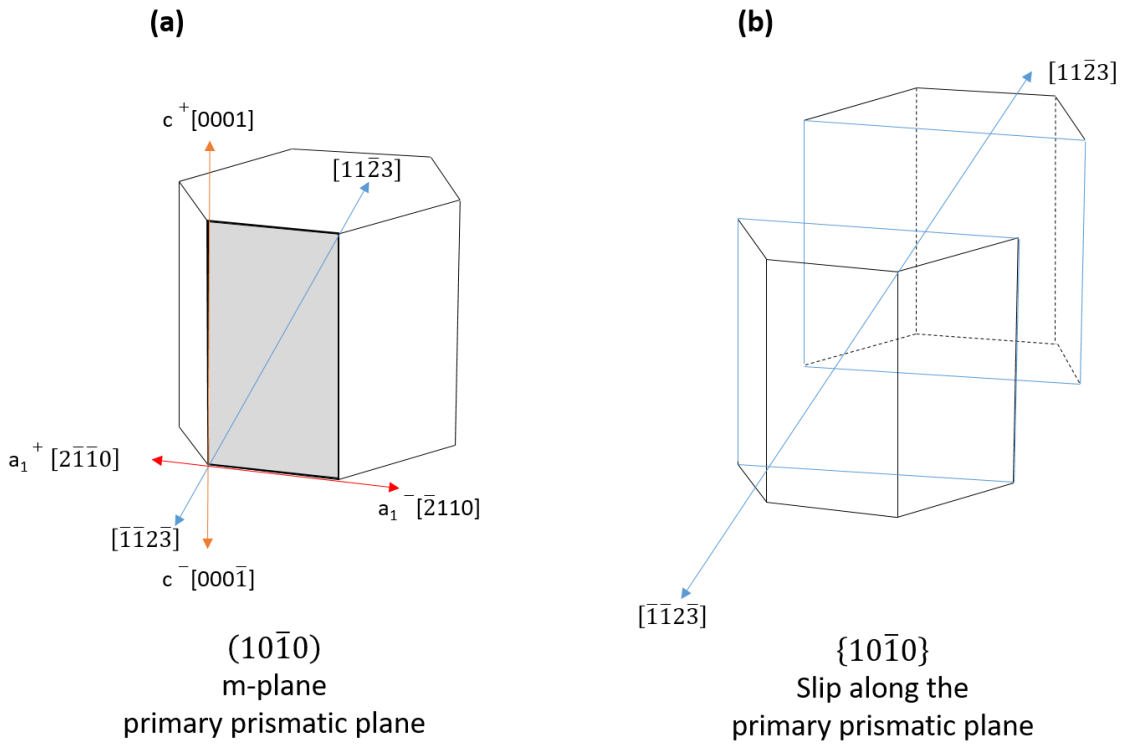

Figure 3. Slip on the primary prismatic plane.
(a) The primary prismatic plane and associated directions
(b) Direction of slip in the prismatic plane in the **[11$\bar{2}$3]** *direction.*

2.2.2. Diamonds

Diamond and graphite are the two main polymorphs of naturally occurring crystalline carbon. In diamond, all atoms are connected to their four immediate neighbours by single covalent bonds, forming a cubic crystal structure, as seen in Figure 4. The strong covalent bonds between carbon atoms in diamonds and their high lattice symmetry contribute to their high hardness, incompressibility and thermal conductivity (Fritsch, 1998).

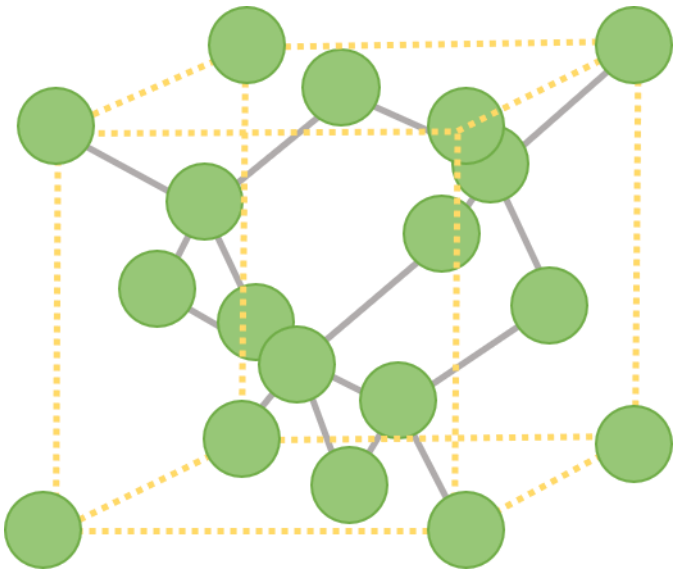

Figure 4. Ball and stick model of the diamond crystal structure
Image adapted from (Tappert & Tappert, 2011)

Naturally occurring diamonds crystallize in different habits, or shapes. These fall into three principal types: monocrystalline (including twinned crystals), polycrystalline aggregates of single-crystal diamonds and fibrous diamonds (Orlov, 1977). Monocrystalline diamonds have octahedral habits with smooth faces or stepped features caused by resorption. The octahedral habit can be distorted, reflecting stresses or dissolution. Dissolution is a chemical reaction between a fully formed diamond and the magmas surrounding it before the diamond reaches the earth's surface. Dissolution leads to the development of pseudo-rhombic-dodecahedral and pseudo-cubic forms (Moore & Lang, 1974). Monocrystalline crystals are commonly transparent and come in a variety of colours: white, yellow, brown, pink, blue and green. The single octahedral form represents equilibrium crystallization and a slow growth rate from a saturated medium (Sunagawa, 1984). Twins, oriented in different, yet crystallographically controlled directions, and parallel intergrowths where the various crystals are oriented along the same crystallographic planes are also considered monocrystalline diamonds. Twinning can occur during the crystallization of a diamond or by mechanical deformation (Cahn, 1954). Twinning during crystallization results in two different kinds of twins, contact twins and

penetration twins. In 1998, Machado et al., demonstrated that naturally occurring contact twins, known in the diamond industry as macles, contain intergrowths between the two twins along the (111) plane. Based on X-ray topographs, twinning in macles starts with a nucleus at the beginning of the diamond's crystallization (Yacoot *et al.*, 1998). These topographs showed increased growth on the (111) planes leading to a triangular habit with two dominant (111) oriented faces parallel to the twinning plane (Machado *et al.*, 1998). Aggregates of randomly oriented monocrystalline diamonds generally include intergrowths of other material and are not considered pure diamonds (Kurat & Dobosi, 2000). Fibrous diamonds grow as fibres, slightly misaligned from the average orientation. This growth leads to the development of cubic habits instead of octahedral ones. Transitions between fibrous and monocrystalline growth are common, leading to the formation of cloudy diamonds (a fibrous zone surrounded by monocrystalline growth) or coated diamonds (a fibrous growth zone that crystallized on a pre-existing monocrystalline diamond). Fibrous diamonds reflect a fast growth rate from a super-saturated medium (Sunagawa, 1984).

The cubic crystal system, also known in mineralogy as the isometric crystal system, is described in Miller-Bravais notation by three axes. These three axes; a_1, a_2 and a_3, are equal and perpendicular, intersecting at 90°, as seen in Figure 5a. Within the isometric system, diamonds are further classified in the hexoctahedral class as octahedrons. A typical diamond is composed of eight equilateral triangular faces. Each of these faces intercepts the three axes at equal distances (Peck & Ostrander, 2018). The exposed diamond faces are each in the {111} family of directions, Figure 5b. A twinned diamond consists of two dominant (111) oriented faces, one of which is the green triangle in Figure 5c, parallel to the twinning plane.

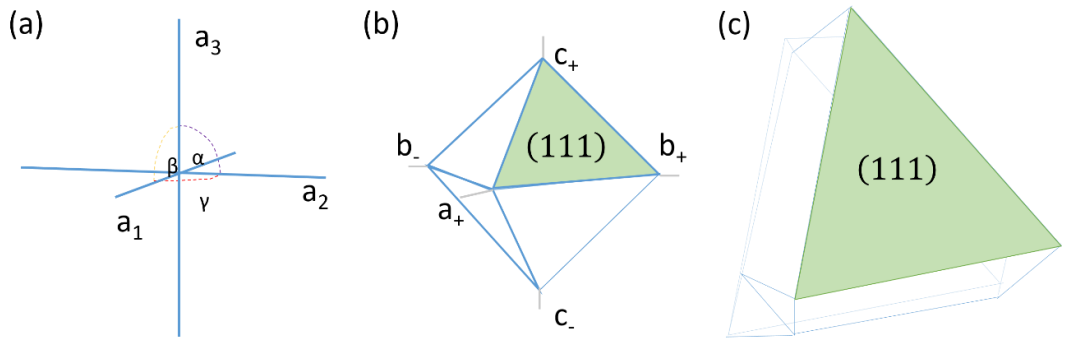

Figure 5. Crystallography of an isometric system
(a) Crystallographic axes in an isometric crystal system. The axes lengths; a_1, a_2 and a_3 are equilength and perpendicular to each other at 90°.
(b) An octahedron with eight equilateral triangles.
(c) A macle diamond with two primary (**111**) *faces. One of these two faces is coloured in green. The two faces are parallel to a twinning plane which separates them.*
Figures 5a and 5b are adapted from
https://www.mindat.org/article.php/2823/Crystallography%3A+The+Isometric+System

2.3. Sample preparation

2.3.1. Sample preparation for WC

In the present work, results were obtained from two grades of WC-Co, a coarse grained sample with 11 wt% Co in the binder phase and a mean WC grain size of 4.5 µm and a medium grained sample with 10 wt% Co in the binder phase and a mean WC grain size of 2.1 µm. The samples were first mechanically polished to an optical finish using standard metallographic techniques, finishing with a colloidal silica polish which leaves a mirror finish and no visible scratches on the surface. Samples were also further polished in a Hitachi IM4000 argon ion beam polishing system to try to remove any fine scratches due to the mechanical polishing. In general significant material removal by ion beam polishing required an Ar+ ion beam of 6 kV for a minimum of 30 minutes, followed by lower beam energies of 3 or 1.5 kV for similar times. This created a polished surface ready for examination in the SEM. While producing a scratch free surface, ion beam polishing induces shallow (of the order of 10 nm) dimples in

the WC grains despite rotation under the ion beam to even out variation in milling rate with grain orientation: these dimples need to be taken into account when analysing the acquired data.

In this study, some WC grains were indented using a nanoindenter to understand the defects induced upon deformation. Nanoindentation is a typical technique used to measure the hardness and Young's modulus of bulk materials (Sakharova *et al.*, 2009). Results from the use of two different nanoindenters are discussed in Chapter 5; a Berkovich indenter and a spherical indenter. A spherical indenter, also known as a conical indenter, is a round tipped indenter. Berkovich indenters are pyramidal, with the three edges of the pyramid coming together at a point, as seen in Figure 6. The strain distribution obtained at different loading pressures per indenter varies and may play a role in determining which indenter to use in an experiment (Sakharova *et al.*, 2009).

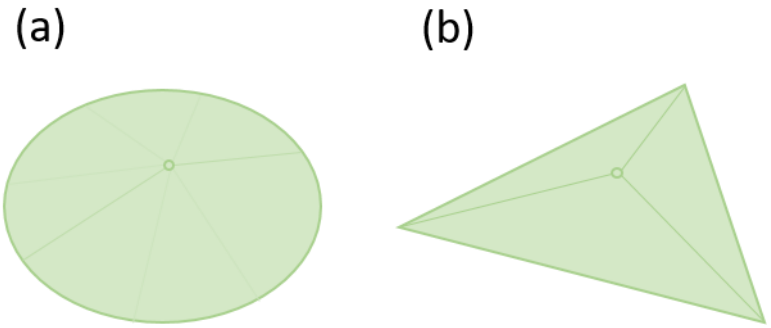

Figure 6. Indenter geometries
(a) spherical indenter
(b) Berkovich indenter
Images adapted from Sakharova *et al.,* 2009

2.3.2. Sample preparation for diamond

The macles were polished perpendicularly to their twinning plane as seen on the red flat surface in Figure 7, exposing the trace of the twin growth plane in the central part of the polished area, as seen in the thin solid blue line in Figure 7. Gem quality diamonds are polished using a polishing wheel called a scaife, a disk impregnated with diamond powder turning at 4000 revolutions per minute

(rpm). The diamond is held manually in a device called a tang until the diamond's surface reflects light. The polished slabs are cleaned by ultrasonicating them in HF (60%) and HNO_3 (69%). They are then rinsed in distilled water and in ethanol ahead of analysis. This is intended to remove all traces of organic and inorganic contaminants by dissolving anything exposed on the diamond faces and the polished surface. The samples are mounted on a SEM sample stub and the exposed polished diamond surface is cleaned with ethanol. Prior to analysis the diamond is carbon-coated to permit electric conduction and reduce charging of the sample.

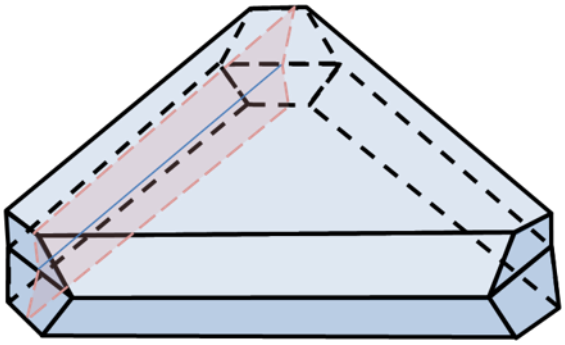

Figure 7. A simplified representation of the polished plane twinning plane.
The polished twinning plane in in red and the trace of the twinning plane is in blue.

2.4. Analytical techniques

2.4.1. Scanning electron microscope and electron probe microanalyzer

A scanning electron microscope (SEM) and an electron probe microanalyzer (EPMA) are each a type of electron microscope. By scanning the surface of a sample in a raster pattern with a focused beam of electrons, images that reflect topography or variations in chemistry can be produced using different signals generated by the electrons. The position of the electron beam and the intensity of the generated signal are combined and used to create an image. Three of these

signals, secondary electrons, backscattered electrons and cathodoluminescence are discussed below.

2.4.2. SE

Secondary electrons (SE) are generated when electrons from the electron source excite the sample's atoms and the atoms emit electrons from their conduction or valence band by inelastic scattering. These are low energy electrons and originate within a few nanometres of the sample surface. The signal contrast depends on the number of electrons reaching the detector and is heavily affected by variations in topography on the sample surface (Goldstein *et al.*, 1981).

2.4.3. BSE

Backscattered electrons (BSE) are high energy electrons that originate in the electron gun. These electrons interact with the sample and are backscattered out of the sample towards the BSE detector. In standard BSE imaging, elements with a higher atomic number emit BSE more strongly than elements with a lower atomic number. The difference in intensity of emitted electrons helps reveal regions with different chemical composition (Goldstein *et al.*, 1981) as seen in Figure 8a. Backscattered electrons can be used to understand crystallographic defects. Two techniques that exploit backscattered electrons, electron backscatter diffraction (EBSD) and electron channelling contrast imaging (ECCI), are discussed below. Illustrative examples of these techniques can be found in Figure 8b and c.

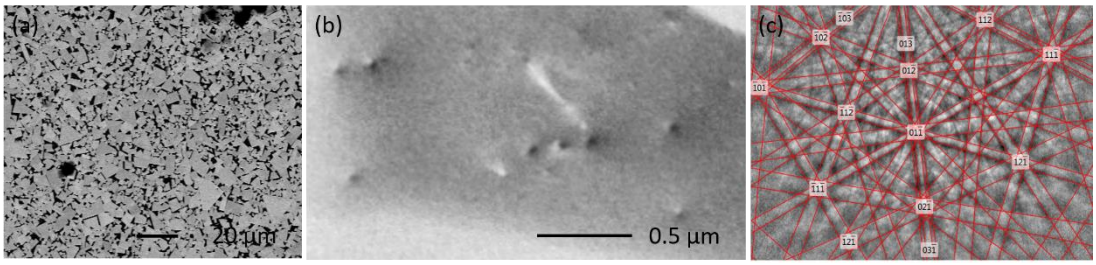

Figure 8. Information revealed by backscattered electrons
(a) A Z contrast image. The higher atomic Z WC grains appear brighter than the lower atomic Z cobalt matrix.
(b) Electron channelling contrast image of a WC grain reveals individual dislocations
(c) Indexed electron backscatter diffraction pattern of WC.

2.4.3.1. ECCI

Electron channelling contrast images (ECCI) are generated when electrons are diffracted by crystal planes in an appropriately oriented sample (Wilkinson & Hirsch, 1997; Joy *et al.*, 1982; Simkin & Crimp, 1999; Zaefferer & Elhami, 2014). Small changes in crystallographic orientation or defects in the crystal lattice are reflected in contrast variations within the image. As the electron beam scans the sample surface, the backscattered electron detector records the variation in intensity of the backscattered elections and produces an electron channelling contrast image (Williams & Carter, 2009; Naresh-Kumar *et al.*, 2012). By tilting a sample away from the horizontal, there is an increase the intensity of the backscattered signal, as the number of backscattered electrons leaving the sample increases. Such small changes in orientation and strain are revealed in this technique that rotation boundaries and individual dislocation can be resolved. By using observations of dislocations in grains of varying orientation tentative identifications of dislocations are made. This is done by applying the $\boldsymbol{g} \cdot \boldsymbol{b}$ invisibility criterion used in transmission electron microscopy, where $\boldsymbol{g}$ is the diffraction vector and $\boldsymbol{b}$ is the Burgers vector of the dislocation (Edington, 1976).

Crystallographic defects, such as dislocations are invisible in an ECCI image if they do not distort the plane(s) which diffract the incident electron beam. In such a diffraction condition, the scalar product $\boldsymbol{g} \cdot \boldsymbol{b} = \mathbf{0}$, this is the invisibility criterion. This is only strictly true for screw dislocations where the Burgers vector of the dislocation and the dislocation line direction are parallel. For edge and mixed dislocations the condition $\boldsymbol{g} \cdot \boldsymbol{b} \times \boldsymbol{u}$, where $\boldsymbol{u}$ is the dislocation line direction, also needs to be satisfied. However the visibility of both edge and mixed dislocations are considerably reduced if $\boldsymbol{g} \cdot \boldsymbol{b} = \mathbf{0}$. It is also possible to use an additional technique to identify dislocations which propagate at, or around 90°, to the surface of the grain. These dislocations are observed as spots on the surface of the sample exhibiting black-white contrast (B-W). To identify the dislocations, changes in the direction of the B-W contrast that occur when the direction of $\boldsymbol{g}$ is changed are monitored. For an edge dislocation, the direction of B-W contrast is dependent on the Burgers vector and not on the diffraction vector (Picard *et al.*, 2009). In this case, changing the diffraction condition from $\boldsymbol{g} = (11\bar{2}0)$ to $\boldsymbol{g} = (1\bar{1}00)$ for example, for a [0001] oriented grain results in a reversal in the B-W contrast. This is because the contrast mirrors tensile compressive strain across the dislocation (Ruedl *et al.*, 1962). For a screw dislocation propagating at, or around 90°, to the surface of the grain, the observed B-W contrast is dominated by surface relaxation (Pascal *et al.*, 2018). This means that for a screw dislocation the B-W contrast observed always lies perpendicular to the $\boldsymbol{g}$-vector (Naresh-Kumar *et al.*, 2012). When assessing a mixed dislocation, $\boldsymbol{b}$ is the vector sum of the edge and screw components. Upon assuming a different diffraction condition, $\boldsymbol{g}$, the B-W contrast direction changes its direction by an angle other than 180° (Naresh-Kumar *et al.*, 2012). Note that when the diffraction conditions are changed, this also changes contrast in subgrains, i.e., regions bounded by low angle tilt or rotation boundaries. The limiting factor with regards to ECCI precision in this study is the lack of exact orientation conditions in polycrystalline materials. This can be achieved by locally rocking the beam in a single crystalline material to obtain

an electron backscatter pattern (EBSP). These patterns allow the user to identify the exact diffraction condition when acquiring ECC images, but this is not possible in polycrystalline materials. An alternative technique, rotational electron channelling contrast imaging, can determine orientation conditions in polycrystalline materials using an ultra-precise stage (L'hôte *et al.*, 2019), when available.

2.4.3.2. EBSD

Electron backscatter diffraction (EBSD) is a technique used in scanning electron microscopes to determine the crystallographic microstructure of a sample (Randle, 2000; Schwarzer *et al.*, 2009; Wilkinson & Hirsch, 1997). An electron beam scans a polished sample tilted to around 70° to the normal of the electron source. Tilting a sample to 70° from the horizontal increases contrast and the number of backscattered electrons reaching the detector. Some of the impinging electrons are incident on atomic planes at angles that satisfy the Bragg equation, $n\lambda = 2dsin(\theta)$, where n is an integer, λ is the wavelength of the electrons, d is the spacing of the diffracting plane, and θ is the angle of incidence of the electrons on the diffracting plane. These electrons are diffracted to form a set of large-angle cones, called Kossel cones, each corresponding to a diffracting plane (Zhou, Weilie and Wang, 2006), Figure 9a. Kossel cones diffract off the sample at close to 180° onto a phosphor screen where they appear as parallel lines, called a Kikuchi lines. An accumulation of Kikuchi lines from different diffracting planes form electron backscatter patterns (EBSPs), Figure 9b. A camera collects these patterns which are acquired over a grid of points and then saved, indexed and configured into a map. These maps can be used to understand a sample's microstructure, as discussed below. The EBSD system installed at Strathclyde is an Oxford NordlysNano system mounted on an FEI Quanta Field Emission Gun Scanning Electron Microscope (FEG SEM). The EBSD system installed at the National Physical Laboratory is an Oxford

NordlysNano system mounted on a Zeiss Aurega Field Emission Gun Scanning Electron Microscope (FEG SEM).

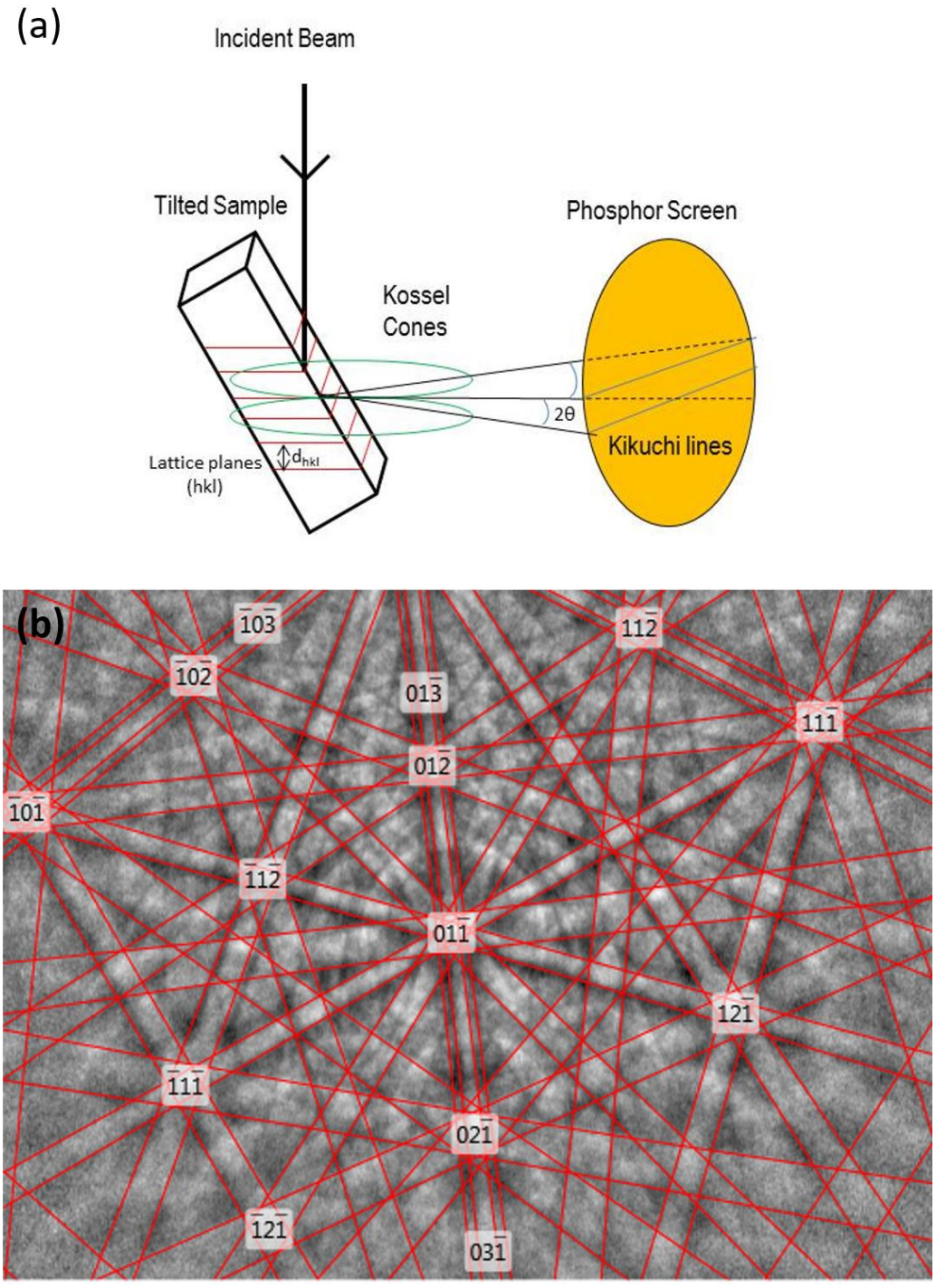

Figure 9. Introduction to EBSD configuration and EBSPs
(a) Electron backscattered diffraction configuration in an SEM
(b) An indexed EBSP from a WC-Co grain.

Several different maps can be generated from the indexed Kikuchi patterns. Band contrast maps reflect the quality of EBSPs as determined by the indexing software. In this case, the Oxford Instruments software assigns a quality number to an EBSP. The higher the value, the better the EBSP quality. Deformed regions will have a low band contrast value and will appear dark in a band contrast map. Band contrast maps can also display regions where the software could not index the EBSP due to grain boundaries, deformed regions, contamination or an unknown/undefined crystallographic phase, like the bottom left region in Figures 10a-d. Band contrast maps are accompanied by a key which consists of a histogram depicting the distribution of band contrast values in the band contrast map. Orientation maps are used to describe the crystal orientation and microstructure of a sample. Examples of these are Euler maps and inverse pole figure maps. Euler maps provide basic information on a sample's microstructure, Figure 10b, by colour coding regions based on differences in microstructure. Euler angles are useful when describing the orientation of a sample with respect to a fixed coordinate system [Euler, 1776]. Using Euler angles, ϕ, θ and ψ, three elemental rotations, are always enough to describe a specific sample orientation. Euler angle map keys show the distribution of grains within the dataset in a given coordinate system. These maps can also be accompanied by Euler angle data, which gives information on the three elemental rotations per pixel. Inverse pole figure (IPF) maps depict which crystallographic direction aligns with the specimen axes and allows for quick interpretation of crystallographic orientation. These maps use colours assigned based on orientation and the selected viewing direction to visualize crystal orientation in the measurement, Figure 10c. Coincident site lattice (CSL) maps reveal special grain boundaries. Some grain boundaries share a certain number of lattice sites with the adjacent crystal lattice. These lattice sites are superimposed, or coincident. These designated boundaries are classified using the reciprocal density of coincident lattice sites, Σ, as seen in red on the band contrast map in Figure 10a. Disorientation imaging is a colour coding method

that factors both the rotation axis and the angle of disorientation between each pixel in a grain and a reference orientation. The colouring algorithm reflects perceptual colour differences that are almost proportional to the true disorientation angles between any of the orientation within the grain (Thomsen *et al.*, 2017), Figure 10d.

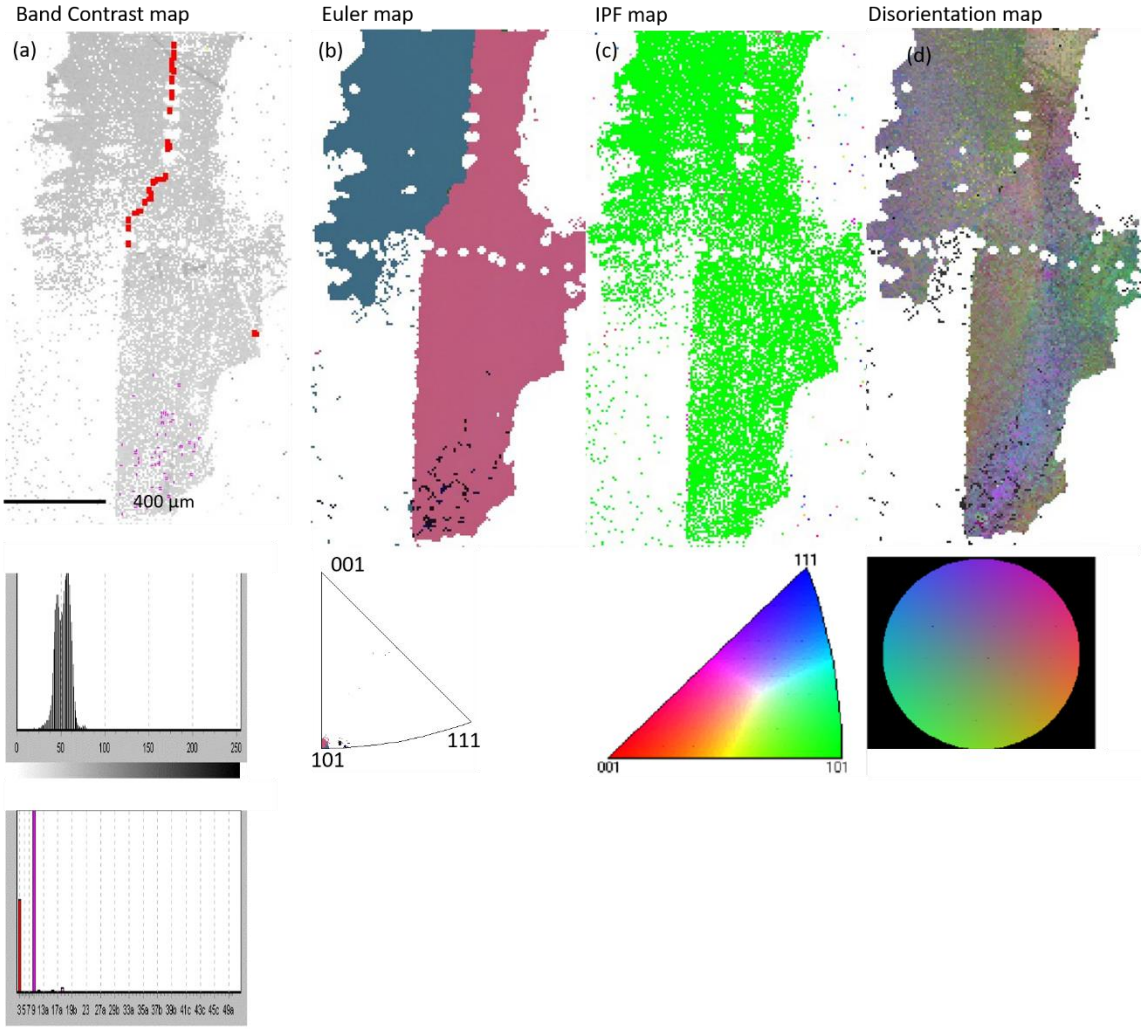

Figure 10. Introduction to EBSD maps
(a) band contrast image with a CSL boundary in red. The band contrast histogram is directly below the map and the CSL key is below the histogram.
(b) An Euler angle map with an Euler angle key below depicting the distribution of crystallographic orientation in the figure.
(c) IPF map shows that both sides of the sample are [101].
(d) Disorientation map and key. The IPF key below depicts the colour guide per crystallographic orientation.
Note that the scale is the same throughout the figure.

Processing EBSD data provides information on a sample's microstructure. Kernel average misorientation (KAM) maps calculate the average misorientation between a pixel and its nearest neighbours. KAM maps are useful in identifying subgrains, Figure 11a. Similarly to KAM maps, grain reference orientation deviation (GROD) maps assign each pixel a value (in degrees) equal to the misorientation that pixel has with the mean orientation of the grain in which the pixel lies, Figure 11b. A slight deviation from a GROD map is a GROD axis map, Figure 11c. In this case each pixel has a value denoting the rotation axis with respect to the mean, as defined by the colour key. The colour key indicates the direction of the misorientation axes in real space above (upper hemisphere) or below (lower hemisphere) the sample. The black dots indicate these directions for each point in the map. The GROD axis map provides significantly more information on the misorientations in the grain when compared to the IPF map. While not providing the high level of detail observed in the ECCI images, these EBSD maps provide a quantitative measure of the misorientations. Colour changes in the GROD axis map match with the subgrain boundaries in the KAM and those observed in the ECCI images. The colour scale also reveals gradual changes in orientation within the subgrains. In the past twenty years, a new field in EBSD, called high resolution EBSD (HR-EBSD) has allowed users to interpret EBSD data with increasing precision. As opposed to the standard Hough transform which is used in EBSD software to identify Kikuchi patterns, experimentally observed Kikuchi patterns are compared to simulated patterns (Chen *et al.*, 2015; Nolze *et al.*, 2015). An optimization procedure is used to find the crystal orientation parameters that lead to the highest similarity between the simulated and experimental pattern. These maps reveal finer details in the EBSD data and contain features that can be compared to ECCI maps, specifically dislocations. Pattern matching was used to acquire images with the resolution found in Figure 11.

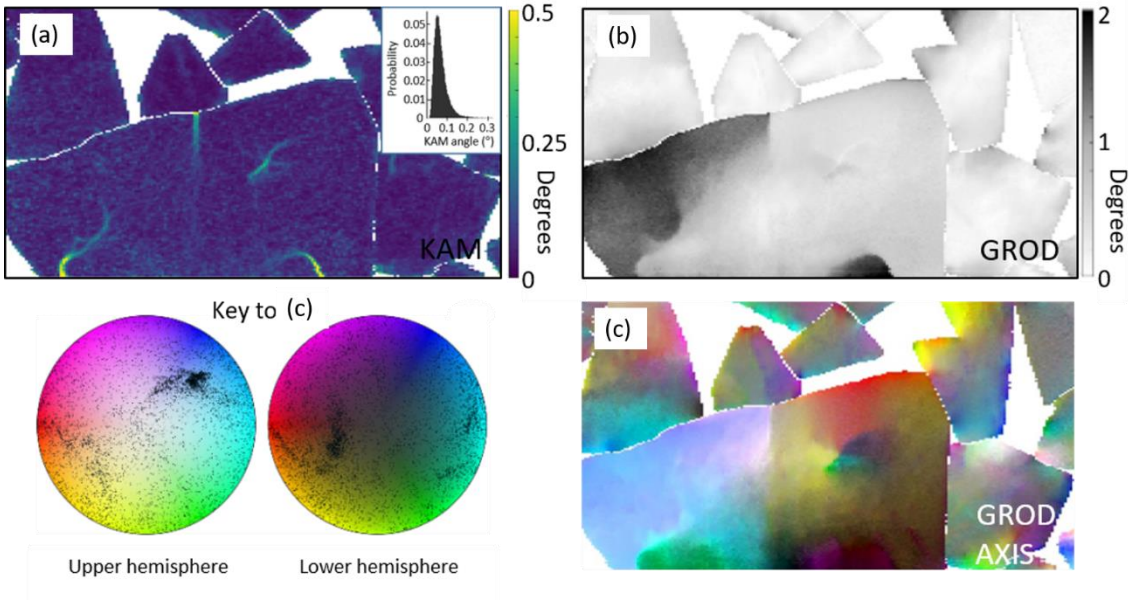

Figure 11. Introduction to pattern matching maps
(a) Kernel average misorientation map with inset key
(b) grain reference orientation deviation (GROD) map with key on the right
(c) GROD axis map with key to the left

2.4.4. CL

Cathodoluminescence (CL) imaging captures the emission of light when a material is stimulated by an electron beam (Edwards & Martin, 2011). This emission can range from the ultraviolet to the infrared and reveals the optical properties of a material. When used alongside other electron microscopy techniques such as energy dispersive spectroscopy (EDS), wavelength dispersive spectroscopy (WDS) or EBSD, CL can reveal nuanced information on the correlation between chemistry and sample growth (Edwards *et al.*, 2012). In a scanning electron microscope, a focused electron beam interacts with the sample surface. As the electron beam scans the sample in an x-y pattern, the emitted light is collected by an optical system and changes in the CL spectra and intensity can be mapped across the sample.

Various CL detectors and detector configurations are possible in an SEM. Different detectors can reveal varying levels of compositional, crystallographic and crystallinity information. These include panchromatic detectors, which

measure all emitted light from a sample; monochromatic detectors, which measure single wavelength bands; single point CL spectroscopy detectors, which measure a spectrum at a single point in the sample; and hyperspectral CL detectors, which acquire a spectrum at every point in a designated region of a sample thereby creating a map with spectral parameters that include intensity, wavelength, peak width and chromaticity.

In this study, a panchromatic detector was used to reveal zoned regions of growth in macles. Panchromatic imaging captures all the light emitted from a material without resolving individual wavelengths. The technique reveals variations in intensity of all the emitted light and the resulting image reflects these variations in greyscale, Figure 12. As such, this technique is most frequently used to study variations in intensity rather than understand the source of the intensity.

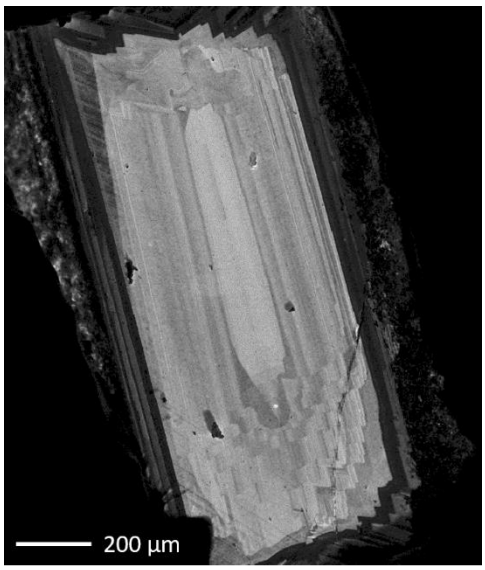

Figure 12. CL image of a macle
Panchromatic cathodoluminescence micrograph of the twinning plane and two "sibling" crystals in a macle.

Cathodoluminescence in diamonds is explained by solid-state band theory. Diamonds, an insulting material, have a valence band and a conduction band with an intermediary forbidden band gap. When the electron beam interacts

with the sample surface, electrons from the valence band are elevated to the conduction band. When the electrons from the elevated conduction band fall back to the lower energy valence band, they can be temporarily trapped by defects in the material. These defects can be structural defects, like lattice imperfections, which are intrinsic defects, or impurities in the material, like rare earth elements, which are extrinsic defects. Luminescence results when the electrons escape the trap within a particular wavelength range while CL intensity is a function of the density of traps (Edwards & Martin, 2011). In naturally occurring diamonds, there are several sources for luminescence. Some of the sources of intrinsic luminescence in diamond include vacancies (Yacobi & Holt, 1990), and nitrogen impurities (Gaft *et al.*, 2005).

3. Subgrain structure and dislocations in indented tungsten-carbide cobalt

3.1. Introduction

This chapter explores the use of the scanning electron microscopy (SEM) techniques of electron backscatter diffraction (EBSD) and electron channelling contrast imaging (ECCI) for studying the microstructure and in particular the subgrain structure and defects present in tungsten carbide (WC) grains in WC-Co hardmetals (cemented carbides). These methods reduce the need for TEM dislocation analysis and provide information over much larger areas, ≈75 × 75 μm^2. EBSD has been used to analyse hardmetals and determine crystal orientation (Mingard & Gee, 2007; Roebuck *et al.*, 2012; Farooq, M.U.; Klement, 2004).

Using ECCI, extremely small changes in orientation and strain are detectable, revealing subgrains and extended defects such as dislocations and stacking faults (Wilkinson & Hirsch, 1997; Joy *et al.*, 1982; Simkin & Crimp, 1999; Zaefferer & Elhami, 2014). This technique facilitates the investigation of contrast exhibited by a defect for different diffraction conditions; ultimately identifying the nature of the defect. Before this study, there did not appear to be any published work on the use of ECCI to identify dislocation types and substructures in hardmetals.

Data was collected from WC grains with surface normals [0001], $[1\bar{1}00]$ and $[11\bar{2}0]$. Below is a discussion of sample preparation in anisotropic, polycrystalline WC, and the study of subgrain structure and dislocation distribution in WC-Co grains.

3.2. Sample specifications and experimental details

In the present work, results were obtained from two grades of WC-Co, a coarse-grained sample with 11 wt% Co in the skeleton (mean WC grain size 4.5 μm), and a medium-grained sample with 10 wt% Co in the skeleton (mean WC grain size 2.1 μm). The samples were first mechanically polished by Dr. Ken Mingard at the National Physical Laboratory to an optical finish using standard metallographic techniques, finishing with a colloidal silica polish which leaves a mirror finish and no visible scratches on the surface. Samples were further polished in a Hitachi IM4000 argon ion beam polishing system to try to remove any fine scratches due to the mechanical polishing. In general, significant material removal by ion beam polishing required an Ar+ ion beam of 6 kV for a minimum of 30 minutes, followed by lower beam energies of 3 or 1.5 kV for similar times. Ion beam polishing removed the scratches from mechanical polishing but left behind shallow (of the order of 10 nm) dimples in the WC grains. These dimples need to be acknowledged when analysing the acquired data.

In this study, ECCI images were acquired at 20 keV and a 10 mm working distance in the backscatter geometry in a Zeiss Auriga FIB SEM using the Zeiss supplied quadrant diode backscattered electron detector which is inserted beneath the pole piece. The electron microscopy techniques are described in detail in Chapter 2. The sample was tilted by around 20° away from the horizontal to increase the intensity of the backscattered signal, as the number of backscattered electrons increases as the tilt of the sample is increased. A series of images of single WC grains with the sample at different tilts or for different rotations were then acquired. In the case of the tilt series, ECCI images were acquired for tilts between 17° and 22° with the sample tilt changed in steps of 0.2°. For the rotation series, the sample was tilted at 20° and rotated 10°

between image acquisitions, with the sample rotated by 180° for each grain. At the time of measurement it was not possible to precisely determine the diffraction conditions for each image acquisition. Diffraction conditions can be determined through the acquisition of local area electron channelling patterns, but this requires local "rocking" of the beam (Wilkinson & Hirsch, 1997) which was not possible in the SEM used for acquisition of this data set. For this work the diffraction conditions for a few of the ECCI micrographs were estimated from the grain orientation with respect to the electron beam. EBSD data in this study was collected in a Zeiss Auriga FIB SEM outfitted with an Oxford NordlysNano system. EBSD maps were acquired at 20 or 30 kV accelerating voltage with a 10 nA beam and the sample tilted at 70° from the horizontal.

3.3. Results

3.3.1. ECCI and EBSD

Initial studies were carried out on a randomly oriented grain in the WC sample with 10 wt% Co in the skeleton which had only a very short (10 minute) ion beam polish. Figure 1 shows a conventional secondary electron image of the sample acquired at 20 kV, tilt corrected for the 70° tilt applied to enable mapping by EBSD. Individual WC grains can be identified but the only contrast variation is between the WC and the binder, and not between different grains.

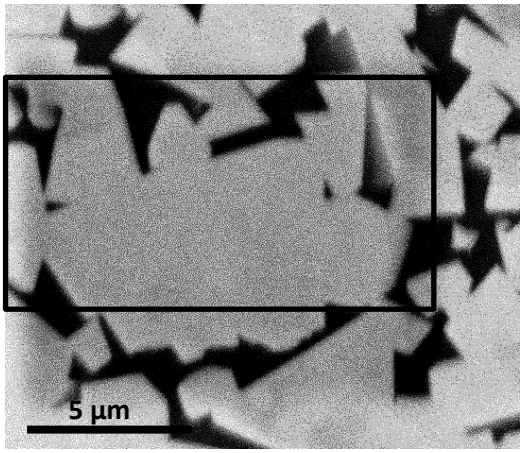

Figure 1. Secondary electron image of a WC sample
This WC sample contains 10wt% Co in the skeleton. Very little detail of structure within the bright WC grains is visible; the area mapped by EBSD in Figure 2 is indicated by the black rectangle.

ECCI data was then acquired of the central grain at varying tilts, as described above. Then the area around the large grain was mapped by EBSD at 20 kV using a relatively long, 50 ms, acquisition time and a resolution of 640×480 pixels to improve angular accuracy. This slow acquisition allowed for clear EBSP acquisition but led to upward sample drift (relative to the map orientation, and opposite to the direction of data acquisition). This caused compression of the target area of 240×170 pixels at a 60 nm step size to give an average pixel size in the vertical direction of approximately 34 nm and only partial mapping of the grain. The EBSD maps shown in Figure 2 are corrected for the drift and were scaled to the electron images which have negligible drift. All the EBSD maps of Figure 2 were produced from the EBSD data using MTEX (Hielscher & Schaeben, 2008; Bachmann *et al.*, 2010; Nolze & Hielscher, 2016), where the orientation of each EBSP was determined by pattern matching to dynamical simulations (Nolze *et al.*, 2017). The Inverse Pole Figure (IPF) map, Fig. 2a demonstrates the random crystallographic orientation of this grain. Fig. 2b and 2c are ECCI data sets acquired at random tilts. The red boxes highlight subgrains whose contrast

changes at varying tilts and whose border is marked by individual dislocations. The blue boxes show individual dislocations that are apparent in Fig. 2c and not in Fig. 2b, an initial indication that a series of images, at varying diffraction conditions is necessary to fully understand the dislocations in a WC grain. Misorientation throughout the grain is evident in Fig. 2d a kernel average misorientation map. Further internal disorientation is clear in Fig. 2e and 2f.

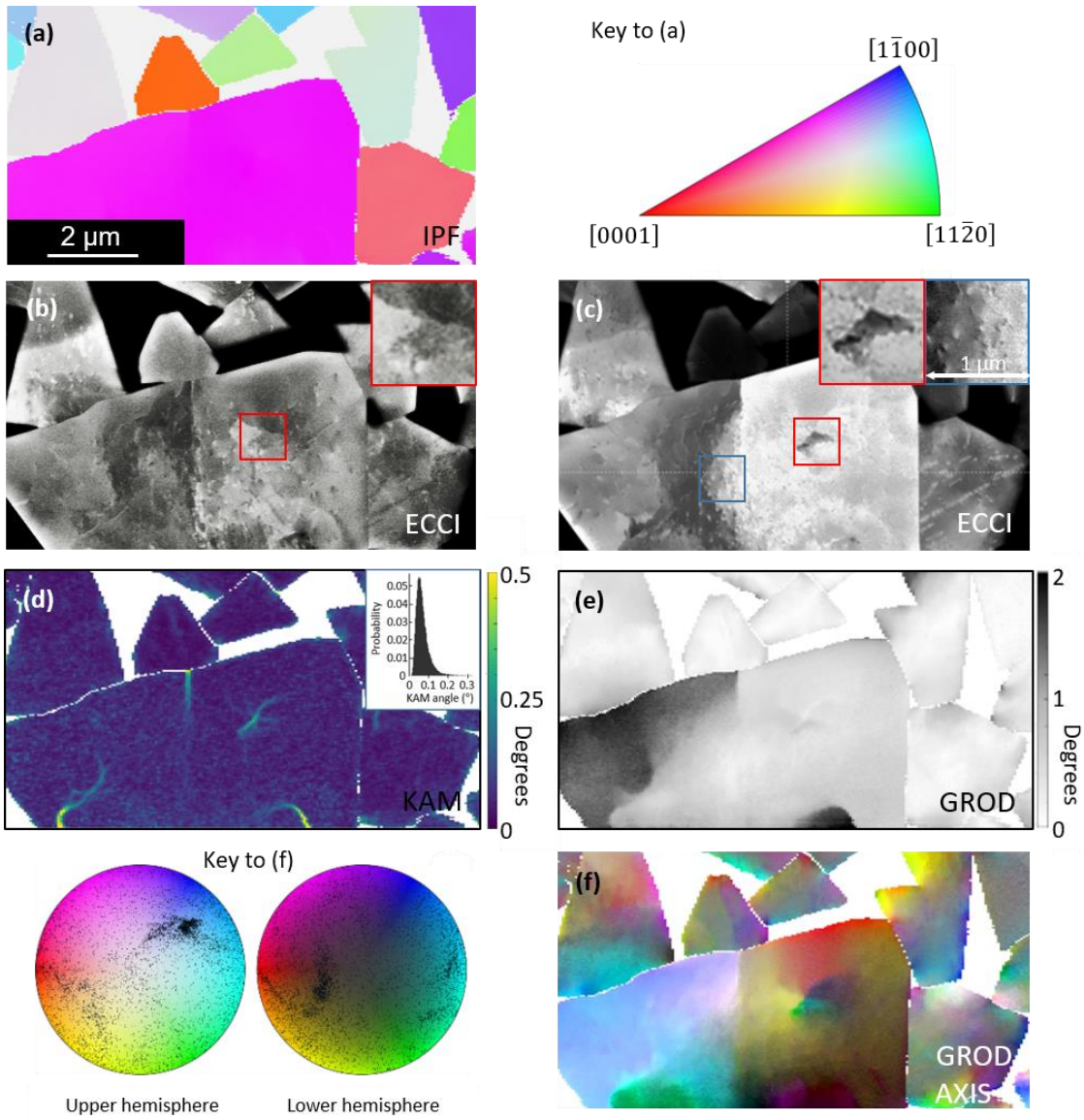

Figure 2. ECCI and EBSD map of a randomly oriented grain
(a) Orientation map coloured with a z-axis inverse pole figure colour scale.
(b) ECCI image with the sample tilted 17° from the horizontal.
(c) ECCI image with the sample tilted 21.4° from the horizontal. The inset shows an expanded view of the area delineated by the blue box in the main image, and highlights the dislocations revealed by ECCI. The red insets shows an expanded view of the area delineated by the red boxes in the main images of (b) and (c), and highlight subgrains revealed by ECCI.
(d) Kernel average misorientation (KAM) map. The inset shows the distribution of KAM angles.
(e) Grain reference orientation deviation (GROD) map. Each pixel has a value (in degrees) equal to the disorientation that pixel has with the mean orientation of each grain. (caption continues on the next page)

(f) Grain reference orientation deviation axis (GROD axis) map. Each pixel has a value denoting the rotation axis with respect to the mean, as defined by the key to the left of the image. The black dots in the key denote the directions for each point on the map.
(Maps (a), (d), (e) and (f) were produced from the EBSD data using MTEX, where the orientation of each EBSP was determined by pattern matching to dynamical simulations.)

Figure 2a shows an inverse pole figure (IPF) map. IPF maps represent crystallographic orientation in terms of the sample coordinate system. This map does not reveal any variation within each WC grain and simply illustrates that this is a polycrystalline sample with grains oriented in different directions.

For comparison, Figures 2b and 2c show two of 19 ECC images of the same region as Figure 1 and 2a, acquired with relative tilts of 17° and 20.4° respectively from the horizontal. A significant level of additional information on the substructure in the grains is revealed by ECCI. Distinct subgrains can be seen in the large grain, for example the red insets in Figure 2b and 2c, as well as individual dislocations, blue inset in Figure 2c. Dislocations are also revealed, which suggest a gradual rotation of the lattice across distances of the order of 1 µm. Subgrains and dislocations change contrast and appear and disappear in the ECCI images as the sample is tilted and the diffraction conditions are changed. In order to reveal all of the subgrains and crystal lattice defects in a grain, a series of ECC images must be acquired to capture all the lattice distortions within the grain.

The EBSD maps in Figure 2, took approximately 40× longer to acquire than the ECCI data. The most important effect of this longer capture time is the drift discussed earlier and the resultant image distortion. After adjustment of the EBSD maps to compensate for the drift, useful information can be obtained from comparison of the EBSD maps and ECCI images. The IPF colour scale of Figure 2a is insensitive to the orientation changes within grains revealed by ECCI, but some quantification is possible by further analysis of the EBSD data. Figure 2d

shows a Kernel Average Misorientation (KAM) map where the KAM angle is the average misorientation angle from the map point to each neighbour (Wright *et al.*, 2011). The KAM map identifies some of the boundaries of the subgrains revealed by ECCI where the change in orientation across them is greater than ≈ 0.2°.

Figures 2e shows a grain reference orientation deviation (GROD) map. In this case each pixel has a value (in degrees) equal to the misorientation that pixel has with the mean orientation of the grain in which the pixel lies. Figure 2f shows a grain reference orientation deviation axis (GROD axis) map. In this case each pixel has a value denoting the rotation axis with respect to the mean, as defined by the colour key to the left of the image. The colour key indicates the direction of the misorientation axes in real space above (upper hemisphere) or below (lower hemisphere) the sample. The black dots indicate these directions for each point in the map. The GROD axis map provides significantly more information on the misorientations in the grain when compared to the IPF map. While not providing the high level of detail observed in the ECCI images, these EBSD maps provide a quantitative measure of the misorientations. Colour changes in the GROD axis map match with the subgrain boundaries in the KAM and those observed in the ECCI images. The colour scale also reveals gradual changes in orientation within the subgrains.

EBSD analysis also allows for investigation of the role that grain boundaries play in the interaction between grains. As discussed in chapter two, coincident site lattice (CSL) maps reveal special grain boundaries. WC grains are not always surrounded by the binder phase, rather they form contacts with other WC grains. The microstructure of the hardmetal depends on the lattice mismatch between these contacts (Lay & Missiaen, 2014). In Figure 3a, an IPF map reveals a region of 57 × 41 μm. Figure 3b is a band contrast image with CSL data superimposed at the grain boundaries.

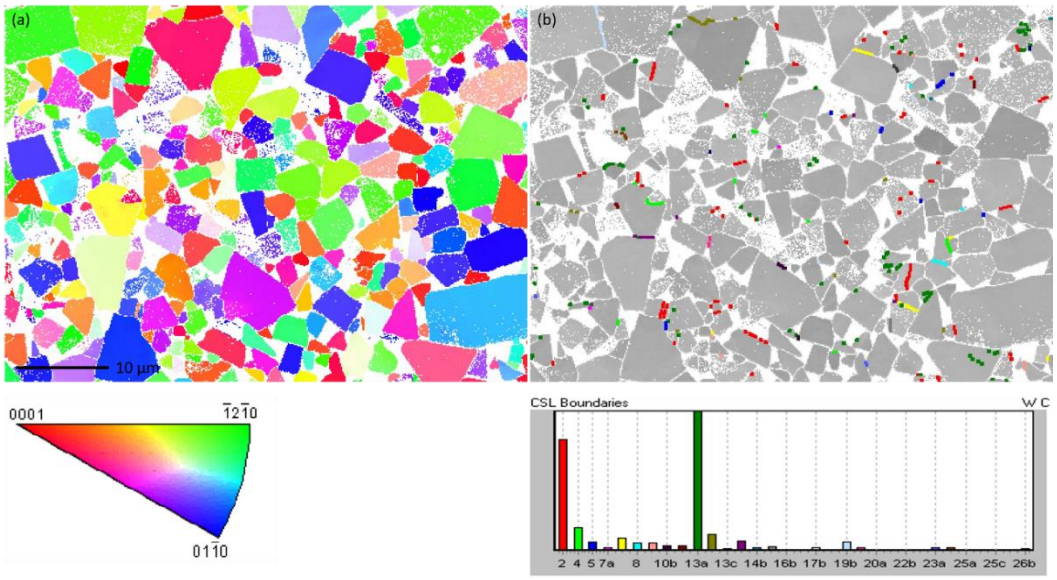

Figure 3. IPF map and CSL grain boundaries
(a) A large area EBSD IPF Z map. The grain in Figures 1 and 2 is the fuchsia grain in the middle of the bottom half of this image. The IPF key is beneath the figure.
(b) A CSL map demonstrates the grains with CSL boundaries.
The figure key is beneath the image.

3.3.2. Preliminary Dislocation Observations

In the example shown in Figure 2, the grain observed was chosen randomly and the ECCI imaging sequence was obtained by tilting in 0.2° increments. Within the limitations of the angular accuracy of the EBSD system, it was not possible to determine the diffraction conditions precisely enough to analyse the dislocation structures in detail. Further detailed imaging was therefore carried out on grains of known orientation. This was achieved by first acquiring EBSD maps of 400 × 300 µm areas, such as the one shown in Figure 4a. Figure 4a is an EBSD pattern quality map, a map that reflects the "quality" or "sharpness" of the diffraction bands in the EBSP acquired at each pixel. Grains with simple orientations, that is grains whose normals lie close (within 3-5°) of one of the principal crystallographic axes $[0001], [1\bar{1}00], [11\bar{2}0]$, were identified from inverse pole figures such as the one shown in Figure 4b. Figure 4b shows those grains whose normals are close to $[1\bar{1}00]$. These grains are coloured blue in the

EBSD quality map of Figure 4a. The crystal orientation of a [1$\bar{1}$00] grain (circled in orange in Figure 4a) is depicted in Figure 4c. A higher resolution image of this [1$\bar{1}$00] oriented grain is shown in Figure 5b.

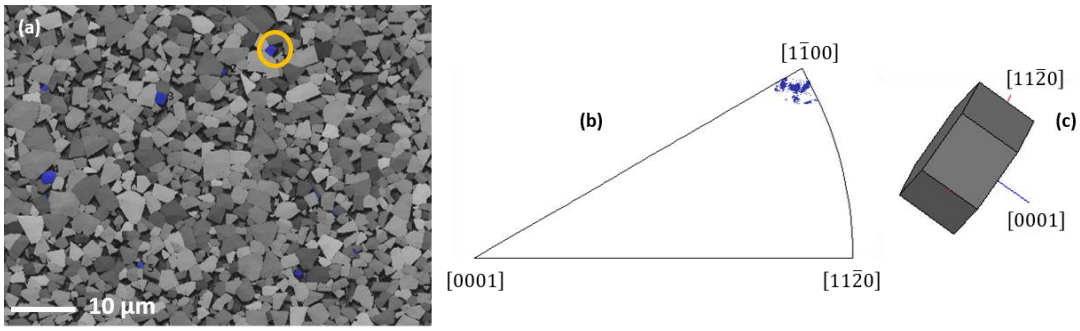

Figure 4. Identifying WC grains close to the [1$\bar{1}$00] sample normal.
(a) A large area EBSD pattern quality map where the grains coloured blue are those identified with the IPF pole figure as having a sample normal close to **[1$\bar{1}$00]**
(b) IPF pole figure highlighting grains whose principal crystallographic are close to the sample normal.
(c) The orientation of the grain circled in orange in Fig. 4a.

On identifying grains with the [0001], [1$\bar{1}$00] and [11$\bar{2}$0] axes normal to the sample, series of ECCI rotation images were then acquired for each of these grain types which were free of polishing damage. Figure 5 shows examples of 3 grains from the WC grain with 11 wt% Co in the skeleton, respectively oriented with the [0001], [1$\bar{1}$00], [11$\bar{2}$0], axes normal to the sample. Dislocations are revealed in the ECCI micrographs intersecting the surface: examples are indicated by arrows in Figure 5. The number of dislocations intersecting the surface in each rotation series was counted per rotation image to calculate the density of dislocations per grain. Densities were similar in all three grains: ≈ 4 × 10^8 cm^{-2} dislocations in the [0001] oriented grain, and ≈ 2 × 10^8 cm^{-2} in [1$\bar{1}$00] and [11$\bar{2}$0]. The dislocations revealed in these grains will be discussed in more detail in Chapter 4.

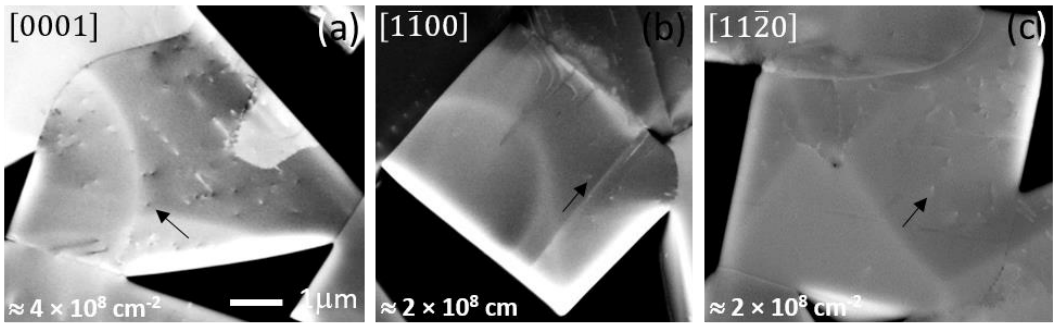

Figure 5. Dislocations as revealed by ECCI in 3 grains
(a) [**0001**] *oriented grain*
(b) [**1$\bar{1}$00**] *oriented grain*
(c) [**11$\bar{2}$0**] *oriented grain*
(The scale bar is the same for all three grains.)

Figure 6 shows three images from a rotation series acquired from the [11$\bar{2}$0] oriented crystal shown in Figure 6c. The facets visible on the grain in Fig 6c were within 0.2° of being perpendicular to each other, which would be expected for such an orientation and gives some degree of confidence in assigning the [1$\bar{1}$00] and [0001] directions determined from EBSD mapping to be parallel to the edges of the grain. The images in Figure 6 have been aligned so that they are parallel with the middle image (Figure 6b). This image is labelled as 0° since it was acquired with the grain edges parallel and perpendicular to the image edge and thus to the scanning direction. Thus to a first approximation, the diffraction **g**-vector selected was close to [1$\bar{1}$00]. The image on the right Figure 6c was acquired with the sample rotated at 90° with respect to the middle image, and thus to a first approximation, the selected **g**-vector was close to (0002). The left hand image Figure 6a was acquired for the crystal at -20° from the middle image and represents a random unknown diffraction condition.

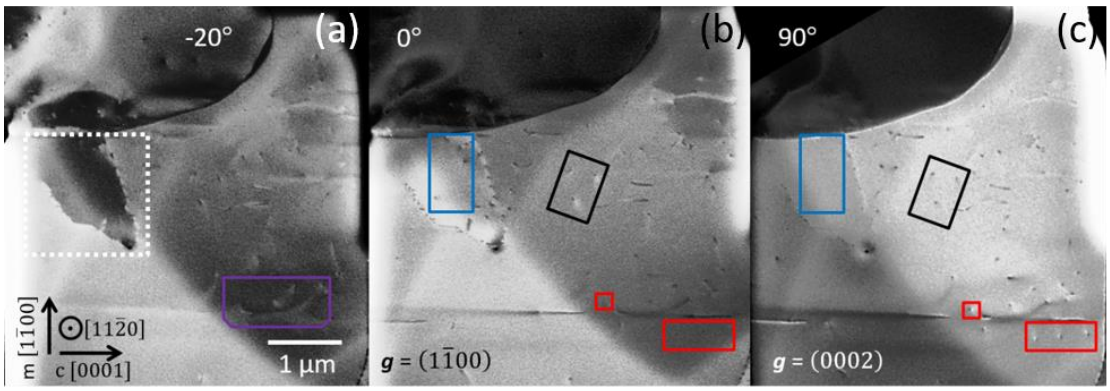

Figure 6. Dislocations as revealed by ECCI in a [11$\bar{2}$0] oriented grain.
(a) -20° rotation
(b) 0° rotation
(c) 90° rotation. The significance of the coloured boxes is discussed in the text.

A subgrain is visible in the top left of image Figure 6a (outlined by the dashed white box) but shows no contrast relative to the parent grain in the middle Figure 6b and right Figure 6c images. Euler angle calculations from EBSD (Table 1) indicate a very small change of its orientation relative to the parent grain (0.1-0.2° around all three axes). The dislocations highlighted in Figure 6 will be discussed in more detail in Chapter 4.

Table 1. Euler angle table for the parent grain and subgrain

Euler angle (°)	Subgrain	Parent grain
ϕ_1	0.8	0.7
Φ	92.8	93
ϕ_2	59.1	59

By comparing the precision of different approaches for orientation imaging using EBSD patterns, research partners at the National Physical Laboratory in

London and at the Academic Centre for Materials and Nanotechnology in Krakow, Dr. Ken Mingard and Dr. Aimo Winkelmann, respectively, were able to image the internal structure of WC grains from EBSD data. This represents an advancement in the field of EBSD as the information revealed by EBSD was now comparable to the ECCI dataset acquired in the present study. Instead of using the traditional Hough-transform based orientation results from the Oxford Instruments EBSD software, Dr. Winkelmann compared each experimental EBSP with a dynamically simulated pattern for the grain in Fig. 6a, above. The qualitative ECCI data presented above is thereby quantified by the orientation data from pattern matching, Fig. 7b (Winkelmann *et al.*, 2020). As opposed to the standard Hough transform which is used in EBSD software to identify Kikuchi patterns, experimentally observed Kikuchi patterns are compared to simulated patterns (Chen *et al.*, 2015; Nolze *et al.*, 2015). An optimization procedure is used to find the crystal orientation parameters that lead to the highest similarity between the simulated and experimental pattern.

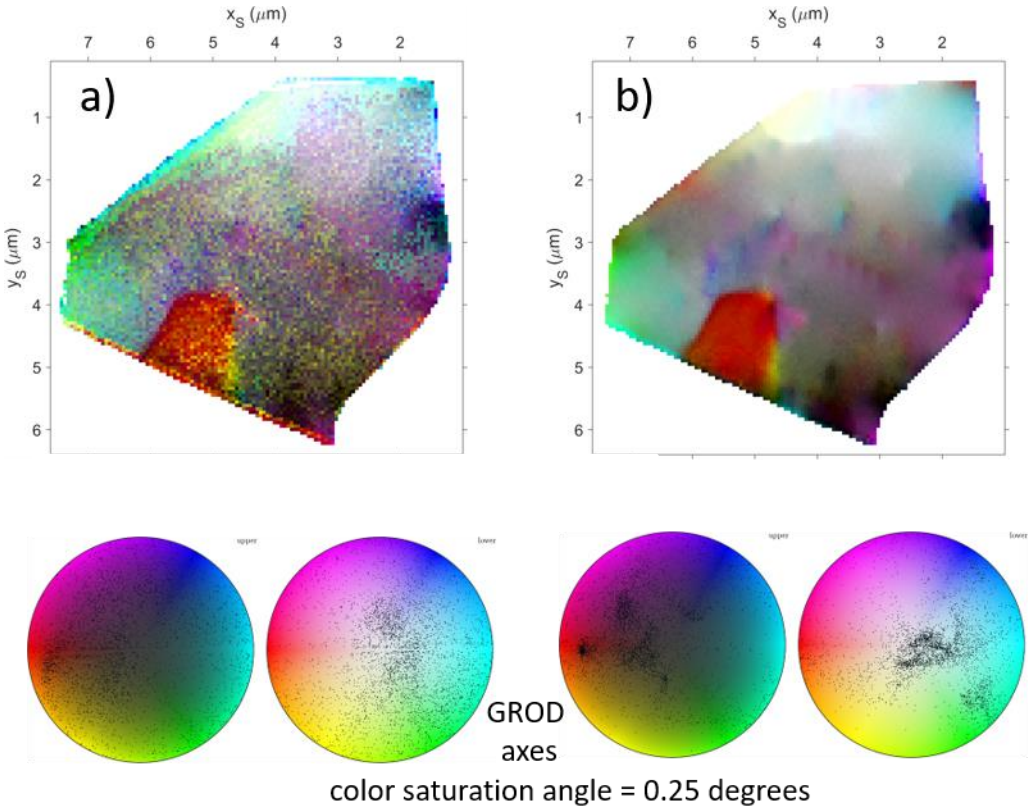

Figure 7. Comparison of refined accuracy data and pattern matching results
(a) refined accuracy data and
(b) pattern matching results.
Maps and colour keys of the grain reference orientation deviation (GROD) with the mean orientation of the grain as the reference.

In the maps generated using MTEX by Dr. Aimo Winkelmann, Fig. 7, it is clear that the Hough-transform map, Fig. 7a shows more misorientation noise than the pattern matching map in Fig. 7b. The pattern matching map consists of features that can be compared to ECCI maps, specifically the dislocations found in Fig. 7a.

3.4. Discussion

3.4.1. Ramifications of sample preparation

As with other techniques such as TEM foil analysis, care must be taken that dislocations observed are inherent in the material and not an artefact produced by the sample preparation method. Dislocations produced by scratches from the coarser stages of mechanical polishing can be very difficult to identify, particularly as the scratches may themselves have been removed to leave a flat surface. An example of this is seen in Figure 3c in which a strong line can be seen running across the width of the grain to the right of the large central grain, with a few shorter lines parallel to it; along with a further line at about 60° to it. The perfectly straight nature of these lines suggest they are probably the residual effects of scratching damage during an earlier polishing stage which was not removed by the final stage; because hardness varies strongly with orientation (Roebuck *et al.*, 2012) scratches often remain in grains presenting a harder orientation to the surface than in the softer orientations.

A prolonged final polishing stage with colloidal silica can eliminate most scratches but this generally leads to significant differential polishing of the Co and edge rounding on the WC grains. This in turn results in high contrast variation in ECCI and obscures information around the edges of the grain. The ion beam polishing used on the samples in Figures 5 and 6 does appear to eliminate residual scratches with a high degree of confidence but has the downside of producing an irregular wavy surface. This wavy surface produces confusing contrast effects such as the curved arcs and ridges seen in Figures 5a-c, although no evidence was observed to suggest it might itself nucleate dislocations at the ridges formed or elsewhere on the surface.

3.4.2. Subgrain structure

The grain observed in the WC sample with 10wt% Co in the skeleton in Figure 2 has a complex sub structure with multiple subgrains. The WC sample with 11 wt% Co in the skeleton in Figures 5, 6 and 7 show individual grains with distinct sub grains. A lower magnification ECCI image shown in Figure 8 (11wt% Co grade) reveals at least four subgrains with clear boundaries, circled in yellow (including the one shown in Figure 5a, circled in a broken yellow line), and a further three more diffuse regions of misorientation in red boxes. The 2D nature of the images cannot show the full detail of the location of the subgrains relative to all the external boundaries of the enclosing grain in 3D, but three of the four well defined subgrains have a WC-Co boundary in common with the enclosing grain. Only one (the bottom of the four in Figure 7) is fully enclosed within the centre of a WC grain, and it is not possible to tell if it has a common WC-Co boundary above or below the plane of the image.

Two questions are posed by these observations. Firstly, are the sharply defined subgrains the result of grain growth from the subgrain during liquid phase sintering, or the result of absorption of the subgrain by a neighbouring grain of almost identical orientation? Secondly, are the more diffuse subgrains the result of grain growth, or the result of accommodation of stresses during cooling from the sintering temperature?

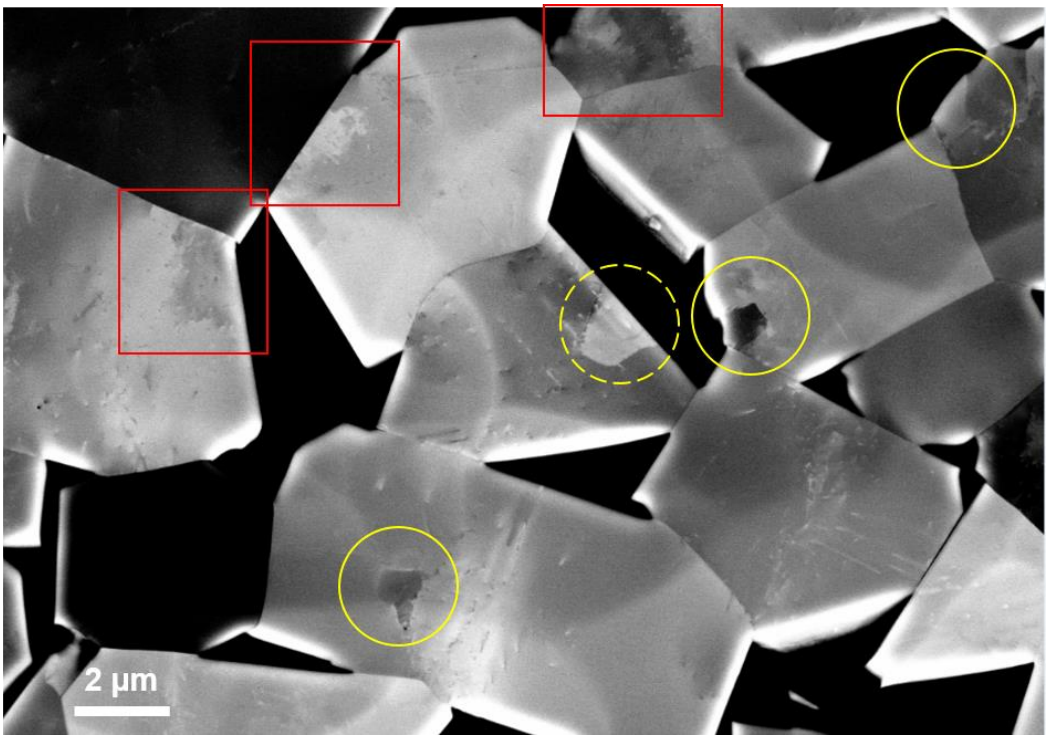

Figure 8. Low magnification ECCI revealing WC subgrains
A low magnification ECC image reveals four subgrains with clear boundaries bound by dislocations, circled in yellow, and a further three more diffuse regions of misorientation in red boxes. The dotted yellow circle indicates the subgrain revealed in figure 4a.

According to the literature, only one previous observation has been reported of subgrains present within WC grains in a WC based hardmetal. Delanoe et al (2007) used TEM to observe one grain enclosing complete three smaller grains and a second grain partly swallowing a smaller grain at a WC-Co boundary (Delanoë *et al.*, 2007). However misorientation in these cases were ≈ 2°, or 3 times larger than the maximum observed here or were actually Σ2 coincidence site lattice (CSL) misorientations. Delanoë suggested the grains were absorbed by abnormal grain growth, whereas the observations here are of grains well within the normal grain size distribution.

A number of studies have investigated the evolution of WC grain shape and size in relationship to the starting powders (e.g. Lay et al. 2008; Pellan et al. 2015; Wang, Fang, and Sohn 2008; Zhong et al. 2011; Kim et al. 2003). In several cases

evidence was found that WC grains develop facets, even in the solid state where WC-Co boundaries develop (Bounhoure *et al.*, 2014), and that the facets affect the growth rates of the grains. However none report on the sub structure or show any evidence for growth from a nucleating grain, although Wang et al. (2008) report coalescence of grains along what may have been special boundaries(Wang *et al.*, 2008). This coalescence would not however lead to absorption of one grain within another to leave only one common WC-Co boundary.

3.4.3. Pattern matching

ECCI is a qualitative technique that allows for imaging defects in the crystal lattice of WC grains. Depending on the diffraction condition, not all defects may be visible. EBSD should reveal all the crystallographic defects in a material, however, this is dependent on the spatial resolution of the EBSD dataset. An advantage of using EBSD and ECCI together is that EBSD can provide quantitative information during interpretation of ECCI data because using pattern matching leads to improved orientation precision. This measurable advantage marks a significant turning point in the type of features identifiable using EBSD. One example of this is the visibility of dislocations in the EBSD data after pattern matching. Data analysis performed by Dr. Winkelmann demonstrates that pattern matching allows for three times the resolution of traditional Hough transform based analysis indicating that minute changes in orientation, such as dislocations, are stored on the EBSPs and resolved using pattern matching. The improvement in orientation precision is consistent with previous pattern matching applications (Friedrich *et al.*, 2018) with a spatial resolution of approximately 100 nm. In Fig. 6, the precision approaches the level of transmission Kikuchi diffraction on the strain field of single dislocations (Yu *et al.*, 2019), where the spatial resolution of TKD is an order of magnitude better than EBSD.

The feasibility of using this technique is dependent on the speed at which pattern matching simulations can take place. The analysis in Dr. Winkelmann's study required a few hours on an advanced computer, demonstrating that this technique does not approach the feasibility of standard indexing for the standard EBSD user. Various other EBSD orientation filtering techniques have been used in the past to improve orientation resolution after Hough-based indexing (Humphreys *et al.*, 2001; Chen & Kuo, 2010; Seret *et al.*, 2019; Hielscher *et al.*, 2019). If the efficiency of post-processing orientation filters rivals the data analysis capabilities of pattern matching, the latter would be moot as it requires significant data processing time and computing power. However, Fig. 4 depicts a WC grain after standard post-processing orientation filtering while Fig. 4b depicts the capability of image processing which removes noise and reveals previously undefined details, such as dislocations. It is clear that post-processing of standard maps does not rival the data analysis capabilities of pattern matching. In essence, ECCI serves as a basis to test the results of pattern matching. For further information on this technique, see Winkelmann et al., 2020.

3.5. Summary

The combination of an ECCI rotation series and EBSD allows for new insights into the presence of subgrains and dislocations in a WC-Co hardmetal sample over a large, in this case 75 µm × 75 µm, field of view. ECCI exposes dislocations within whole grains, ≈ 10-25 µm in diameter and can be used to investigate the properties of a large number of grains in a sample. High precision EBSD data acquired by applying pattern matching to unprocessed EBSPs reveals small changes in crystallographic orientation that result from dislocations and subgrains. This information is verified by ECCI, therefore allowing a second tool, EBSD, to confirm defects in WC's crystal lattice. When used in conjunction with EBSD, ECCI is an effective tool for acquiring information on defects inherent in undeformed material after sintering.

4. Dislocation analysis in basal and prismatic tungsten carbide grains

4.1. Introduction

This study utilizes the scanning electron microscopy (SEM) techniques of electron backscatter diffraction (EBSD) [Randle, 2000; Schwarzer et al., 2009; Wilkinson and Hirsch, 1997] and electron channelling contrast imaging (ECCI) (Wilkinson & Hirsch, 1997; Joy *et al.*, 1982; Simkin & Crimp, 1999; Zaefferer & Elhami, 2014) for studying the dislocations present in as-sintered basal and prismatic, hexagonal tungsten carbide (WC) grains, see Figure 1 for example, in WC-Co hardmetals (cemented carbides).

In indented hexagonal WC grains the established slip plane is $[10\bar{1}0]$ and the slip direction is $[11\bar{2}3]$ (Duszová *et al.*, 2013; Rowcliffe *et al.*, 1988). Dislocations in as-sintered WC grains can be described as resulting from the stress relating to the compression of grains by neighbouring grains, or grain boundary coalescence. Grain boundaries in WC-Co, the rotation angle between grains and the observed grain boundary plane is categorized in detail by Lay and Missiaen, 2014. They discuss how one twist boundary on the $[10\bar{1}0]$ plane shows the most continutity between crystal lattices except at regularly placed steps. These steps are accompanied by dislocations which rectify the c/a ratio. These dislocations on the $[10\bar{1}0]$ plane have a Burgers vector of $^1/_6\langle\bar{1}2\bar{1}3\rangle$. Other dislocations on the $[10\bar{1}0]$ plane have a Burgers vector of $^1/_3\langle\bar{1}2\bar{1}0\rangle$ or $\langle 0001\rangle$ (Vicens *et al.*, 1988). Previous studies have found that many of these boundaries were inherent in the WC powder before sintering (Kim *et al.*, 2005; Kumar *et al.*, 2006; Lay & Loubradou, 2003).

The current model for dislocations and slip in WC is primarily based on studies where WC grains were indented and the induced defects in the crystal lattice were categorized (Takahashi & Freise, 1965; Hibbs & Sinclair, 1981), as discussed in chapter 2. In these studies, the slip system is identified as $[10\bar{1}0]$. Hibbs & Sinclair, 1981; Luyckx, 1970 and Johannesson & Lehtinen, 1973 suggested a slip direction of $\langle 11\bar{2}3\rangle$, Fig. 2b. Reports of dislocations in undeformed WC grains describe dislocations with Burgers vectors of $^1/_3\langle 11\bar{2}0\rangle$ and $\langle 0001\rangle$ (Hibbs & Sinclair, 1981). As most of the work in this field has focused on intentionally damaging WC grains with indenters and observing the induced defects (Rowcliffe *et al.*, 1988; Takahashi & Freise, 1965; Hibbs & Sinclair, 1981; Johannesson & Lehtinen, 1973; Bolton & Redington, 1980), this method does not necessarily describe dislocations inherent in the material after sintering. In undeformed WC grains, dislocations with Burgers vectors of $\langle 0001\rangle$, $^1/_3\langle 1\bar{2}10\rangle$ and $^1/_3\langle 1\bar{2}13\rangle$ are mobile on a variety or dislocation planes (Greenwood *et al.*, 1982).

This chapter uses the novel and non-destructive method for investigating dislocations in WC grains first used by Jablon *et al.*, 2020. This method reduces the need for TEM data acquisition and provides information over much larger areas by the combined use of EBSD and ECCI to study individual dislocations in the WC grain structure of as-synthesized WC grains. EBSD, a SEM based diffraction technique is used to determine crystal orientation and strain in the WC grains. ECCI is also an SEM based diffraction technique which can be used to detect small orientation changes or changes in lattice constant in a material. Extremely small changes in orientation and strain are detectable, revealing subgrains and extended defects such as dislocations and stacking faults (Wilkinson & Hirsch, 1997; Joy *et al.*, 1982; Simkin & Crimp, 1999; Zaefferer & Elhami, 2014). By investigating the contrast exhibited by a defect for different diffraction conditions (Williams & Carter, 2009; Naresh-Kumar *et al.*, 2012) the nature of the defect can be identified.

In this chapter the dislocations in WC grains with surface normals [0001], [$1\bar{1}00$] and [$11\bar{2}0$] are described and where possible the type and ***b***, the Burgers vector of each dislocation are identified. By applying the "invisibility criteria" (Edington, 1976) and techniques previously applied to semiconductor materials (Naresh-Kumar *et al.*, 2012), as described later in this chapter, dislocation types in the basal, [0001], primary prismatic slip, [$1\bar{1}00$] and secondary prismatic, [$11\bar{2}0$] planes can be discussed. Ability to undergo plastic deformation was once attributed to plastic deformation of the soft cobalt phase, but is now attributed to slip deformation within WC (Hibbs & Sinclair, 1981; Johannesson & Lehtinen, 1973; Bolton & Redington, 1980; Mingard & Gee, 2007; Lay *et al.*, 1985). Bolton and Reddington hypothesized and reported slip systems for WC involving prismatic and pyramidal slip planes but do not report on basal slip even though this plane has a high packing density. This chapter describes dislocations revealed by ECCI on basal and prismatic planes in as-sintered WC-Co grains and shows the results from EBSD that may shed light on their origin.

4.2. Sample specifications and experimental details

In this study a coarse-grained WC with 11 wt% Co in the skeleton with a mean grain size or equivalent circle diameter of 4.5 μm was analysed.

Samples were prepared to the standard necessary for EBSD and ECCI acquisition, as discussed in chapter 2.

In this study, ECCI images were acquired at 20 keV and a 10 mm working distance in the backscatter geometry in a Zeiss Auriga FIB SEM using the Zeiss supplied quadrant diode backscattered electron detector which is inserted beneath the pole piece. The sample was tilted by around 20° away from the horizontal to increase the intensity of the backscattered signal. A series of

images of single WC grains were acquired. The grain was rotated 10° between image acquisitions, to obtain an ECCI rotation series data set for [0001] $[1\bar{1}00]$ and $[11\bar{2}0]$ oriented grains. At the time of measurement, it was not possible to precisely determine the diffraction conditions for each image acquisition. Diffraction conditions can be determined through the acquisition of local area electron channelling patterns, but this requires local "rocking" of the beam (Wilkinson & Hirsch, 1997) which was not possible in the SEM used for acquisition of this data set. For this work the diffraction conditions for a few of the ECCI micrographs were estimated from the orientation of the sample. A more precise determination of diffraction conditions for a range of ECCI micrographs for identification of individual defects will be the subject of future work.

EBSD data in this study was collected in a Zeiss Auriga FIB SEM outfitted with an Oxford NordlysNano system. EBSD maps were acquired at 20 or 30 kV accelerating voltage with a 10 nA beam and the sample tilted at 70° from the horizontal. EBSD maps are acquired over 400 × 300 μm areas, Figure 1a. Figure 1a is an EBSD pattern quality map, a map that reflects the "quality" or "sharpness" of the diffraction bands in the EBSP acquired at each pixel. Grains with simple orientations, that is grains whose normals lie close (within 3-5°) of one of the principal crystallographic axes [0001], $[1\bar{1}00]$, $[11\bar{2}0]$, were identified from inverse pole figures such as the one shown in Figure 1b. Figure 1b shows those grains whose normals are close to [0001]. These grains are coloured red in the EBSD quality map of Figure 1a. The crystal orientation of a [0001] grain (circled in black in Figure 1a) is depicted in Figure 1c. The blue line on this grey hexagon is indicative that the (0001) plane normal is perpendicular to the detector. The red lines extending from the 120° angles of the hexagon indicate that the $\{11\bar{2}0\}$ planes are in the plane of the detector. The electron backscatter pattern (EBSP) of this [0001] oriented grain is found in Figure 1d. An Inverse Pole Figure (IPF-Z) map of this [0001] oriented grain and crystallographic

directions are shown in Figure 1e. The corresponding electron channelling contrast imaging (ECCI) image is found in Figure 1f. The triangular shape of this prismatic grain, is characteristic of [0001] oriented grains (Lay & Loubradou, 2003).

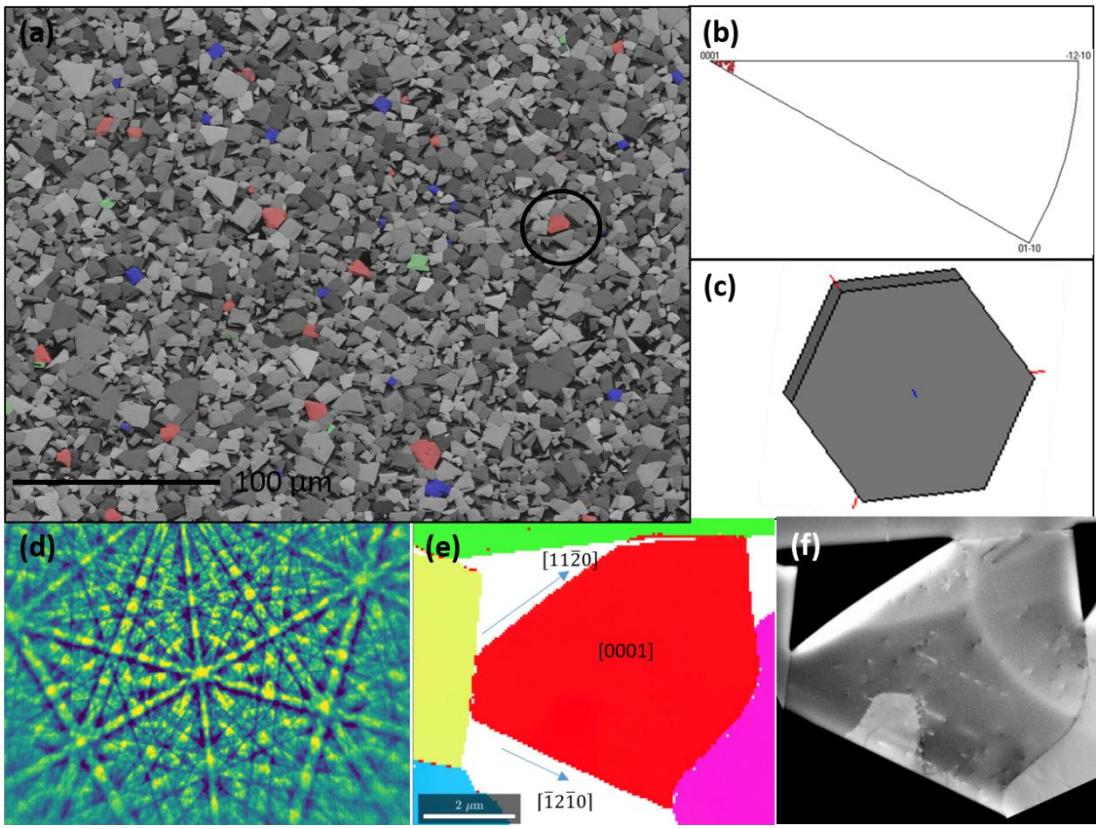

Figure 1. Identifying WC grains close to the [0001] sample normal
(a) A large area EBSD pattern quality map. The red grains are those identified with the IPF pole figure as having a sample normal close to [**0001**]*, the blue grains have a sample normal close to* [**10$\bar{1}$0**] *and the green grains have a sample normal close to* [**11$\bar{2}$0**].
(b) IPF pole figure highlighting grains with a sample normal close to [**0001**],
(c) Orientation of the [0001] grain circled in black in Fig. 1a
(d) EBSP of the grain circled in black in Fig. 1a
(e) EBSD IPF map of the grain circled in black in Fig. 1a and the corresponding crystallographic directions,
(f) ECCI of the grain circled in black in Fig. 1a.
(The scale bar is the same for (e) and (f).)

As discussed in Chapter 2, electron channelling contrast images (ECCI) are generated when electrons are diffracted by crystal planes in an appropriately oriented sample. Small changes in crystallographic orientation or defects in the crystal lattice are reflected in variations in contrast within the image. Recording the intensity in backscattered elections across a sample surface produces an electron channelling contrast image (Naresh-Kumar *et al.*, 2012). Such small

changes in orientation and strain are revealed in this technique that rotation boundaries and individual dislocation can be resolved.

4.3. Results and discussion

After identifying grains with the [0001], [$1\bar{1}00$] and [$11\bar{2}0$] axes normal to the sample, ECCI rotation series were acquired for each crystallographic orientation. Figure 2 shows examples of three grains respectively oriented with the [0001], [$1\bar{1}00$], [$11\bar{2}0$], axes normal to the sample. Dislocations are revealed in the ECCI micrographs intersecting the surface as seen in Figure 2.

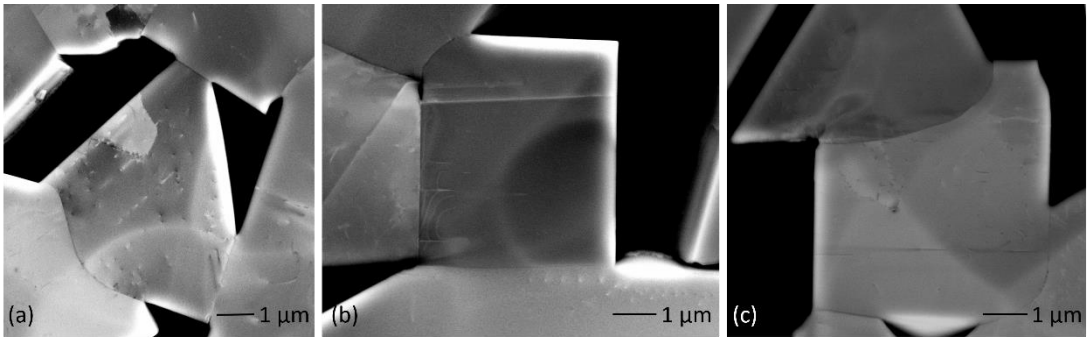

Figure 2. Dislocations as revealed by ECCI in three grains
(a) [**0001**] *oriented grain*
(b) [**$1\bar{1}$00**] *oriented grain*
(c) [**$11\bar{2}$0**] *oriented grain.*

Figure 3 shows four images from a rotation series acquired from the [0001] oriented crystal. The [$1\bar{1}00$] and [$11\bar{2}0$] directions were determined from EBSD mapping using the techniques described above. The images in Figures 3 have been aligned so that they are parallel with each other. Figure 3a was acquired at a random orientation. Figure 3b is labelled as 0° since it was acquired with the [$1\bar{1}00$] grain edge and image edge parallel to the scanning direction. Thus to a first approximation, the diffraction **g**-vector selected was close to ($11\bar{2}0$). Figure 3c was acquired with the sample at 30° to Fig. 3b, and thus to a first approximation, according to Figure 1d, the selected **g**-vector was close to

$(10\bar{1}0)$. Figure 3d was acquired with the sample rotated 60° from Figure 3c and is marked 90°. Thus to a first approximation, the selected **g**-vector was close to $(1\bar{1}00)$. From **g·b** analysis, for **g** = $(11\bar{2}0)$, all dislocations with Burgers vectors of $^1/_3\langle 11\bar{2}0\rangle$ or $^1/_3\langle 11\bar{2}3\rangle$ are visible.

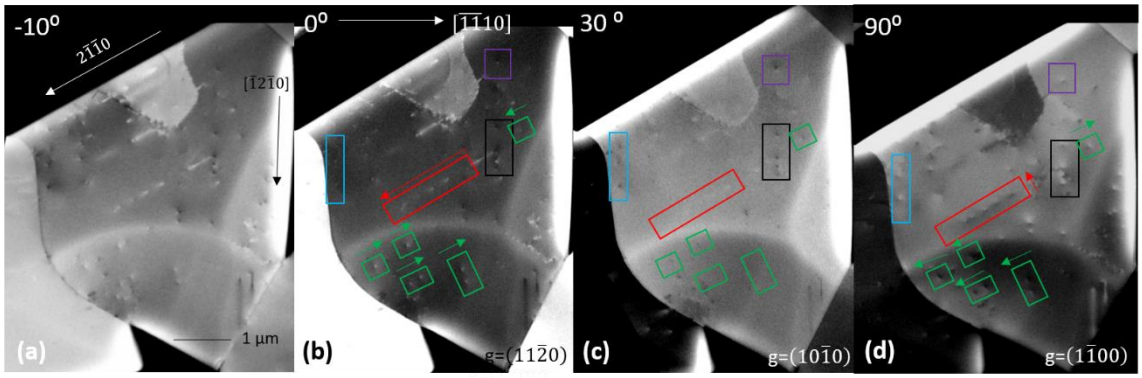

Figure 3. Dislocations as revealed by ECCI in a [0001] oriented grain.
(a) random orientation with arrows indicating crystal directions
(b) 0° rotation (c) 30° rotation
(d) 90° rotation.
Directions of the grain were determined using Fig. 1(e). Green boxes indicate dislocations with B-W contrast that rotates by 180° between Fig. 3(b) and 3(d). Red boxes indicate dislocations with B-W contrast that rotates by an angle other than 180° between Fig. 3(b) and 3(d). Black boxes indicate dislocations with B-W contrast whose rotation between Fig. 3(b) and 3(d) cannot be determined. These dislocations are present in Figs. 3(a)-(d). The blue boxes indicate dislocations prominent in Fig. 3(c) but not in Figs. 3(b) and 3(d). The purple boxes indicate a dislocation with B-W contrast that rotates by 180° between Fig. 3(b) and 3(d) and remains visible in Fig. 3(c).

Most of the dislocations propagating at, or around 90° to the surface of the grain appear to be mixed dislocations, as the black-white (B-W) contrast exhibited by the dislocations is observed to rotate by an angle other than 180° (which would be a reverse of contrast) on comparing the two ECCI images (and on comparing with other ECCI images from the rotation series). The dislocations outlined by green boxes appear to be edge dislocations. Their B-W contrast appears to reverse on comparing the two ECCI images. Applying the invisibility criterion and analysis of their B-W contrast direction implies **b** = $^1/_3[\bar{1}2\bar{1}0]$ or

$^1/_3$ [$1\bar{2}10$], table 1. Note that ***g*·*b*** is of opposite sign for **g** = ($11\bar{2}0$) and **g** = ($1\bar{1}00$) (-1 or +1) for these dislocations which explains the reversal of contrast. It is also interesting to note that the sub-grain present in the top of the image appears dark in the **g** = ($11\bar{2}0$) image, but bright in the **g** = ($1\bar{1}00$) image. This subgrain is surrounded by dislocations. This can be accounted for by which side of the selected Kikuchi band is giving rise to the contrast, as diffraction conditions are only approximate. Note that while some dislocations are configured in a line, most obviously those outlined by a red rectangle, nearly all the dislocations appear as individual defects terminating on the grain's surface. The majority of the dislocations in this grain align along either the {$\bar{1}2\bar{1}0$} or {$11\bar{2}0$} directions. Both (hkil) (4 indices) and (hkl) (3 indices) and [UVTW] (4 indices) and [uvw] (3 indices) are listed to describe ***g*** and ***b*** respectively in Table 1, where the dot product ***g*** · ***b*** is calculated using (hkl) and [uvw] respectively.

Table 1. Summarizing $g \cdot b$ analysis for grain shown in Figure 3.

g	$b = {}^1/_3$ [0003][003]	$b = {}^1/_3\langle 11\bar{2}0\rangle$ [330]		
		$= {}^1/_3$ [$11\bar{2}0$][330]	$^1/_3$ [$\bar{1}2\bar{1}0$] [030]	$^1/_3$ [$\bar{2}110$] [$\bar{3}00$]
($11\bar{2}0$)/(110) ($10\bar{1}0$)/(100) ($1\bar{1}00$)/($1\bar{1}0$)	$g \cdot b$ = 0 (invisible) $g \cdot b$ = 0 (invisible) $g \cdot b$ = 0 (invisible)	$g \cdot b$ = 2 (visible) $g \cdot b$ = 1 (visible) $g \cdot b$ = 0 (invisible)	$g \cdot b$ = 1 (visible) $g \cdot b$ = 0 (invisible) $g \cdot b$ = -1 (visible)	$g \cdot b$ = -1 (visible) $g \cdot b$ = -1 (visible) $g \cdot b$ = -2 (visible)

g	$b = {}^1/_3\langle 11\bar{2}3\rangle$ [333]					
	$^1/_3$ [$11\bar{2}3$] [333]	$^1/_3$ [$11\bar{2}\bar{3}$] [$33\bar{3}$]	$^1/_3$ [$1\bar{2}13$] [$0\bar{3}3$]	$^1/_3$ [$1\bar{2}1\bar{3}$] [$0\bar{3}\bar{3}$]	$^1/_3$ [$\bar{2}113$] [$\bar{3}03$]	$^1/_3$ [$\bar{2}11\bar{3}$] [$\bar{3}0\bar{3}$]
($11\bar{2}0$)/(110) ($10\bar{1}0$)/(100) ($1\bar{1}00$)/($1\bar{1}0$)	$g \cdot b$ = 2 (visible) $g \cdot b$ = 1 (visible) $g \cdot b$ = 0 (invisible)	$g \cdot b$ = 2 (visible) $g \cdot b$ = 1 (visible) $g \cdot b$ = 0 (invisible)	$g \cdot b$ = -1 (visible) $g \cdot b$ = 0 (invisible) $g \cdot b$ = 1 (visible)	$g \cdot b$ = -1 (visible) $g \cdot b$ = 0 (invisible) $g \cdot b$ = 1 (visible)	$g \cdot b$ = -1 (visible) $g \cdot b$ = -1 (visible) $g \cdot b$ = -1 (visible)	$g \cdot b$ = -1 (visible) $g \cdot b$ = -1 (visible) $g \cdot b$ = -1 (visible)

Figure 4 shows three images from a rotation series acquired from the [$1\bar{1}00$] oriented grain shown in Figure 2b. The images in Figure 4 have been aligned so that they are parallel with the middle image (Figure 4b). This image is labelled as 0° since it was acquired with the grain edges parallel and perpendicular to the image edge and thus to the scanning direction. Thus to a first approximation, the diffraction ***g***-vector selected was close to (0002). The image on the right, Figure 4c, was acquired with the sample at 90° to the middle image,

and thus to a first approximation, the selected ***g***-vector was close to [11$\bar{2}$0]. The left hand image Figure 4a was acquired for the crystal at -50° from the middle image and represents a random unknown diffraction condition.

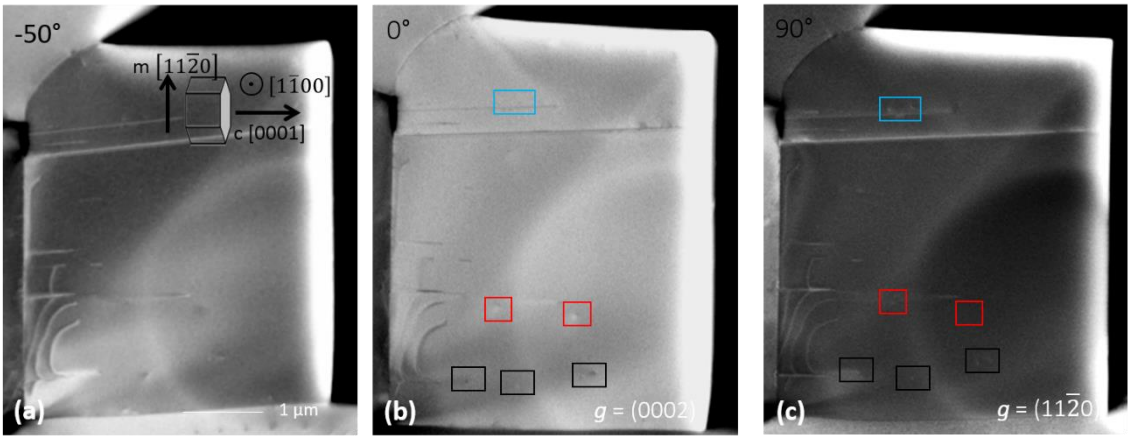

Figure 4. Dislocations as revealed by ECCI in a [1$\bar{1}$00] oriented grain.
(a) -50° rotation
(b) 0° rotation
(c) 90° rotation
The significance of the coloured boxes is discussed in the text.

On this primary prismatic plane, three types of dislocations are present. These are outlined by coloured rectangles. There are a number of dislocations visible in the middle image (Figure 3b) which are not visible in the right-hand image (Figure 3c), these are highlighted by the red box in Figure 3b and 5c. These dislocations satisfy the condition $\boldsymbol{g} \cdot \boldsymbol{b} \neq 0$ when ***g*** is (11$\bar{2}$0), (See Table 2) and $\boldsymbol{b} = {}^{1}/_{3}\langle 11\bar{2}0\rangle$. There are also dislocations which appear in the right-hand image (Figure 3c) but are very faint in the middle image (Figure 3b), these are highlighted by the blue boxes in Figure 3b and 3c. These dislocations satisfy the condition $\boldsymbol{g} \cdot \boldsymbol{b} \neq 0$ when ***g*** is (0002), (See Table 2) and b=⟨0001⟩. There are also dislocations which appear in both the middle and right-hand images and these are highlighted by the black box in Figure 3b and 3c. These dislocations satisfy the condition $\boldsymbol{g} \cdot \boldsymbol{b} \neq 0$ when ***g*** is (11$\bar{2}$0) and (0002), (See Table 2) when b=${}^{1}/_{3}\langle 11\bar{2}3\rangle$. Both (hkil) (4 indices) and (hkl) (3 indices) and [UVTW] (4

indices) and [uvw] (3 indices) are listed to describe $\boldsymbol{g}$ and $\boldsymbol{b}$ respectively in Table 2, where the dot product $\boldsymbol{g} \cdot \boldsymbol{b}$ is calculated using (hkl) and [uvw] respectively.

Table 2. Summarizing $\boldsymbol{g} \cdot \boldsymbol{b}$ analysis for grain shown in Figure 4.

g	$b = {}^1/_3\langle 11\bar{2}0\rangle$ [330]					
	$= {}^1/_3\langle 11\bar{2}0\rangle$ [330]		${}^1/_3$ [$\bar{1}2\bar{1}0$] [030]		${}^1/_3$ [$\bar{2}110$] [$\bar{3}\bar{3}0$]	
(0002)(002) (11$\bar{2}$0)/(110)	$g \cdot b$ = 2 (visible) $g \cdot b$ = 0 (invisible)		$g \cdot b$ = 0 (invisible) $g \cdot b$ = 2 (visible)		$g \cdot b$ = 0 (invisible) $g \cdot b$ = 1 (visible)	
g	$b = {}^1/_3\langle 11\bar{2}3\rangle$ [333]					
	${}^1/_3$ [11$\bar{2}$3] [333]	${}^1/_3$ [11$\bar{2}\bar{3}$] [33$\bar{3}$]	${}^1/_3$ [1$\bar{2}$13] [0$\bar{3}$3]	${}^1/_3$ [1$\bar{2}\bar{1}\bar{3}$] [0$\bar{3}\bar{3}$]	${}^1/_3$ [$\bar{2}$113] [$\bar{3}$03]	${}^1/_3$ [$\bar{2}\bar{1}\bar{1}\bar{3}$] [$\bar{3}\bar{0}\bar{3}$]
(0002)(002) (11$\bar{2}$0)/(110)	$g \cdot b \neq 2$ (visible) $g \cdot b \neq 2$ (visible)	$g \cdot b$ = -2 (visible) $g \cdot b$ = 2 (visible)	$g \cdot b$ = 2 (visible) $g \cdot b$ = -1 (visible)	$g \cdot b$ = -2 (visible) $g \cdot b$ = -1 (visible)	$g \cdot b$ = 2 (visible) $g \cdot b$ = -1 (visible)	$g \cdot b$ = -2 (visible) $g \cdot b$ = -1 (visible)

The most obvious dislocations observed in Figure 4 for the [1$\bar{1}$00] oriented grain, are the straight lines which propagate across the grain from the left-hand side of the grain in the [0001] direction. On careful inspection of Figure 4, some of these lines seem to originate from lines propagating in the [11$\bar{2}$0] direction at the interface between the [1$\bar{1}$00] oriented grain and its neighbour. These dislocations may be dislocations lying in the *c*-plane, from $\boldsymbol{g} \cdot \boldsymbol{b}$ analysis their $\boldsymbol{b}$-vector is either $\pm {}^1/_3$ [11$\bar{2}$0]. As they have a line direction of [11$\bar{2}$0], this indicates they are screw dislocations. These dislocations then "bend" to take up a line direction of [0001]. A $\boldsymbol{g} \cdot \boldsymbol{b}$ analysis of the dislocations propagating in the [0001] direction suggests that these are mixed dislocations, as they are visible for $\boldsymbol{g}$ is (11$\bar{2}$0) and $\boldsymbol{g}$ is (0001).

Figure 5 shows three images from a rotation series acquired from the [11$\bar{2}$0] oriented crystal shown in Figure 2c. The facets visible on the grain were within 0.2° of being perpendicular to each other, according to the analysis of Winkelmann et al., 2020. This is expected for such an orientation and gives some degree of confidence in assigning the [1$\bar{1}$00] and [0001] directions determined from EBSD mapping to be parallel to the edges of the grain. The images in Figure

5 have been aligned so that they are parallel with the middle image. This image is labelled as 0° since it was acquired with the grain edges parallel and perpendicular to the image edge and thus to the scanning direction. Thus to a first approximation, the diffraction **g**-vector selected was close to $[1\bar{1}00]$. The image on the right was acquired with the sample at 90° to the middle image, and thus to a first approximation, the selected **g**-vector was close to (0002). The left hand image was acquired for the crystal at -20° from the middle image and represents a random unknown diffraction condition.

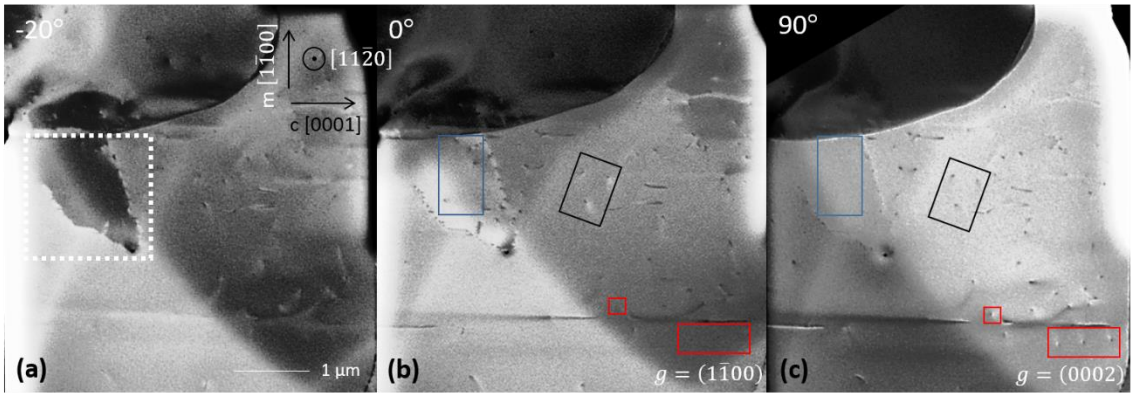

Figure 5. Dislocations as revealed by ECCI in a $[11\bar{2}0]$ oriented grain.
(a) -20° rotation
(b) 0° rotation
(c) 90° rotation.
The significance of the coloured boxes is discussed in the text.

There are a number of dislocations visible in the middle image (Figure 5b) which are not visible in the right-hand image (Figure 5c), these are highlighted by the blue box in Figure 5b and 5c. There are also dislocations which appear in the right-hand image (Figure 5c) but are very faint in the middle image (Figure 5b), these are highlighted by the red boxes in Figure 5b and 5c. There are also dislocations which appear in both the middle and right-hand images and these are highlighted by the black box in Figure 5b and 5c. The dislocations in the blue box, visible in the middle image (Figure 5b), but not visible in the right-hand image (Figure 5c) (blue box) satisfy the condition $\boldsymbol{g} \cdot \boldsymbol{b} \neq \mathbf{0}$ when $\boldsymbol{g}$ is $(1\bar{1}00)$ and $\boldsymbol{g} \cdot \boldsymbol{b} = \mathbf{0}$ when $\boldsymbol{g}$ is (0002). This observation is consistent with these dislocations being mixed dislocations with $\boldsymbol{b} = {}^{1}/_{3}[\bar{1}2\bar{1}0]$ or $\boldsymbol{b} =$

$^1/_3$ [$\bar{2}$110] (See Table 3) (Kong *et al.*, 2012). Similar analysis can be applied to the dislocations highlighted by the red boxes: $\boldsymbol{b}$ = [0001] (edge) or $\boldsymbol{b}$ = $^1/_3$ [11$\bar{2}$3]) (mixed) and to the dislocations highlighted by the black box $\boldsymbol{b}$ = $^1/_3$ [$\bar{1}$2$\bar{1}$3]) (mixed) or b = $^1/_3$ [$\bar{2}$113]) (mixed). Both (hkil) (4 indices) and (hkl) (3 indices) and [UVTW] (4 indices) and [uvw] (3 indices) are listed to describe $\boldsymbol{g}$ and $\boldsymbol{b}$ respectively in Table 3, where the dot product $\boldsymbol{g} \cdot \boldsymbol{b}$ is calculated using (hkl) and [uvw] respectively, as was the case for Tables 1 and 2. In this study, evidence of dislocations along subgrain boundaries is found in Figures 3a and 3c. Dislocations along subgrain boundaries are clear in the three diffraction conditions in Figure 5.

Table 3. Summarizing $\boldsymbol{g} \cdot \boldsymbol{b}$ analysis for grain shown in Figure 5.

g				
	$b = ^1/_3$ [$\bar{1}$2$\bar{1}$0]([030]) mixed dislocations	$b = ^1/_3$ [$\bar{2}$110] ([$\bar{3}$00]) mixed dislocations	b = [0001] ([001]) edge dislocations	$b = ^1/_3$ [11$\bar{2}$3] ([333]) mixed dislocations
[1$\bar{1}$00] ([1$\bar{1}$0]) [0002] ([002])	$g \cdot b$ = -1 (visible) $g \cdot b$ = 0 (invisible)	$g \cdot b$ = -1 (visible) $g \cdot b$ = 0 (invisible)	$g \cdot b$ = 0 (invisible) $g \cdot b$ = 2 (visible)	$g \cdot b$ = 0 (invisible) $g \cdot b$ = 2 (visible)

g			
	$b = ^1/_3$ [$\bar{1}$2$\bar{1}$3] ([033]) mixed dislocations	$b = ^1/_3$ [$\bar{2}$113] ([$\bar{3}$03]) mixed dislocations	$b = ^1/_3$ [11$\bar{2}$0]([330]) screw dislocations
[1$\bar{1}$00] ([1$\bar{1}$0]) [0002] ([002])	$g \cdot b$ = -1 (visible) $g \cdot b$ = 2 (visible)	$g \cdot b$ = -1 (visible) $g \cdot b$ = 2 (visible)	$g \cdot b$ = 0 (invisible) $g \cdot b$ = 0 (invisible)

Dislocations are primarily observed coming up to the surface of the grain in the [0001] oriented grain, dislocations run parallel to the grain's surface in the [1$\bar{1}$00] oriented grain, and a mixture of dislocations coming up to the surface of the grain and dislocations running parallel to the grain's surface in the [11$\bar{2}$0] oriented grain. Slip systems describe the set of planes and associated directions upon which dislocations and plastic deformation occur. When an external force acts upon a material, parts of the crystal lattice glide along each other (Hull & Bacon, 2001*a*). Depending on the crystal lattice and the material, different slip systems can manifest themselves. This may be due to the very low, and non-

idealized c/a ratio of 0.98 which is manifested with a denser-than-usual packing density on the prismatic planes.

According to the literature, there are three primary reasons why dislocations are present in as-sintered WC grains. Dislocations exist in the WC powder before liquid phase sintering (Lay, 2013; Zhimin *et al.*, 2000). As the WC grains precipitate out of solution after sintering, grains may be subsumed by other grains and dislocations appear along the border of the primary grain and the subgrain (Jablon *et al.*, 2020; Lay *et al.*, 1985). Additionally, dislocations are present in WC grains to accommodate the boundary between a WC grain and its neighbours, these neighbours include both the greater WC skeleton and the cobalt matrix (Lee & Gurland, 1978; Farooq, M.U.; Klement, 2004). In this study, evidence of dislocations along subgrain boundaries is found in Figures 3a and 3c. The interaction between neighbouring WC grains, Figures 2a, 2b and 2c, corroborates previous work on the presence of dislocations along grain boundaries. EBSD data indicates that a number of dislocations observed in the present work are a result of the strain induced by neighbouring grains as seen in Figure 6. Figure 6b shows the value of the rotation angle around Y in the $[11\bar{2}0]$ map, relative to the reference orientation at the position marked on Figure 6a. This seems to indicate a systematic rotation of the grain around [0001], which is along the Y axis in the map. The colour map, Figure 6c (grain reference orientation deviation map) is relative to the reference orientation in Figure 6a and shows slight changes in orientation throughout the grain as seen in the drift along the lower edge of the colour key in Figure 6c.

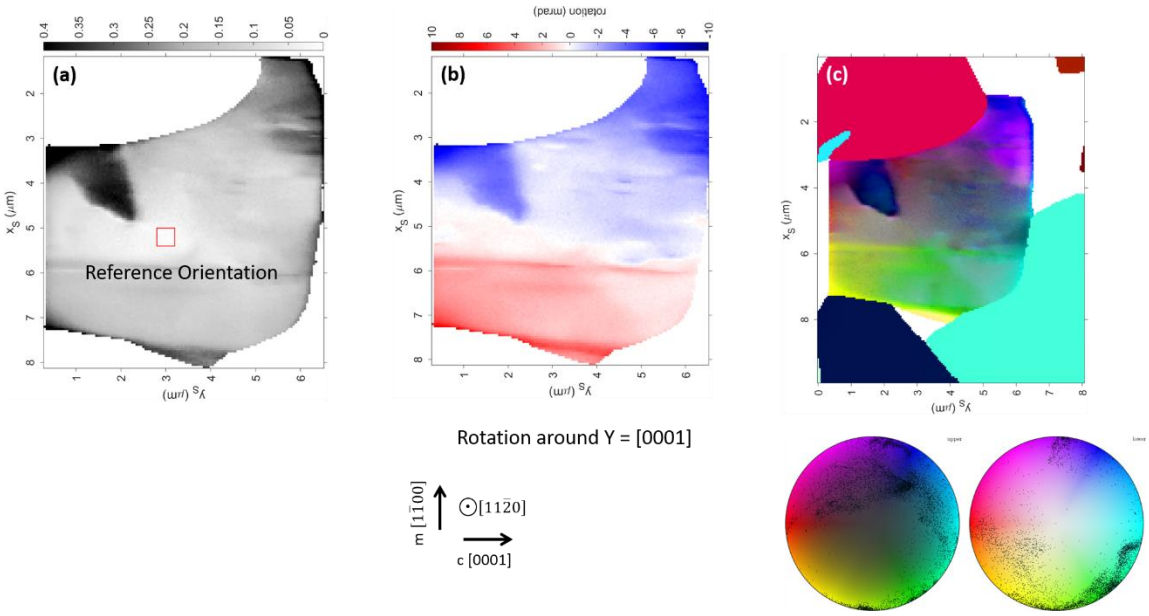

Figure 6. Dislocations revealed by EBSD using pattern matching in a [11$\bar{2}$0] oriented grain.
(a) Grain reference orientation deviation (GROD) map. Each pixel has a value (in degrees) equal to the disorientation that pixel has with the mean orientation of each grain.
(b) value of rotation angle around the Y axis relative to a reference orientation
(c) Grain reference orientation deviation axis (GROD axis) map. Each pixel has a value denoting the rotation axis with respect to the mean, as defined by the key to the left of the image. The black dots in the key denote the directions for each point on the map.

The data in this study agrees with previous studies on defects inherent in undeformed WC grains where reports of dislocations in undeformed WC grains describe dislocations with Burgers vectors of ⟨0001⟩, $^1/_3\langle 11\bar{2}0\rangle$ and $^1/_3\langle 11\bar{2}3\rangle$ are identified in the text (Hibbs & Sinclair, 1981). Previous work suggests that undissociated dislocation with b=⟨0001⟩ and $^1/_3\langle 11\bar{2}0\rangle$ are expected in as-sintered WC grains. This study reports that dislocation with b= $^1/_3\langle 11\bar{2}3\rangle$ remain in the as-sintered WC as well.

4.4. Conclusions

Combining ECCI and EBSD allows for new insights into defects and dislocations characteristic of WC grains of particular crystallographic orientation. In this study, dislocations and their Burgers vectors are described allowing for interpretation and discussion of dislocations in basal and prismatic grains of WC. This is a new approach which can help explain how WC deforms plastically by describing dislocations inherent in undeformed WC grains. Future work will study and catalogue similar dislocations on basal and prismatic planes under more precise diffraction conditions.

5. Crystallographic defects in indented tungsten carbide grains

5.1. Introduction

The purpose of the present study is to explore and compare defects in the crystal lattice of as-sintered and intentionally damaged WC grains and builds upon the work presented in chapters 3 and 4. This chapter discusses the slip systems observed in indented WC grains on the basal and prismatic planes. The significance of understanding these deformation mechanisms can be found in chapter 2. Previous TEM studies describe the deformation mechanisms, specifically the slip systems in damaged WC grains. Below, multiple grains with surface normals [0001], $[1\bar{1}00]$ and $[11\bar{2}0]$ were intentionally damaged and the induced defects in the crystal lattice are analysed using ECCI and discussed.

5.2. Slip plane identification in the literature

Deformation in WC grains has mostly been discussed in the literature through the lens of indents on various crystal planes after TEM analysis. Slip lines were first observed around hardness indents in single crystals of WC (Takahashi & Freise, 1965). In the first studies on this material, the primary prismatic plane, $[10\bar{1}0]$ was found to be the slip plane (Takahashi & Freise, 1965; French, D.N. and Thomas, 1965) with formation of dislocations with Burgers vectors of $\langle 0001 \rangle$ and $^1/_3 \langle 11\bar{2}0 \rangle$. Subsequent studies identified the slip system around indents on the $[10\bar{1}0]$ plane and partial dislocations with Burgers vectors of $^1/_6 \langle 11\bar{2}3 \rangle$ (Luyckx, 1970; Johannesson & Lehtinen, 1971). Later, Bolton & Redington, 1980 studied plastically deformed WC grains and identified slip on the $[10\bar{1}0]$ plane and again suggested extended dislocations formed by the dissociation of $^1/_3 \langle 11\bar{2}3 \rangle$ dislocations.

The primary prismatic plane is a surprising slip plane for a hexagonal material. WC is characterized by extreme anisotropy and a rigidly ordered lattice, leading to a low c/a ratio. These two characteristics of the material lead to slip behaviour that is unlike that in the ideal hexagonal materials (Bolton & Redington, 1980). This is evident in the observed slip system in WC. Most hexagonal materials experience slip on the basal plane, the plane with the highest packing density. In WC, slip is most commonly observed on the prismatic and pyramidal planes. One suggestion for this observation is that strong interatomic bonds exist on the basal plane between the tungsten and carbon atoms across the ABAB layers. This prevents slip on the basal plane (Bolton & Redington, 1980).

The following Burgers vectors can be found during slip on the prismatic $[10\bar{1}0]$ plane; $\boldsymbol{b} = \langle 0001 \rangle$, $\boldsymbol{b}={}^{1}/_{3}\langle 11\bar{2}3\rangle$ *and* $\boldsymbol{b} = {}^{1}/_{3}\langle 2\bar{1}\bar{1}0\rangle$. Dislocations with $\boldsymbol{b} = \langle 0001 \rangle$ can dissociate on the $\{11\bar{2}0\}$ secondary prismatic plane into partials of ${}^{1}/_{6}\langle \bar{2}023\rangle + {}^{1}/_{6}\langle 20\bar{2}3\rangle$. On the pyramidal plane, $\{2\bar{1}\bar{1}2\}$, dislocations with $\boldsymbol{b} = {}^{1}/_{3}\langle \bar{2}113\rangle$ have been observed. These dislocations can cross slip into the primary prismatic and pyramidal planes (Bolton & Redington, 1980). Bolton and Reddington also identified the first dislocations observed in indented WC grains.

Hibbs & Sinclair, 1981 observed dislocations with $\boldsymbol{b} = \langle 0001 \rangle$, $\boldsymbol{b} = {}^{1}/_{3}\langle 2\bar{1}\bar{1}0\rangle$ *and* $\boldsymbol{b} = {}^{1}/_{3}\langle 11\bar{2}3\rangle$. Dislocations with Burgers vectors of $\boldsymbol{b} = \langle 0001 \rangle$, $\boldsymbol{b} = {}^{1}/_{3}\langle 2\bar{1}\bar{1}0\rangle$ were the most common. Later studies of subgrain boundaries in WC deformed at high temperatures describe tilt subgrain boundaries formed by a family of perfect dislocations composed of $\boldsymbol{b} = \langle 0001 \rangle$, $\boldsymbol{b} = {}^{1}/_{3}\langle 2\bar{1}\bar{1}0\rangle$ *and* $\boldsymbol{b} = {}^{1}/_{3}\langle 11\bar{2}3\rangle$. Lay in 1985 found that most of the observed subgrains have rotation angles close to 1° and consisted of a single array of dislocations (Lay *et al.*, 1985). A few of them were entirely contained within a grain, leading to highly strained regions. Most subgrains were found on WC

grain boundaries. The defects resulting from plastic deformation were partial dislocations of $\boldsymbol{b} = {}^{1}/_{6}\langle 11\bar{2}3\rangle$.

Rowcliffe et al. discussed deformation and fracture in 1988. They describe the primary slip mechanism as slip on the $[10\bar{1}0]$ plane in the $\langle 11\bar{2}3\rangle$ direction by the motion of identical $\langle {}^{a}/_{6}\rangle[11\bar{2}3]$ partials. On the basal plane, indentation with Vickers and spherical indenters leads to cracks with intersecting slip bands on the $\{11\bar{2}0\}$ and $\{10\bar{1}0\}$ planes. A quarter century later, another study on nanoindentation in WC, explored identifying defects in indented WC grains using a Berkovich indenter. EBSD was used to obtain information on crystallographic orientation for subsequent hardness analysis. Slip lines were found in all WC grains within 100 μm^3 of the indent. The study found that deformation was dependent on the position of the indenter in the grain and crystallographic orientation. In the [0001] oriented grain, slip lines were visible in all three equivalent $\langle 10\bar{1}0\rangle$ directions (Duszová *et al.*, 2013).

5.3. Sample specifications and experimental details

Samples were prepared to the standard necessary for EBSD and ECCI acquisition, as discussed in chapter 2.

5.3.1. Choosing grains for analysis

The grains in this study were chosen using the method described in chapters 2, 3 and 4. EBSD maps of 400 × 300 μm areas were collected. Grains with simple orientations, that is grains whose normal lies close (within 3-5°) to one of the principal crystallographic axes $[0001], [1\bar{1}00], [11\bar{2}0]$ were identified from inverse pole figure keys, Figure 1a. These grains were subsequently identifiable on a backscatter electron image, Figure 1b. ECCI data were collected from five grains of each of the crystallographic orientations, labelled one through five on

Figure 1b for a total of 15 images. From this data, two grains of each orientation, a total of six grains, were chosen based on their size, exceptional polishing and lack of pre-existing dislocations. The sample was then removed from the SEM and imaged using an optical microscope. The grains of interest were identified in the optical microscope so they could be found in the nanoindenter.

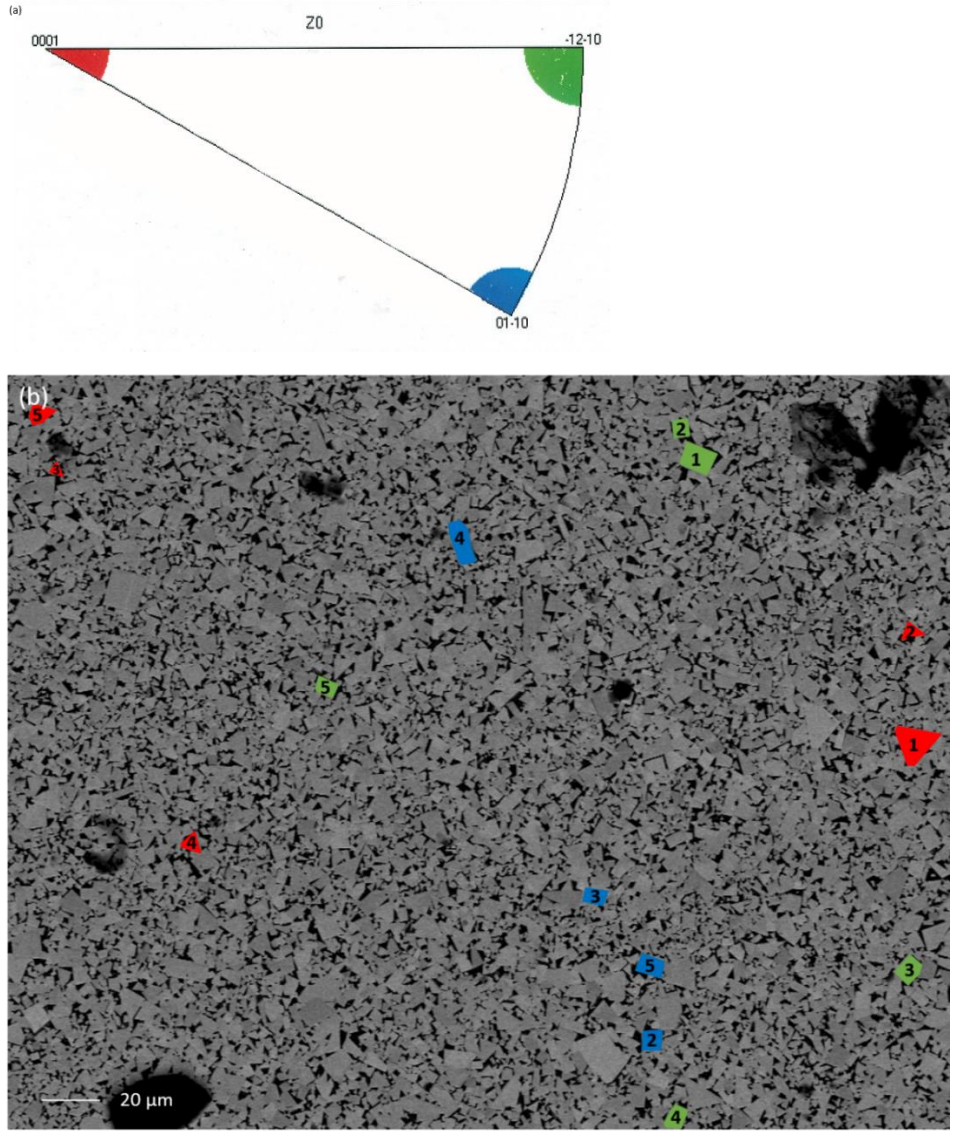

Figure 1. Identifying [0001], [1$\bar{1}$00], [11$\bar{2}$0] oriented grains
(a) IPF pole figure highlighting grains, in red, green and blue, whose normal lies close to one of the principal crystallographic axes. ECCI image before indentation (b) A large area backscatter electron map where the grains coloured red, blue and green are those identified with the IPF pole figure as having a sample normal close to **[0001]**, **[1$\bar{1}$00]**, **[11$\bar{2}$0]** *respectively.*
Note that grain 1 in the **[1$\bar{1}$00]** data series exceeded the boundaries of this image.

5.3.2. Indenting WC grains

The sample was indented using a nanoindentation system (Nanotest Xtreme, Micro Materials, UK) equipped with a Berkovich indenter. The Berkovich indenter is a three-sided pyramidal tip. More detail on this indenter is provided in Chapter 2. Berkovich indenters are often chosen for nanoindentation tests because it has an apex that is particularly sharp, generally < 20 nm (MM Khrushchov, 1951). After indentation, the samples were returned to the FEG SEM and new ECCI and EBSD data were collected.

5.4. Results and Discussion

5.4.1. ECCI and EBSD of [0001], $[1\bar{1}00]$ and $[11\bar{2}0]$ oriented grains using a Berkovich indenter

5.4.1.1. [0001]

Two grains with surface normal of [0001] were indented with a Berkovich indenter. In Figure 2a, the WC grain is shown before indentation. The region of interest where the grain was subsequently indented is expanded in Figure 2b. Note that there are no visible dislocations on the sample surface, but ample damage is visible due to sample polishing. Grain hardness varies with sample orientation (Roebuck *et al.*, 2012), so preferential damage to grains of a particular orientation, here on the basal plane, is very common. In Figure 2c, a pattern quality image, as generated from EBSD patterns, depicts this grain after indentation. The pattern quality appears to be uniform across the grain aside from a scratch below the indent indicating that this grain is undeformed outside of the indentation. The Inverse Pole Figure Map, depicts a grain with a surface normal of [0001]. The key for interpreting this can be found in Figure 2f. Intragranular defects around the indent are revealed in an EBSD disorientation map, Figure 2e. Disorientation imaging is a colour coding method that factors both the rotation axis and the angle of disorientation between each pixel in a grain and a reference orientation. The colouring algorithm reflects perceptual

colour differences that are almost proportional to the true disorientation angles between any of the orientation within the grain (Thomsen *et al.*, 2017). Clear disorientation is visible around the scratches that were observed on the sample surface before indentation. Additional disorientation is visible in the region immediately surrounding the indent. Interpretation of this map is facilitated by the key in Figure 2g. Comparison of the EBSD map after indentation and the ECC images after indentation reveals slip bands on the sample surface in the region immediately surrounding the indent, Figure 2i.

Disorientation is visible in this grain along the sides of the indent indicating deformation. Clear slip bands are visible in the ECCI image of this grain after indentation. Using the hexagon superimposed on the image, some characteristics of slip can be described. Slip appears to be consistently running parallel to the trace of $\{10\bar{1}0\}$ planes and with numerous slip bands visible. There do not appear to be any other slip bands present around the indentation and there was no further damage to the grain in other parts of the crystal. These slip bands are consistent with the observations of Rowcliffe et al., 1988 and Almond, 1983. They also found that for indentation on the basal plane, cracks develop at intersecting slip bands on $\{10\bar{1}0\}$.

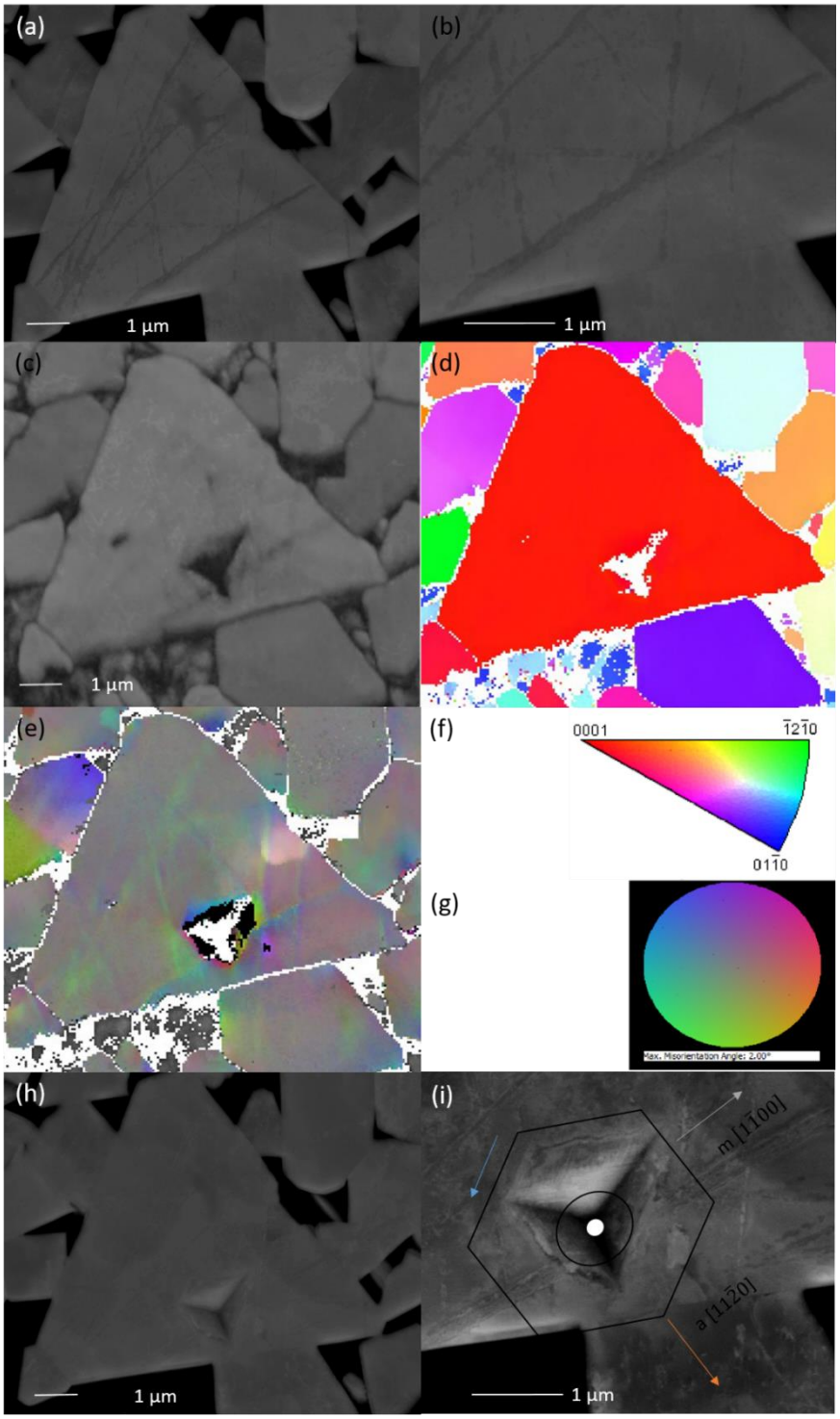

Figure 2. Indentation of the first [0001] oriented grain
(a) ECCI image before indentation
(b) region of interest before indentation
(c) Pattern quality map
(d) IPF map
(e) disorientation map (caption continues on the next page)

(f) legend for the IPF map
(g) legend for the disorientation map
(h) ECCI image after indentation
(i) region of interest after indentation with superimposed hexagon illustrating the plane normal (white dot), relevant crystallographic directions (orange and white arrows) and the direction of the induced slip bands (blue arrow).
Note that the scale is the same for all the EBSD maps.

Another grain with surface normal of [0001] was intentionally damaged with a Berkovich indenter. In Figure 3a the WC grain is visible before indentation. Note that this grain is significantly less damaged than in Figure 3. There are still noteworthy scratches on the sample surface. The region of interest where the grain was subsequently indented is expanded in Figure 3b. As with Figure 2, there are no visible dislocations on the sample surface. In Figure 3c, a pattern quality image, as generated from EBSD patterns, depicts this grain after indentation. The pattern quality appears to be uniform across the grain aside from evidence of dimpling on the sample surface due to ion milling. The Inverse Pole Figure Map depicts a grain with a surface normal of [0001]. The key for interpreting this can be found in Figure 3f. Intragranular defects around the indent are revealed in an EBSD disorientation map, Figure 3e. Clear disorientation is visible around the scratches that were observed on the sample surface before indentation. Additional disorientation is visible in the region immediately surrounding the indent. Interpretation of this map is facilitated by the key in Figure 3g. Comparison of the EBSD map after indentation and the ECC images after indentation reveals slip bands on the sample surface in the region immediately surrounding the indent, Figure 3i.

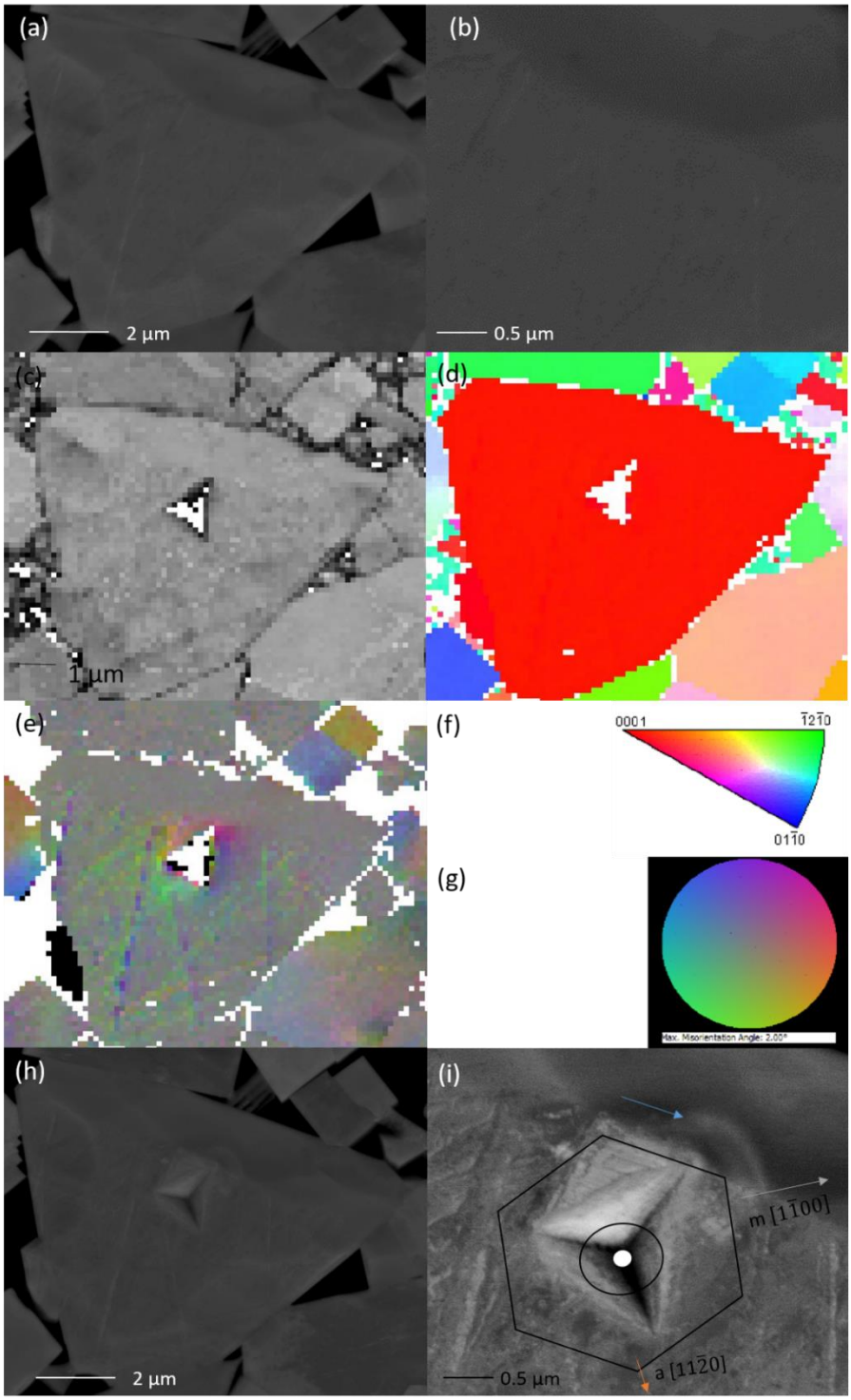

Figure 3. Indentation of the second [0001] oriented grain
(a) ECCI image before indentation
(b) region of interest before indentation
(c) Pattern quality map
(d) IPF map
(e) disorientation map (caption continues on the next page)

(f) legend for the IPF map
(g) legend for the disorientation map (h) ECCI image after indentation (i) region of interest after indentation with superimposed hexagon illustrating the plane normal (white dot), relevant crystallographic directions (orange and white arrows) and the direction of the induced slip bands (blue arrow). (Note that the scale is the same for all the EBSD maps.)

Slip bands are visible in the ECCI image of this grain after indentation. Using the hexagon superimposed on the image, some characteristics of slip can be described. As with the grain in Figure 2, slip appears to be consistently running parallel to the trace of the $\{10\bar{1}0\}$ planes with numerous slip bands visible. There do not appear to be any other slip bands present around the indentation and there was no further damage to the grain in other parts of the crystal. These slip bands are consistent with the observations above and of (Rowcliffe *et al.*, 1988; A. Almond, 1983). Note that the indentation in these grains was random. The indent was placed in different parts of the grain. In Figure 2, the indent if very close to a grain boundary, while in Figure 3 the indent is closer to the middle of the grain. It appears that grain boundaries did not play a role in the slip systems that developed after indentation. In Figure 2, the indent is located with a random orientation in the grain while in Figure 3, one tip of the indent appears to lie with its edge perpendicular to a $\{10\bar{1}0\}$ direction. Regardless of these differences, it appears that the slip bands in these two indented grains lie along the $\{11\bar{2}0\}$ direction.

5.4.1.2. $[10\bar{1}0]$

Two grains with surface normal of $[10\bar{1}0]$ were intentionally damaged with a Berkovich indenter. In Figure 4a, the WC grain is visible before indentation. The region of interest where the grain was subsequently indented is expanded in Figure 4b. Note that there are no visible dislocations on the sample surface, but there are striations on the sample surface running parallel to one of the prismatic edges. Further analysis of this grain using EBSD allows for additional insight into the crystallography of the grain. In Figure 4c, a pattern quality

image, as generated from EBSD patterns, depicts this grain after indentation. The pattern quality appears to be uniform across the grain. The Inverse Pole Figure Map depicts a grain with a surface normal of $[10\bar{1}0]$. The key for interpreting this can be found in Figure 4f. Intragranular defects around the indent are revealed in an EBSD disorientation map, Figure 4e. Clear disorientation is visible in the region immediately surrounding the indent, in particular, at the edges of the indent. Interpretation of this map is facilitated by the key in figure 4 g. Comparison of the EBSD map after indentation and the ECC images after indentation reveals slip bands on the sample surface in the region immediately surrounding the indent, Figure 4i.

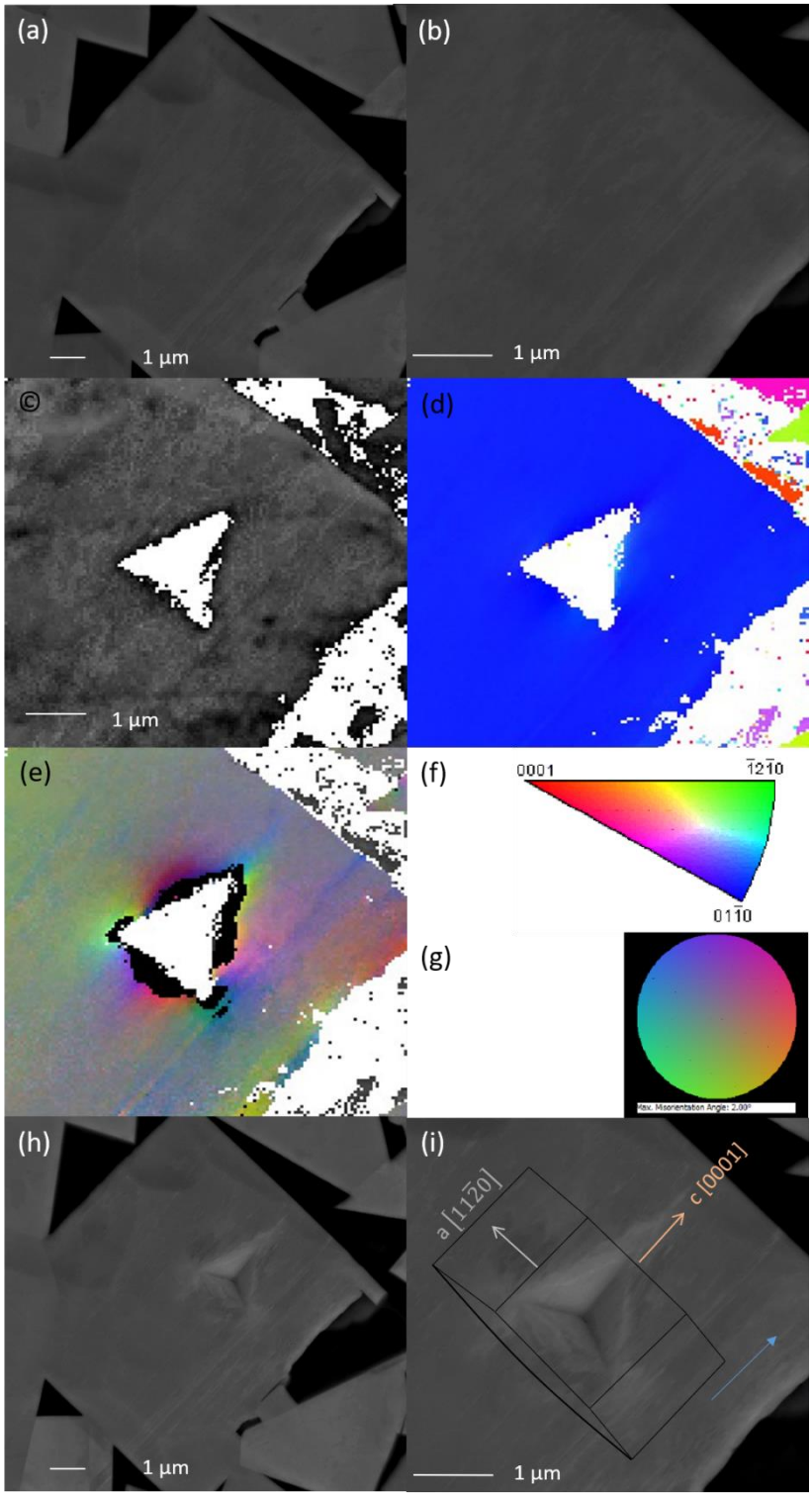

Figure 4. Indentation of the first [$10\bar{1}0$] oriented grain
(a) ECCI image before indentation
(b) region of interest before indentation
(c) Pattern quality map
(d) IPF map
(e) disorientation map (caption continues on the next page)

(f) legend for the IPF map
(g) legend for the disorientation map
(h) ECCI image after indentation
(i) region of interest after indentation with superimposed prism illustrating the relevant crystallographic directions (orange and white arrows) and the direction of the induced slip bands (blue arrow).
Note that the scale is the same for all the EBSD maps.

Disorientation is visible in this grain along the sides of the indent, as was the case in Figure 2, and along the points of the indenter, indicating deformation. Clear slip bands are visible in the ECCI image of this grain after indentation. Using the prismatic face superimposed on the image, some characteristics of slip can be described. Slip appears to run consistently along the {0001} direction with numerous slip bands visible. As opposed to the slip bands in Figures 2 and 3, the slip bands in Figure 4 seem to run through the indent and parallel to the striations on the sample surface visible before indentation. There do not appear to be any other slip bands present around the indentation and there was no further damage to the grain in other parts of the crystal. Slip bands with a direction of {0001} are consistent with the literature (Hibbs & Sinclair, 1981; Takahashi & Freise, 1965).

Another grain with surface normal of $[10\bar{1}0]$ was intentionally damaged with a Berkovich indenter. In Figure 5a the WC grain is visible before indentation. Note that this grain seems to be composed of a number of grains, with notable different surface normals, growing into the primary grain. This may affect the observations below. The region of interest where the grain was subsequently indented is expanded in Figure 5b. As with Figure 4, there are no visible dislocations on the sample surface. Further analysis of this particular grain using EBSD allows for additional insight into the crystallography of the grain. In Figure 5c, a pattern quality image, as generated from EBSD patterns, depicts this grain after indentation. The pattern quality appears to be uniform across the grain aside from evidence of dimpling on the sample surface due to ion milling. The Inverse Pole Figure Map depicts a grain with a surface normal of $[10\bar{1}0]$.

The key for interpreting this can be found in Figure 5f. Intragranular defects around the indent are revealed in an EBSD disorientation map, Figure 5e. Clear disorientation is visible around the scratches that were observed on the sample surface before indentation. Additional disorientation is visible in the region immediately surrounding the indent. Interpretation of this map is facilitated by the key in Figure 5 g. Comparison of the EBSD map after indentation and the ECC images after indentation reveals slip bands on the sample surface in the region immediately surrounding the indent, Figure 5i.

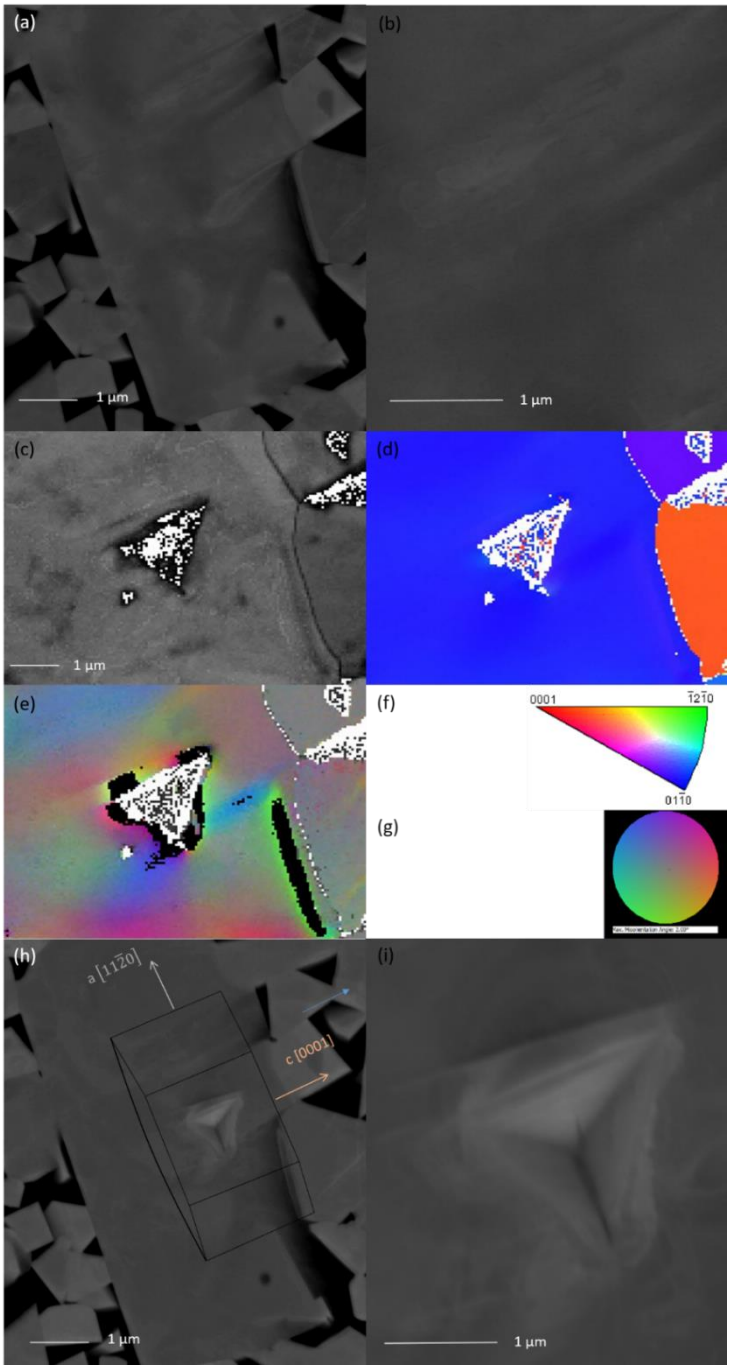

Figure 5. Indentation of the second [$10\bar{1}0$] oriented grain
(a) ECCI image before indentation
(b) region of interest before indentation
(c) Pattern quality map
(d) IPF map
(e) disorientation map
(f) legend for the IPF map
(g) legend for the disorientation map (caption continues on the next page)

(h) ECCI image after indentation
(i) region of interest after indentation with superimposed prism illustrating the plane normal, relevant crystallographic directions (orange and white arrows) and the direction of the induced slip bands (blue arrow).
Note that the scale is the same for all the EBSD maps.

Slip bands are visible in the ECCI image of this grain after indentation. Using the prismatic face superimposed on the image, it is clear that slip runs in the {0001} direction with a few slip bands visible. As with Figure 4, the slip bands in Figure 5 run through the indent. There do not appear to be any other slip bands present around the indentation and there was no further damage to the grain in other parts of the crystal. It is important to note that this grain is unusual and distinct from the previous grains discussed above in that this grain seems to contain numerous intergrowths. Figure 5d depicts the primary grain of interest here, a grain with a surface normal of $[10\bar{1}0]$ in blue and two randomly oriented grains in orange and purple. More work is necessary to determine the role that these intergrowths may play in the formation of defects in this grain. From the disorientation map, Figure 5e, there appears to be internal strain in the grain with a surface normal of $[10\bar{1}0]$ around these intergrowths. The disorientation image also reveals small changes in orientation along the slip plane, in the direction of slip. These is the most obvious evidence of changes in orientation due to slip in the four examples discussed so far.

5.4.1.3. $[11\bar{2}0]$

Two grains with surface normal of $[11\bar{2}0]$ were intentionally damaged with a Berkovich indenter. In Figure 6a, the WC grain is visible before indentation. The region of interest where the grain was subsequently indented is expanded in Figure 6b. Note that there are no visible dislocations on the sample surface, but some striations are visible. Some damage is visible from ion milling during sample preparation, specifically on the left side of the grain. Further analysis of this grain using EBSD allows for additional insight into the crystallography of the grain. In Figure 6c, a pattern quality image, as generated from EBSD

patterns, depicts this grain after indentation. The pattern quality appears to be uniform across the grain. The Inverse Pole Figure Map, depicts a grain with a surface normal of [11$\bar{2}$0]. The key for interpreting this can be found in Figure 6f. Intragranular defects around the indent are revealed in an EBSD disorientation map, Figure 6e. Disorientation is visible in the region immediately surrounding the indent. Interpretation of this map is facilitated by the key in Figure 6g. Comparison of the EBSD map after indentation and the ECC images after indentation reveals slip bands on the sample surface in the region immediately surrounding the indent, Figure 6h.

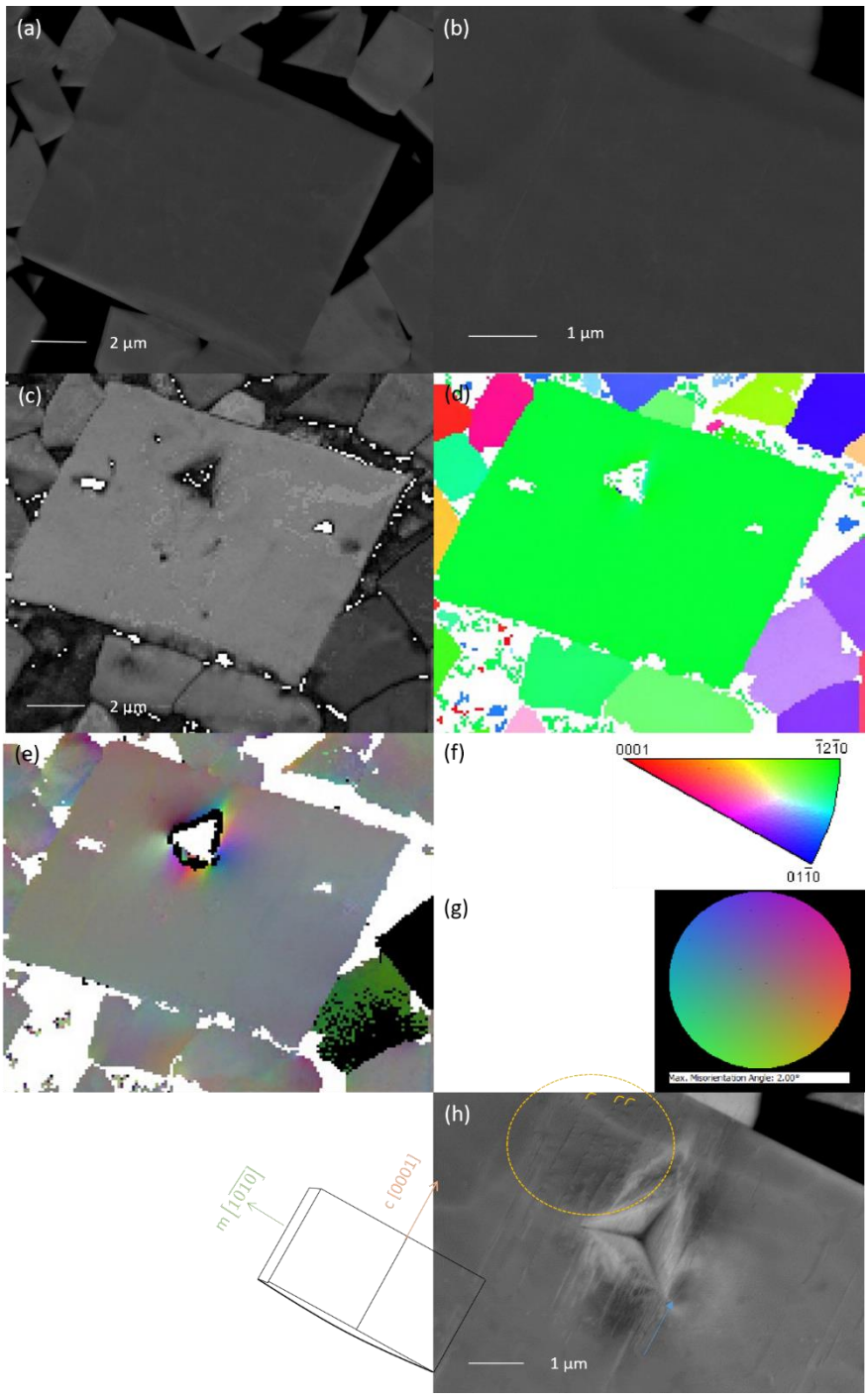

Figure 6. Indentation of the first [$11\bar{2}0$] oriented grain
(a) ECCI image before indentation
(b) region of interest before indentation
(c) Pattern quality map
(d) IPF map
(e) disorientation map
(f) legend for the IPF map
(g) legend for the disorientation map (caption continues on the next page)

(h) ECCI image after indentation. A schematic image of the secondary prismatic plane, in this case [**11$\bar{2}$0**]*, illustrating the plane normal, relevant crystallographic directions (orange and green arrows) and the direction of the induced slip bands (blue arrow). The yellow circle denotes the region with curved features. The curved yellow hooks imitate the shape of these features.*
Note that the scale is the same for all the EBSD maps.

Clear slip bands are visible in the ECCI image of this grain after indentation. Using the prismatic face superimposed on the image, some characteristics of slip can be described. Slip appears to run consistently in the {0001} direction, as was the case in the grain with a surface normal of [10$\bar{1}$0]. The slip bands in Figure 6 run on three sides of the indent. While some of the slip bands are linear lines with no other obvious characteristics, most of the slip bands to the left of the indent appear with curved features. These are highlighted in Figure 6h with a broken yellow circle. Further analysis is necessary to define them as without multiple diffraction conditions it is difficult to interpret these features.

A second grain with surface normal of [11$\bar{2}$0] was intentionally damaged with a Berkovich indenter. In Figure 7a, the WC grain is visible before indentation. The region of interest where the grain was subsequently indented is expanded in Figure 7b. Note that there are no visible dislocations on the sample surface, but some damage is visible from ion milling during sample preparation, specifically at the top of the grain. Further analysis of this particular grain using EBSD allows for additional insight into the crystallography of the grain. In Figure 7c, a pattern quality image, as generated from EBSD patterns, depicts this grain after indentation. The pattern quality map reveals some damage radiating out form the region directly surrounding the indent. The Inverse Pole Figure Map, Fig. 7d, depicts a grain with a surface normal of [11$\bar{2}$0]. The key for interpreting this can be found in Figure 7f. Intragranular defects around the indent are revealed in an EBSD disorientation map, Figure 7e. Disorientation is visible in the region immediately surrounding the indent. Interpretation of this map is facilitated by the key in Figure 7g. Comparison of the EBSD map after

indentation and the ECC images after indentation reveals slip planes on the sample surface in the region immediately surrounding the indent, Figure 7h. The region of interest around the indent, at a larger magnification is visible in Figure 7i.

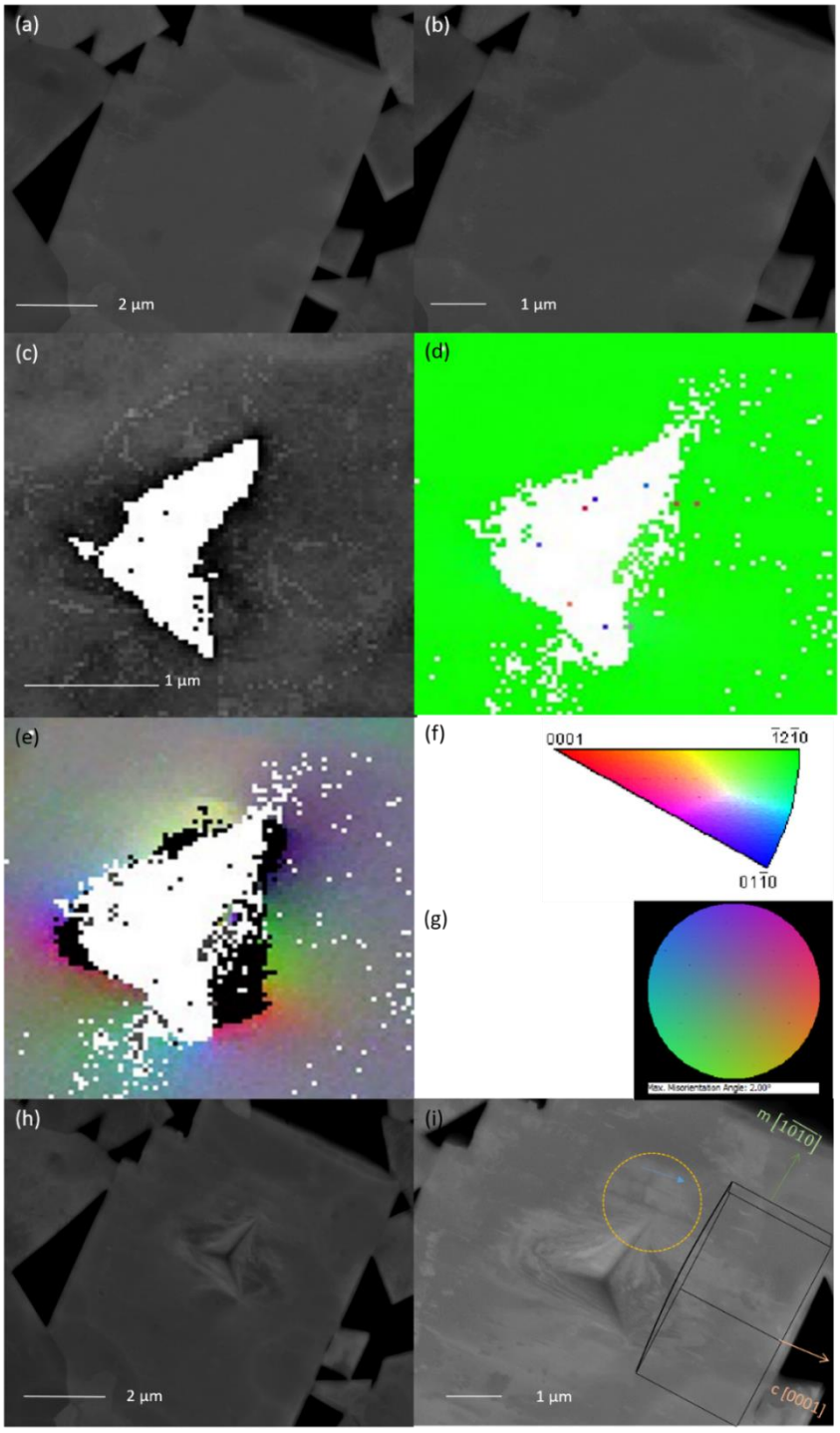

Figure 7. Indentation of a second [11$\bar{2}$0] oriented grain
(a) ECCI image before indentation
(b) region of interest before indentation
(c) Pattern quality map
(d) IPF map
(e) disorientation map (caption continues on the next page)

(f) legend for the IPF map
(g) legend for the disorientation map
(h) ECCI image after indentation.
(i) Region of interest after indentation with superimposed secondary prismatic plane, in this case [**11$\bar{2}$0**]*, illustrating the plane normal, relevant crystallographic directions (orange and green arrows) and the direction of the induced slip planes (blue arrow). The yellow circle denotes the region where two slip bands are connected by a diagonal defect.*
Note that the scale is the same for all the EBSD maps.

Slip bands are visible in the ECC image of this grain after indentation, Figure 7h. By superimposing the prismatic face on Figure 7i, some characteristics of slip can be described. Slip bands run in the {0001} direction, as was the case in the first grain with sample normal of [11$\bar{2}$0]. The slip bands in Figure 7 run all along the indent in the {0001} direction at the top, bottom and sides of the indent. All of the slip bands are linear lines with no other obvious characteristics, except for the two slip bands beneath the blue arrow. These bands seem to be connected by some kind of defect which runs in an undetermined direction. These are highlighted in Figure 6h with a broken yellow circle. Further analysis is necessary to fully define this diagonal feature. As mentioned in the discussion of Figure 6, slip bands in grains with a surface normal of [11$\bar{2}$0] have been documented in the literature where dislocations with a Burgers vector of $\boldsymbol{b} = \langle 0001 \rangle$ are formed. These have the potential for dissociation on the $\{\bar{1}2\bar{1}0\}$ prism planes into partials of the type $\langle 0001 \rangle \rightarrow {}^{1}/_{6}\langle \bar{2}023 \rangle + {}^{1}/_{6}\langle 20\bar{2}3 \rangle$ (Bolton & Redington, 1980).

5.4.2. ECCI of [0001] and [11$\bar{2}$0] oriented grains using a spherical indenter

Collaborative research was undertaken at NPL on nanoindentation from ambient to high temperature using a spherical indenter in grains with surface normals [0001], [1$\bar{1}$00] and [11$\bar{2}$0]. Experimental data was acquired by Dr. Francois de Luca. A spherical nanoindenter was used in this study as spherical indenters leave more homogenous deformation in all directions rather than

preferentially along the indenter edges or indenter tip. More details on this indenter can be found in Chapter 2. After indentation ECCI data was acquired of the indented region, followed by focused ion beam (FIB) sectioning to acquire a cross-section of the indented region. By tilting the grain after sectioning so that the cross-section was perpendicular to the electron beam, three-dimensional distribution of slip around the indents can be seen.

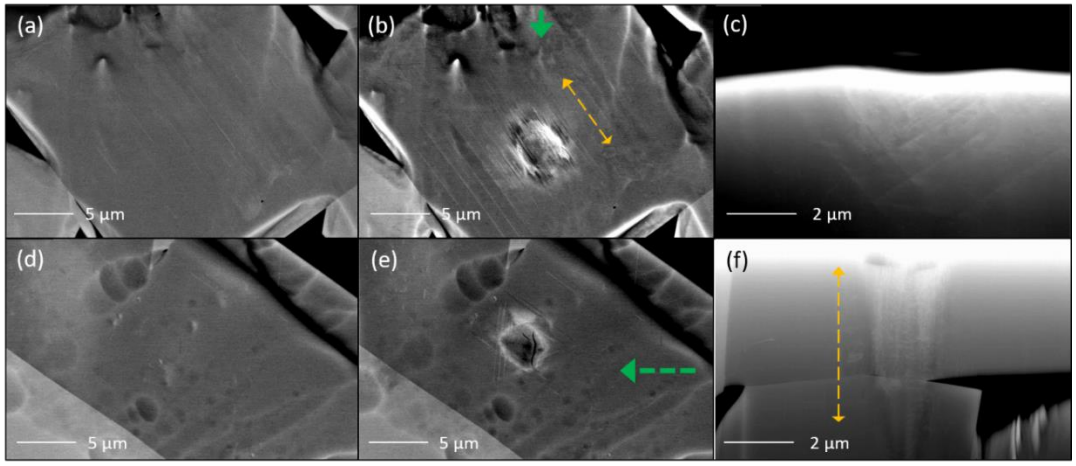

Figure 8. Indentation of WC followed by ECCI analysis and FIB milling
(a) ECCI of a [**11$\bar{2}$0**] *oriented grain before indentation*
(b) the same grain found in Fig. 8(a) after indentation with slip bands running parallel to two grain edges and perpendicular to the remaining two edges
(c) cross section of the grain in Figs. 8(a) and (b)
(d) ECCI of a [**0001**] *oriented grain before indentation*
(e) the same grain found in Fig. 8(d) after indentation with slip bands running parallel to two grain edges and perpendicular to the remaining two edges
(f) cross section of the grain in Figs. 8(d) and €. The yellow arrows indicate diffusion of deformation through the grain while the green arrows indicate milling direction.

These three ECC images, the first acquired before indentation, the second acquired after indentation at ambient temperature and the third acquired after indentation perpendicular to the indent, show slip planes around the indent which were not present in the as-sintered material. The slip in the [11$\bar{2}$0] oriented grain, Figure 8a-c, show slip lines parallel to the [10$\bar{1}$0] direction, in agreement with previous work (Luyckx, 1970). Notable in Figure 8c is the intercepting slip lines which is consistent with previous slip on prismatic planes (Rowcliffe *et al.*, 1988; Luyckx, 1970).

Slip lines intercepting each other at 60° are visible on the [0001] oriented grain, Figure 8d-f. ECC images of the region perpendicular to the indent reveal that damage is limited to the region immediately beneath the indent and not in the surrounding area.

This study continues on to investigate WC grains heated to 700° C and then indented. Grains were indented at increasing temperatures to measure the change in hardness from ambient to high temperature. Basal and prismatic grins softened as temperature increased, with a 70% reduction in hardness measured at 700° C. Increasing temperature leads to more damage in the region surrounding the indent. This data is not shown here. The deformation data in this study indicates a preference for slip on the prismatic plane in indented WC grains. In the ambient temperature work in Figures 1-7, slip bands were apparent on the basal, primary prismatic and secondary prismatic planes.

5.5. Summary

In this chapter, slip bands and crystallographic defects are observed in grains with surface normals of [0001], $[1\bar{1}00]$ and $[11\bar{2}0]$ in ECCI data after indentation. When grains with surface normal [0001] are indented with a Berkovich tip, slip bands parallel to the $\{10\bar{1}0\}$ directions are apparent which is consistent with the observations of (Rowcliffe *et al.*, 1988; A. Almond, 1983). Proximity to grain boundaries and orientation of the indenter do not seem to play a role in the slip systems that develop after indentation.

In grains with surface normal of $[1\bar{1}00]$, slip bands run in the {0001}. Slip bands with a direction of {0001} are consistent with the literature (Takahashi & Freise, 1965; Hibbs & Sinclair, 1981). The disorientation images from the EBSD data set reveal small changes in orientation along the slip plane, in the direction of slip.

In grains with surface normal of $[11\bar{2}0]$ slip bands appear to run in the {0001} direction, as was the case in the grain with a surface normal of $[10\bar{1}0]$. The slip bands are linear lines and are accompanied by features with curved tails. Straight dislocation segments can form extinction fringes and streaking of the diffraction pattern. These could be extended dislocations or stacking faults, which could indicate an antiphase boundary (Bolton & Redington, 1980). Slip bands in grains with a surface normal of $[11\bar{2}0]$ have been documented in the literature with a Burgers vector of $\mathbf{b} = \langle 0001 \rangle$. These have the potential for dissociation on the $\{\bar{1}2\bar{1}0\}$ prism planes into partials of the type $\langle 0001 \rangle \rightarrow {}^{1}/_{6}\langle \bar{2}023 \rangle + {}^{1}/_{6}\langle 20\bar{2}3 \rangle$ (Bolton & Redington, 1980).

The $[11\bar{2}0]$ oriented grain indented with a spherical indenter exhibits slip lines parallel to the $[10\bar{1}0]$ direction, in agreement with previous work (Luyckx, 1970). Slip lines intercepting each other at 60° are visible on the [0001] oriented grain.

This study is the first to systematically study indents in WC grains with surface normals [0001], $[1\bar{1}00]$ and $[11\bar{2}0]$. The ECCI work here agrees with previous TEM data on slip systems in indented WC grains. Using ECCI presents an advantage over TEM in that damage in grains can be imaged over a wider field of view with simpler sample preparation.

6. Crystallographic defects in twinned, gem-quality diamonds

6.1. Introduction

This chapter investigates twinning in naturally occurring gem-quality diamonds. Combining cathodoluminescence (CL) imaging and electron backscatter diffraction (EBSD) helps to locate the twinning plane, visualize zoning in the diamond's growth and discern the differences in orientation between the two grains, discussed below as 'sibling twins'.

Twinning occurs in nature when a new crystal is added to the face of an existing crystal. The new crystal shares lattice points on the face of the original crystal, but the twinned domain is crystallographically rotated from the parent due to errors in the normal stacking of the carbon atoms along the ⟨111⟩ family of crystal directions (Butler & Oleynik, 2008; Nelson, 2013). Diamond contact twins are called macles and follow the spinel law which describes a twin plane parallel to an octahedron (Nelson, 2013). Twinning in synthetically grown diamonds is commonly observed and generally has a positive impact on mechanical characteristics of diamond and a negative effect on optical and electronic properties (Butler & Oleynik, 2008). In gem-quality diamonds the twinning plane traps microinclusions and mineral inclusions (Jablon & Navon, 2016).

To investigate the growth of macles, panchromatic cathodoluminescence images were acquired. These reveal borders between zones of discrete growth. EBSD maps were then acquired of the entire polished diamonds. Inverse pole figure and Euler maps reveal the twinning plane, and the misorientation between the two siblings with [101] oriented exposed faces. Disorientation maps reveal zoning in the diamond's growth, similar to the zoning visible in CL. Background information on these techniques can be found in Chapter 2.

6.2. Sample specifications and experimental details

6.2.1. Choosing samples

The macles in this study were chosen based on several factors. These samples were originally analysed in a systematic search for fluid microinclusions (Jablon & Navon, 2016). In that study the assumption was made that the probability of finding inclusions was higher near imperfections in the crystal, near mineral inclusions, along the twinning plane or along borders between zones with discrete cathodoluminescence intensities. In the 2016 study, 50 diamonds from the Venetia diamond mine and 50 diamonds from the Voorspoed diamond mine, both in South Africa, were examined. All the macles weigh between six and 15 mg and are between 0.6 and 1.6 mm thick. Macles grow fastest along the twinning plane leading to the development of two triangular faces with similar orientation. The resulting diamond is flat and triangular, as seen in Figure 1a with the twinning surface parallel to the large (111) faces. The remaining octahedral faces are small, Figure 1b. The twinning plane bisects the diamond, as seen in a diamond turned on its side in Figure 1c. The red line traces the twinning plane. The raw diamonds in this study are depicted in Figure 2.

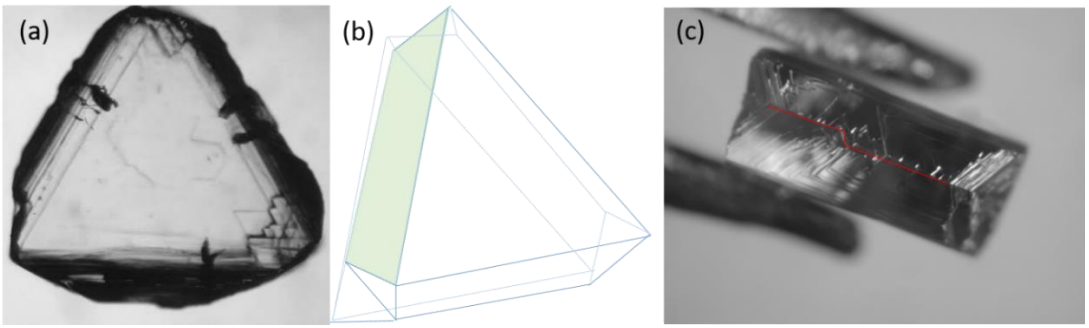

Figure 1. A twinned diamond's crystallographic faces
(a) Optical micrograph of the dominant, triangular face of a macle
(b) Schematic drawing of a macle with one of the smaller remaining octahedral faces in green.
(c) A raw macle turned to its side. The twinning plane, in red, separates the two large triangular faces. Note that the twinning plane is not linear.

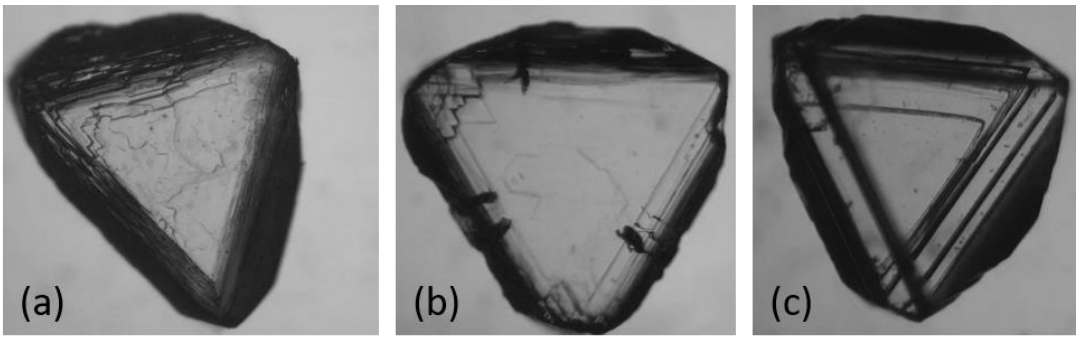

Figure 2. Optical micrographs of the diamonds in this study
(a) diamond 617 from the Voorspoed mine, SA
(b) diamond 625 from the Voorspoed mine, SA
(c) diamond 596 from the Venetia mine, SA. These images were taken before cutting and polishing. In all three images, the large, dominant octahedral face is visible.

6.2.2. Sample preparation

The macles were polished using a diamond wheel perpendicular to the large triangular faces, exposing the twinning plane. These wheels are embedded with microscopic diamond bits. They were cleaned for two hours in 69% HNO_3 and 60% HF in an ultrasonic bath, rinsed in water, then rinsed in alcohol and carbon-coated to facilitate imaging in an electron microscope. The carbon coat is approximately 5 nm thick as determined by interference measurement on a

gold sample. Carbon coating is necessary because diamonds are not conductive. Without a carbon coating, charging would be apparent on the sample surface and imaging in an SEM or EPMA would be difficult.

6.2.3. Acquiring images: ECCI, CL, EBSD

A JEOL JXA-8230 Electron Probe Microanalyzer at the Hebrew University of Jerusalem, was used for initial SE, CL and ECC imaging. Using the EPMA's backscatter detector at 0° tilt, electron channelling contrast images were collected, Figure 3. ECC images (ECCI) reveal the two twins. As the twins do not have the same orientation, ECCI can reveal both the twinning plane and the distinct twins with varying levels of contrast. Subsequently the JXA-8530F field emission EPMA at the University of Strathclyde was used to collect panchromatic CL images at 15kV at various beam currents. These maps reveal the diamond growth patterns and the location of the twinning plane. In these data sets it is apparent that the twinning plane is not linear but notched throughout the diamonds. The non-linear nature of the twinning plane has not been reported extensively in the literature. This sparked an interest in the crystallization mechanism and served as an impetus for EBSD analysis. EBSD maps were acquired at the University of Strathclyde using an Oxford NordlysNano system mounted on an FEI Quanta Field Emission Gun Scanning Electron Microscope (FEG SEM). Further information on the hardware configuration can be found in chapter 2.

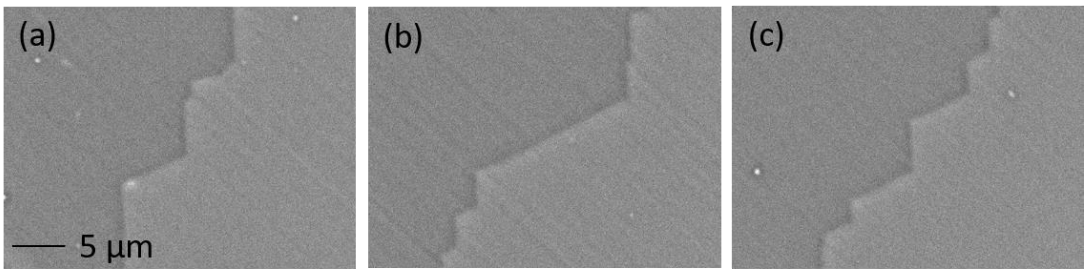

Figure 3. ECCI of the twinning plane
(a-c) Electron channelling contrast images of a macle, with the two sibling twins on either side of the jagged twin plane.

6.3. Twinning

6.3.1. The crystallography of twinning

As discussed in chapter 2, twinning is a crystallographic defect. Growth twins are naturally occurring crystallographic anomalies and form when a crystal is added to an existing crystal face (Nelson, 2013). Their relationship always adds symmetry to the crystal which can be characterized by symmetry operations, such as reflection, rotation or inversion. There are two primary growth twins, contact and penetration twins. The former have a plane separating the two crystals and can be defined by a twin law, Figure 4a. The latter are separated by an irregular surface and can be described by a twin center or axis, Figure 4b. The two twinned growth crystals, discussed below as sibling grains, always share lattice points with each other, Figure 4c. The jagged twinning plane in Figure 3 does not visually appear to satisfy the conditions for a contact or penetration twin, prompting additional investigation.

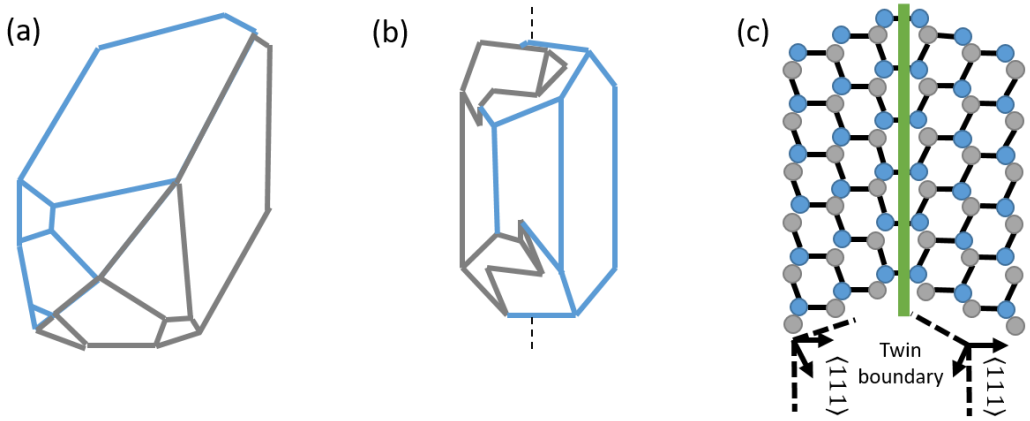

Figure 4. The crystallography of twinning
(a) contact twin
(b) penetration twin
(c) the twinning plane in a contact twin
Image adapted from, https://www.tulane.edu/~sanelson/eens211/twinning.htm

6.3.2. Twinning in natural diamonds; contact twins

Diamonds only twin during growth by lattice merohedry, where the lattice of the sibling twins exist as multiple lattices continuing from one component to the next (Yacoot *et al.*, 1998). Previous work demonstrated that macles are in fact contact twins, although there is often intergrowth between the siblings. Twinning in macles occurs from the onset of diamond nucleation, often from a nucleus (Machado *et al.*, 1998).

According to the theory proposed by Butler & Oleynik, 2008, twinning in synthetic diamonds originates from the formation of a hydrogen-terminated four carbon atom cluster on a {111} surface morphology. This cluster is the point of crystallization for the subsequent growth layer. This model describes the crystallization of contact twins and the observation of defects on the {111} growth sectors. The two crystals in a macle represent domains that are crystallographically rotated from the parent crystal by errors in the normal carbon stacking mechanism along the [111] crystal direction, Figure 5. Twinning in diamonds is defined as contact twinning when the growth appears on the {111} surface (Everson *et al.*, 1994; Tamor & Everson, 1994; Wild *et al.*, 1990).

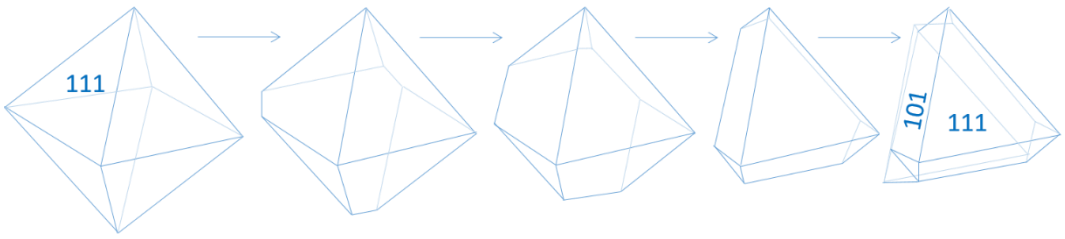

Figure 5. The notional relationship between an octahedron and a spinel twin producing a triangular type crystal face.
In a typical octahedron (left) one face is distorted leading to a flattened form with a triangular face, ultimately resulting in a triangular twinned crystal. This is "notional" in that this is not how the spinel twin evolves with time, but rather, a visual guide to compare an octahedron (left) and triangular face (right).

6.4. Results and Discussion

There are two primary challenges when using EBSD on non-conductive samples, like diamonds. When acquiring EBSD, the sample must be well polished with little deformation for optimal pattern acquisition. This is particularly difficult in the earth sciences where rock samples, consisting of different minerals, with different hardnesses, must be polished to similar heights and similar finishes. When polishing rocks or minerals for EBSD analysis, the sample is generally polished with a hard cloth with a coarse abrasive, slowly moving on to softer cloths with finer abrasives. Excessive polishing can result in inadvertent damage to the sample surface, for example, excessive relief.

Minerals and rocks are generally non-conductive materials which leads to charging in scanning electron microscopes. Charging is the build-up of energy on the sample surface which isn't dissipated throughout the sample through conductivity (Shaffner & Van Veld, 1971). Several steps can be taken to minimize charging in non-conducting materials. Samples are polished to minimize surface topography. The electron beam should be turned on only once the sample has been tilted to 70° and only during the analysis. When working in an environmental SEM, the sample can be analysed in variable pressure mode. Charge can be dissipated through the sample by building a conductive path between the sample and the sample holder with conductive tape or conductive paint around the sample and down to the holder. Working at high speed or low probe current and accelerating voltage can also eliminate charge build up on the sample surface. These attempts to eliminate charging may not work on every sample and the sample may need to be coated with a conductive coat. This poses a significant challenge to EBSD users as any coat on the sample surface will increase the signal to noise ratio leading to poor electron backscatter patterns. Poor EBSPs cannot be easily identified by the software. This leads to poor indexing and misleading EBSD maps. When coating is necessary, carbon should be applied and not exceed 2-5 nm in thickness (Bestmann *et al.*, 2011; Trimby &

Prior, 1999). Thinner coats may not fully eliminate charging from the sample surface.

In this study, CL was acquired in three diamonds, followed by EBSD. The CL maps reveal zoning and the twinning plane as seen in Figure 6a. Note the green dotted line around an initial seed in the CL map. EBSD maps also reveal the twinning plane along with rotation between the original crystal and the twin. An EBSD band contrast map reflects the quality of the electron backscatter patterns (EBSPs) during acquisition. In diamond 617 from the Voorspoed mine in South Africa, the sibling twins are distinctly visible and separated by the twinning plane. One of the twins, the right side, has lower quality patterns which appear slightly darker in Figure 6b. The twinning plane is traced in red. Inverse pole figure maps (IPF Z), which depict crystallographic orientation in terms of the sample coordinate system, reveal that both twins are [101], Figure 6c. Using the IPF Z key, located below Figure 6c, no variation in orientation between the twins is apparent. Disorientation maps describe subgrain differences in orientation (Thomsen *et al.*, 2017) and here they reveal zoning similar to that seen in CL maps as outlined by the black dotted line, Figure 6d. The Euler map reveals subtle rotation as depicted in Figure 6e, where the pink and blue colours reflect a 173° rotation in the first Euler angle component. Much more subtle rotations are revealed by the second and third Euler angle components.

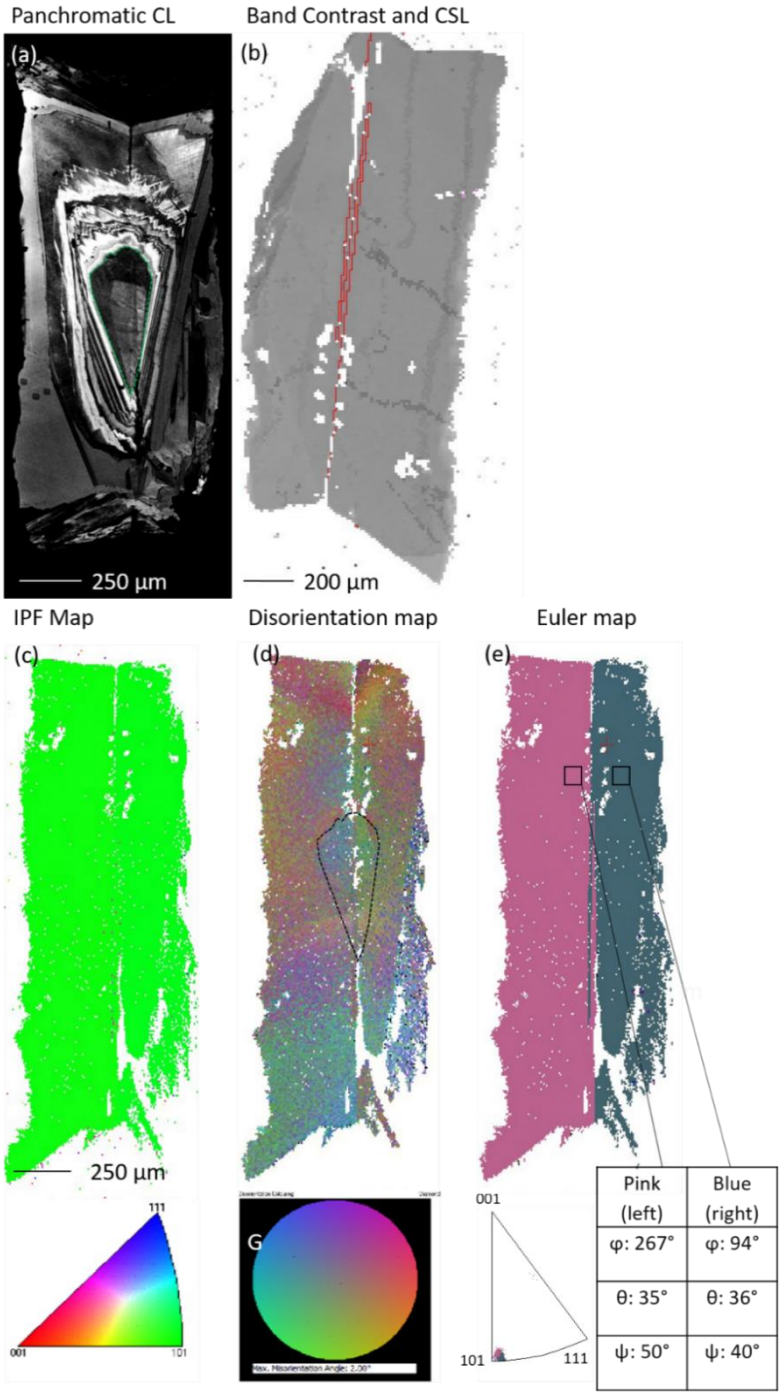

Figure 6. EBSD and CL data from diamond 617
(a) Panchromatic CL map
(b) band contrast map with CSL twin boundary in red
(c) IPF Z map and colour key
(d) disorientation map and key
(e) Euler angle map, Euler angle key and chart of Euler angles for the two siblings.
Note the scale for figures 6(c-e) is the same.

In diamond 596 from the Venetia mine in South Africa, the cathodoluminescence map, Figure 7a reveals an initial seed from which the diamond grew and then mostly concentric regions of growth. Note the uneven growth in the upper right and lower right hand corners of the CL map. The band contrast image reveals a twisted twinning plane, traced in Figure 7b in red, and that one of the twins (the left side) has lower quality patterns. The inverse pole figure map (IPF Z) reveals that both twins are [101] faces, Figure 7c, with no apparent variation in crystallographic orientation. Disorientation maps reveal differences in sub-grain orientation that are subtly reflective of zoning in the CL map, Figure 7d. The non-linear twinning plane is traced in black. The Euler map reveals small rotations in orientation as depicted in Figure 7e. Based on the table of Euler angles in Figure 7e, the blue and pink colours reflect a 174° rotation in the first Euler angle component. This is nearly the same rotation in the first Euler angle component as seen in Figure 6e. More subtle rotations are revealed by the second and third Euler angle components. However, these rotations are more pronounced than those in Figure 6e.

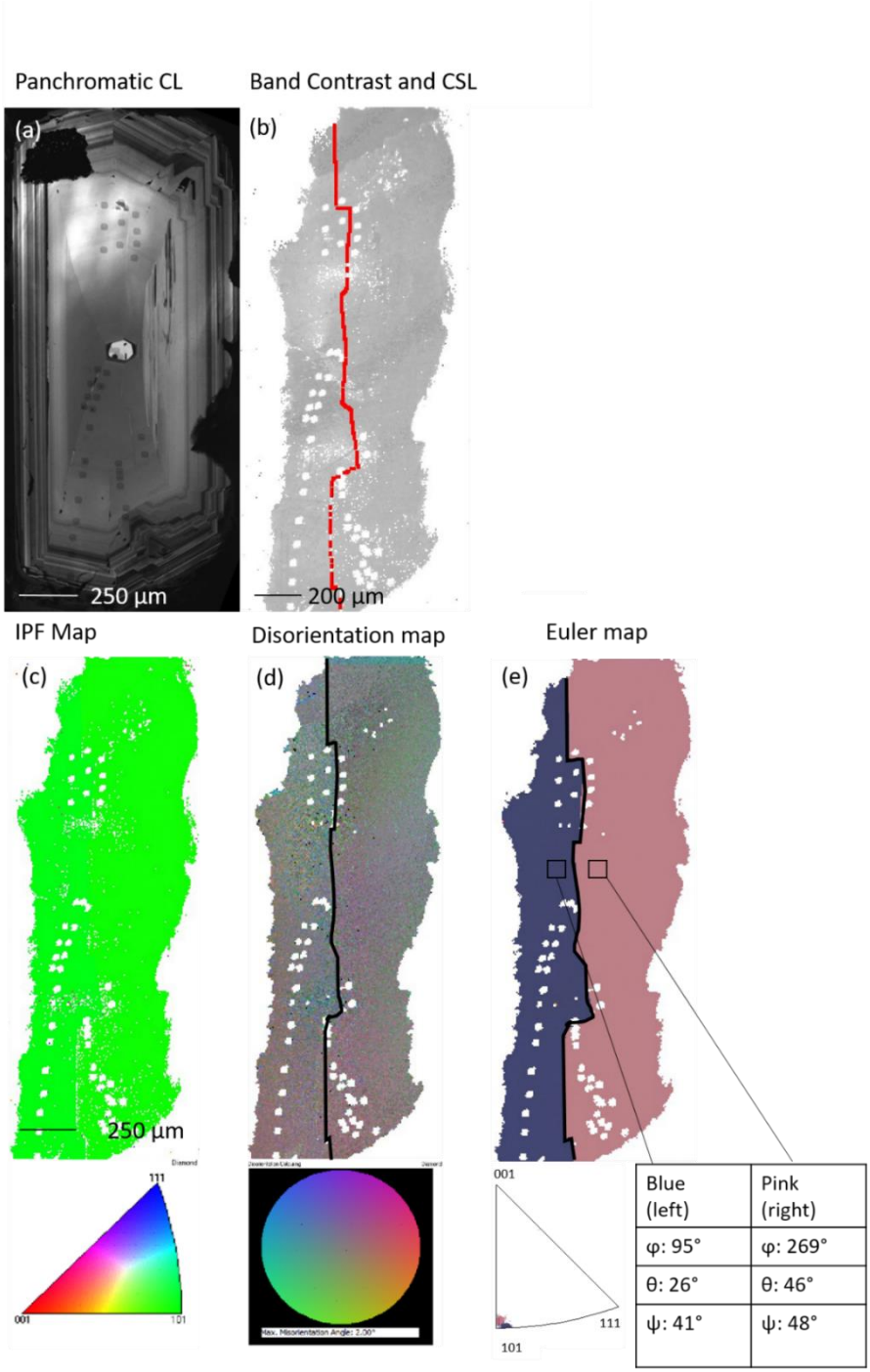

Figure 7. EBSD and CL data from diamond 596
(a) Panchromatic CL map
(b) band contrast map with CSL twin boundary in red
(c) IPF Z map and colour key
(d) disorientation map and key
(e) Euler angle map, Euler angle key and chart of Euler angles for the two siblings.
Note the scale for figures 7(c-e) is the same.

In diamond 625 from the Voorspoed mine in South Africa, the CL map reveals an initial seed from which the diamond grew, another seed surrounding the first seed with concentric growth, followed by more even growth bands, outlined in blue, Figure 8a. In the bottom right of the CL map, dissolution and regrowth of the diamond is apparent in the non-linearity of the growth bands. The twinning plane is traced here in black. The band contrast image reveals a twinning plane with kinks like that seen in diamond 617, Figure 6. Here one of the twins, the right side, has lower quality patterns, Figure 8b. The inverse pole figure map (IPF-Z) reveals that both twins are close to the [101] faces, with no obvious variation in orientation between the twins. Noticeable in this data set is the poor indexing on the bottom left of the diamond. This is due to polishing facets which are visible in the band contrast image, Figure 8c. A disorientation map reveals subtle changes in sub-grain orientation which reflect some zoning in the CL map. Smaller step sizes and a more detailed analysis of the data is required to fully quantify the similarities, Figure 8d. The Euler map reveals subtle rotation as depicted in Figure 8e, where the pink and blue colours reflect a 182° rotation in the first Euler angle component. The absolute value difference between the Euler angle components is listed in Table 1. Much more subtle rotations are revealed by the second and third Euler angle components. This rotation is quite similar to that found in the two other diamonds discussed above.

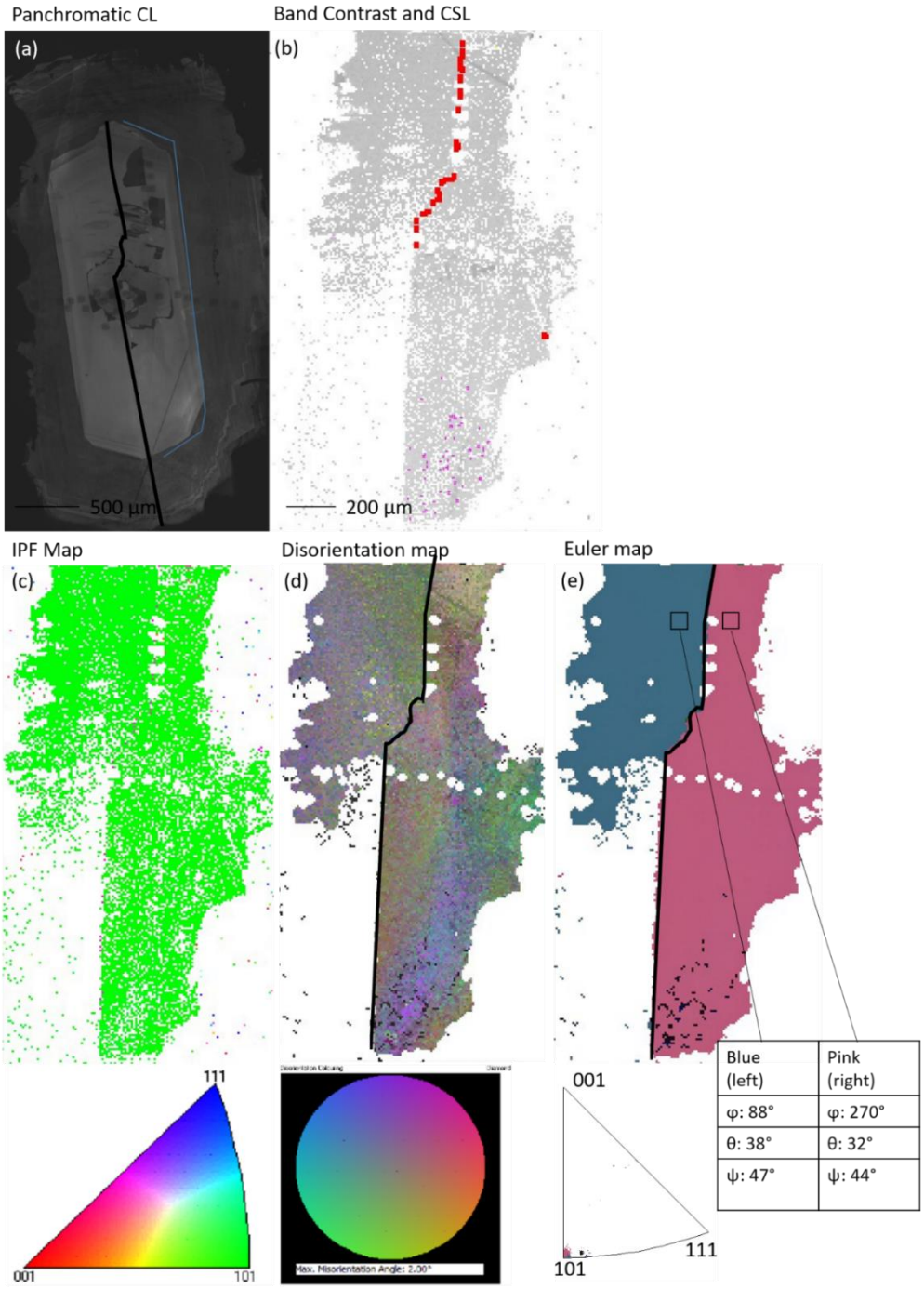

Figure 8. EBSD and CL data from diamond 625
(a) Panchromatic CL map
(b) Band contrast map with CSL twin boundary in red
(c) IPF Z map and colour key
(d) disorientation map and key
(e) Euler angle map, Euler angle key and chart of Euler angles for the two siblings.
Note the scale for figures 8(b-e) is the same.

Preliminary CL hyperspectral data was collected for all three diamonds but is not discussed here. An example spectrum from each diamond is found below in Figure 9.

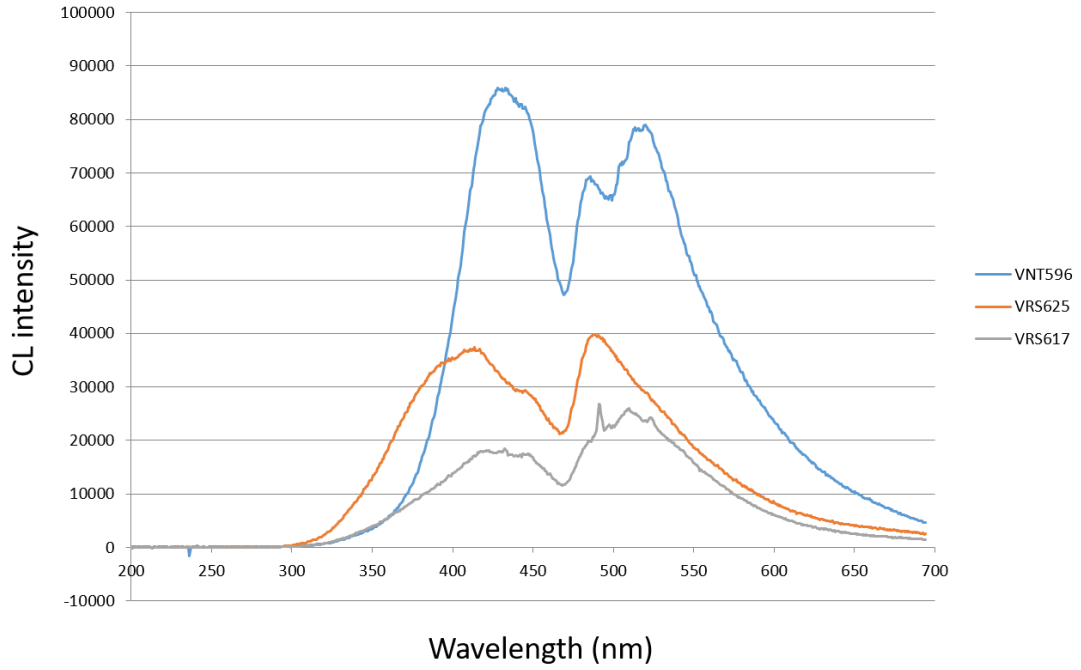

Figure 9. CL spectra from diamonds 596, 625 and 617

All three diamonds in this study are separated by a twinning plane with a $\Sigma = 3$ coincident site lattice (CSL) twin boundary. CSLs were introduced and discussed in chapter 2. In this work, the CSL information is important as it reinforces the work of Machado and emphasizes that this is a twinning boundary and that macles are not composed of two separate diamonds joined after the completion of crystallization. Even with the apparent presence of penetration growth in diamond 617, the CSL boundary remains consistent throughout the sample.

In the three diamonds presented here, the absolute value of the rotation between siblings is close to 180°, as seen in Table 1. The variation between diamond samples is not surprising as the growth patterns exposed by the cathodoluminescence images reveals different growth in different diamonds. Yacoot and Moore in 1998 concluded that twinning in macles is by 180° rotation

about a [111] direction, equivalent to twinning by reflection in a (111) plane. The work presented in this chapter corroborates their conclusion.

Table 1. Absolute value of Euler angles between the two twins

	617	**596**	**625**
φ:	173	174	182
θ:	1	20	6
ψ:	10	7	3

In addition to providing information on the rotation between sibling grains, EBSD reveals zoning in the diamonds. The zoned diamond growth, as seen in disorientation maps, corresponds to cathodoluminescence images. More in depth EBSD work is needed, similar to the work in chapter 3, to fully understand the relationship between disorientation in these diamonds and diamond growth.

Butler and Oleynik cite trace amounts of nitrogen in the plasma assisted growth of synthetic diamonds as the reason for the formation of macrosteps on the surface of diamonds and the transition from growth rates on {111} to {100} surfaces. The environments surrounding natural diamonds is less controlled than that of synthetic diamonds, however nitrogen is present in the environment when diamonds crystallize. Nitrogen in diamonds is well documented and diamonds ON-VNT-596 and ON-VRS-625 have 66 and 392 ppm nitrogen respectively, as determined by FTIR. According to the theory presented by Butler and Oleynik for synthetic diamonds, one sibling twin has [111] orientation and the other sibling twin is slightly rotated. This is observed in all three of the naturally-occurring diamonds in this study. Butler and Oleynik propose that the two twins grow in tandem with one twin acting as the parent, and the daughter twin which is crystallographically rotated from the parent crystal by errors in the normal carbon stacking mechanism along the [111] crystal direction. These errors on the [111] plane are predicted

theoretically by Butler and Oleynik to rotate the twin from the parent 70.58° about the [110] axis. This however, is not what is revealed by the Euler maps in Figures 6, 7 and 8, for the macles in this study.

Previous X-Ray topography work on naturally occurring macles by Machado in 1984 and Yacoot and Moore in 1998 definitively ruled out the possibility that naturally-occurring contact twins are made of two entirely separate entities separated by a plane as penetration between siblings is almost always observed. In this work, it is clear from ECCI, CL images and EBSD (specifically Euler angle maps and CSL twin boundary maps) that these are twinned diamonds with some intergrowth between the two twins. The twinning plane is jagged throughout the three diamonds in this study, demonstrating some intergrowths. This agrees with the observations of Yacoot and Moore who also observed twinning planes that are not linear. As described in section 6.3.1, contact twins have a plane separating the two twinned crystals and interpretant twins have an irregular surface.

6.5. Summary

This work presents cathodoluminescence and electron backscattered diffraction data documenting the crystallographic orientation of twinned gem-quality diamonds. The twinned diamonds are all composed of two sibling twins with around 180° rotation in Euler angles between the siblings. CL is helpful in understanding the initial twin nucleation and distinct periods of crystallization in the diamond's history while EBSD can be used in some cases to corroborate CL data like in diamond 617 where zoning is visible in both techniques. CL and EBSD together are powerful tools for characterizing the twinning plane and growth mechanism in diamonds.

7. Conclusions

7.1. Techniques and materials

This thesis presents work on the analysis of hexagonal tungsten carbide (WC) grains and cubic diamonds using the SEM based backscattered electron techniques of ECCI and EBSD and panchromatic cathodoluminescence imaging. Chapter 2 introduced the materials in this work and the analytical techniques used in this thesis. Chapters 3 and 4 discussed WC grains and the dislocations and subgrains inherent in them after sintering using ECCI for the first time to identify dislocations. Next, chapter 5 discussed WC grains that were indented to study the associated defects. Using ECCI and EBSD in WC demonstrates a novel use of these techniques to study crystallographic defects in hardmetals. New information on dislocations and subgrains was found allowing for greater insight into their deformation. The final chapter examined twinned gem-quality diamonds, known in the diamond trade as macles. Combining EBSD, ECCI and CL analysis allowed for investigation into the twinning plane, interpretation of the diamond's nucleation and zoned growth. This represents the first time that these techniques have been used together on gem-quality diamonds. Chapter 6 presents advances in understanding the crystallography of macles.

7.2. Tungsten carbide grains

7.2.1. Conclusions on tungsten carbide

In chapter 3 of this thesis the dislocations and subgrain structures of WC grains of known crystallographic orientation were analysed. This was the first time that ECCI analysis was used to study WC grains (Jablon *et al.*, 2019). By combining ECCI and EBSD, new insights into the microstructure of WC grains were revealed. The advantage of using these techniques over the more common TEM

based techniques is that ECCI and EBSD allow for analysis over a large field of view, in this case 75 μm × 75 μm. These larger scale analyses reveal dislocations throughout an entire WC grain, showing, for the first time, the microstructure and misorientation of whole grains. ECCI exposed dislocations while EBSD data revealed small changes in crystallographic orientation resulting from dislocations and subgrains, thereby corroborating the ECCI data. This chapter demonstrates that used together, these two techniques are an effective tool for acquiring information on defects inherent in undeformed WC grains after sintering. In the two samples analysed in this chapter clear subgrains, with misorientation on the order of 0.2°, and distinct boundaries are discussed. One previous observation has been reported of subgrains present within WC grains in a WC based hardmetal where TEM was used to observe one grain enclosing three smaller grains and a second grain partly enclosing a smaller grain at a WC-Co boundary (Delanoë *et al.*, 2007). However, misorientation in these cases were ≈ 2°, or 3 times larger than the maximum observed here or were actually CSL boundaries. These grains were absorbed by abnormal grain growth, leading to abnormally large grains, whereas the observations here are of grains well within the normal grain size distribution. Previous work investigated WC grain shape and size in relationship to the starting powders, however none report on the sub structure or show any evidence for growth from a nucleating grain (e.g. Lay et al. 2008; Pellan et al. 2015; Wang, Fang, and Sohn 2008; Zhong et al. 2011; Kim et al. 2003). This chapter presents evidence detailing WC subgrains and the dislocations on their boundaries using ECCI data and EBSD together. An advantage of using EBSD and ECCI together is that EBSD can provide quantitative information on misorientation, such as the magnitude and direction of the misorientation. EBSD typically provides an orientation precision on the order of 0.1°-0.5°. In the work reported here, the experimental patterns were compared to dynamical simulations, improving the orientation resolution to 0.3° (Winkelmann *et al.*, 2020). This measurable advantage marks a significant turning point in the type of features identifiable using EBSD. One

example of this is the visibility of dislocations in the EBSD data after pattern matching which provides a spatial resolution of approximately 100 nm.

Chapter 4 expands on the work in chapter 3 by categorizing the type of dislocations found in grains of known crystallographic orientation using ECCI and EBSD. Dislocations and their Burgers vectors are described. This new approach to categorizing dislocations in the basal and prismatic planes will help explain how WC grains deform plastically. This chapter also covers the role that grain boundaries play in the formation of dislocations during sintering. The crystallography of WC is discussed in detail here and the reasons why the primary prismatic plane is the slip plane in WC, an anomaly among hexagonal materials. After identifying grains with the $[0001]$, $[1\bar{1}00]$ and $[11\bar{2}0]$ axes normal to the sample, ECCI rotation series were acquired for each crystallographic orientation. For the [0001] oriented grain, most of the dislocations observed were propagating at, or around 90°, to the surface of the grain. The $\boldsymbol{g} \cdot \boldsymbol{b}$ analysis, for different diffraction conditions allows for the identification of dislocations with Burgers vectors of $^1/_3\langle 11\bar{2}0\rangle$ or $^1/_3\langle 11\bar{2}3\rangle$. This was corroborated by investigating the direction of the black-white (B-W) contrast exhibited by the dislocations. Most of the dislocations in this grain are mixed dislocations as the B-W contrast exhibited by the dislocations rotates by an angle other than 180° in different diffraction conditions. Some edge dislocations were identified whose B-W contrast appears to reverse on comparing the two ECCI images. Analysis of their B-W contrast direction implies $\boldsymbol{b} = {}^1/_3\,[\bar{1}2\bar{1}0]$ or $^1/_3\,[1\bar{2}10]$. This grain contained a subgrain which was surrounded by dislocations. While some dislocations are configured in a line, nearly all the dislocations appear as individual defects terminating on the grain's surface. The majority of dislocations in this grain align along either the $\{\bar{1}2\bar{1}0\}$ or $\{11\bar{2}0\}$ directions.

For the $[1\bar{1}00]$ oriented grain three types of dislocations reaching the sample surface are identified. These dislocations satisfy the condition $\boldsymbol{g} \cdot \boldsymbol{b} \neq 0$ when $\boldsymbol{g}$ is $(11\bar{2}0)$ and b=$^1/_3\langle 11\bar{2}0\rangle$; $\boldsymbol{g} \cdot \boldsymbol{b} \neq 0$ when $\boldsymbol{g}$ is (0002) and b=$\langle 0001\rangle$; and $\boldsymbol{g} \cdot \boldsymbol{b} \neq 0$ when $\boldsymbol{g}$ is $(11\bar{2}0)$ and (0002), when $\boldsymbol{b} = {}^1/_3\langle 11\bar{2}3\rangle$. The most obvious dislocations observed for the $[1\bar{1}00]$ oriented grain, are the straight lines which propagate across the grain in the [0001] direction. These lines seem to originate from lines propagating in the $[11\bar{2}0]$ direction at the interface between the $[1\bar{1}00]$ oriented grain and its neighbour. These dislocations may be dislocations lying in the *c*-plane with a $\boldsymbol{b}$ -vector of either $\pm\,{}^1/_3\,[11\bar{2}0]$ and a line direction of $[11\bar{2}0]$, indicating they are likely to be screw dislocations. These dislocations then "bend" to take up a line direction of [0001]. A $\boldsymbol{g} \cdot \boldsymbol{b}$ analysis of the dislocations propagating in the [0001] direction suggests that these are mixed dislocations, as they are visible for $\boldsymbol{g}$ is $(11\bar{2}0)$ and $\boldsymbol{g}$ is (0001).

For the $[11\bar{2}0]$ oriented grain some dislocations satisfy the condition $\boldsymbol{g} \cdot \boldsymbol{b} \neq 0$ when $\boldsymbol{g}$ is $(1\bar{1}00)$ and $\boldsymbol{g} \cdot \boldsymbol{b} = 0$ when $\boldsymbol{g}$ is (0002). This observation is consistent with these dislocations being mixed dislocations with $\boldsymbol{b} = {}^1/_3\,[\bar{1}2\bar{1}0]$ or $\boldsymbol{b} = {}^1/_3\,[\bar{2}110]$. Other dislocations are identified with $\boldsymbol{b}$ = [0001] (edge) or $\boldsymbol{b} = {}^1/_3\,[11\bar{2}3])$ (mixed) and $\boldsymbol{b} = {}^1/_3\,[\bar{1}2\bar{1}3])$ (mixed) or $\boldsymbol{b} = {}^1/_3\,[\bar{2}113])$ (mixed). In this grain there is also evidence of dislocations along subgrain boundaries. The interaction between neighbouring WC grains corroborates previous work on the presence of dislocations along grain boundaries. The data in this chapter agrees with previous studies on defects inherent in undeformed WC grains where reports of dislocations in undeformed WC grains describe dislocations with Burgers vectors of $\langle 0001\rangle$, $^1/_3\langle 11\bar{2}0\rangle$ and $^1/_3\langle 11\bar{2}3\rangle$. Previous work suggests that undissociated dislocation with $\boldsymbol{b} = \langle 0001\rangle$ and $^1/_3\langle 11\bar{2}0\rangle$ are remains of the as-grown state and therefor expected in all as-sintered WC grains. This study reports that dislocations with b= $^1/_3\langle 11\bar{2}3\rangle$ remain in the as-sintered WC as well.

The fifth chapter is the culmination of WC analysis in this thesis. It discusses the defects induced in WC grains after indentation as revealed by ECCI and EBSD analysis. Misorientation surrounding the indent is described from EBSD maps for two different indenter tips. This chapter represents an advance in the field of indentation analysis of WC as the work in this study is the first time that ECCI is used to identify slip around indents in grains of known crystallographic orientation. The ECCI work in this chapter agrees with previous TEM data on slip systems in indented WC grains. Using ECCI presents an advantage over TEM in that damage in grains can be imaged over a wider field of view with simpler sample preparation. In the [0001] oriented grains disorientation is visible along the sides of the indent indicating deformation. Slip appears to run parallel to the trace of the $\{10\bar{1}0\}$ planes with numerous slip bands visible and this is consistent with the literature (Rowcliffe *et al.*, 1988; A. Almond, 1983). In the $[10\bar{1}0]$ oriented grains EBSD maps reveal disorientation visible along the sides of the indent, indicating deformation. Slip bands are visible in the ECCI image of this grain after indentation running in the [0001] direction with numerous slip bands visible. Slip bands with a direction of {0001} are consistent with the literature. In the $[11\bar{2}0]$ oriented grains slip runs in the {0001} direction, as was the case in the grain with a surface normal of $[10\bar{1}0]$. Slip bands in grains with a surface normal of $[11\bar{2}0]$ have been documented in the literature with the formation of dislocations with a Burgers vector of $\boldsymbol{b} = \langle 0001 \rangle$.

Additional work in this chapter focused on indenting [0001], $[1\bar{1}00]$ and $[11\bar{2}0]$ oriented grains using a spherical indenter and the three-dimensional distribution of slip around the indents was examined. Slip in the $[11\bar{2}0]$ oriented grain ran in the $[10\bar{1}0]$ direction, in agreement with previous work. Slip lines intercepting each other at 60° are visible on the [0001] oriented grain. Intercepting slip lines are consistent with previous work on slip in prismatic planes. This sample was then heated to 700° C, the change in hardness was then measured from ambient to high temperature. The basal and prismatic grains

softened as temperature increased, with a 70% reduction in hardness measured at 700° C. Increasing temperature leads to more damage in the region surrounding the indent, but this is not discussed in this thesis. The deformation data in this study indicates a preference for slip on the prismatic plane in indented WC grains.

7.2.2. Future work on tungsten carbide

Future work on WC should analyse dislocations along the most prevalent CSL boundaries to interpret the role that dislocations play in the formation of these grain boundaries. Additional work should focus on collecting ECCI data from a statistically representative group of grains from the three primary plane normals, [0001], [$10\bar{1}0$] and [$11\bar{2}0$]. Collecting this data would cement the role that ECCI and EBSD play together in the interpretation of crystallographic defects in WC grains.

7.3. Twinned diamonds

7.3.1. Conclusions on twinned diamonds

Chapter 6 presents cathodoluminescence and EBSD data documenting the crystallographic orientation of twinned gem-quality diamonds. The twinned diamonds are all composed of two sibling twins with around 180° rotation in Euler angles between the siblings. CL is helpful in understanding the initial twin nucleation and distinct periods of crystallization in the diamond's history while EBSD is used to corroborate CL data like in diamond 617 where zoning is visible in both techniques. This study reveals that the twinning plane is not linear, but jagged, corroborating previous research indicating that these are not true contact twins, rather they contain some intergrowths. EBSD confirms that these are undeniable twins as the plane separating the two siblings is a twin CSL grain boundary. CL and EBSD together are powerful tools for characterizing the

twinning plane and growth mechanism in diamonds and this work describes the novel use of these techniques to characterize the twinning plane in macles.

7.3.2. Future work on twinned diamonds

Future work on twinned diamonds should examine the strain on either side of the twinning plane using EBSD pattern matching. As discussed in chapter 3, pattern matching allows for improved orientation precision with three times the resolution of traditional Hough transform based analysis. If very small changes in orientation, such as dislocations are visible in WC grains using pattern matching, theoretically the dislocations that lead to twinning can be revealed as well. Pattern matching could also allow investigation of the initial diamond seed from which subsequent growth commenced.

Cathodoluminescence hyperspectral imaging could correlate the source of cathodoluminescence with regions of distinct growth. This technique could also be used to understand the origin of the cathodoluminescence signal in different regions in the diamond. These analyses would be beneficial in interpreting the twinning mechanism and associated strain in macles.

List of Figures

Chapter 1

Figure 1. A BSEI of WC grains embedded in a cobalt binder 14
Figure 2. Introduction to macles..... 17

Chapter 2

Figure 1. Model of dislocations in a simple cubic lattice. 22
Figure 2. Crystallography of hexagonal materials.....24
Figure 3. Slip on the primary prismatic plane 26
Figure 4. Ball and stick model of the diamond crystal structure 27
Figure 5. Crystallography of an isometric system. 29
Figure 6. Indenter geometries.....30
Figure 7. A simplified representation of the polished twinning plane 31
Figure 8. Information revealed by backscattered electrons 33
Figure 9. Introduction to EBSD configuration and EBSP.....36
Figure 10. Introduction to EBSD maps 38
Figure 11. Introduction to pattern matching maps..... 40
Figure 12. CL image of a macle 41

Chapter 3

Figure 1. SEI of a WC sample..... 46
Figure 2. ECCI and EBSD map of a randomly oriented grain..... 48
Figure 3. IPF map and CSL grain boundaries 51
Figure 4. Identifying grains close to the **1100** sample normal 52
Figure 5. Dislocations as revealed by ECCI in 3 grains 53
Figure 6. Dislocations as revealed by ECCI in a **1120** oriented grain 54
Figure 7. Comparison of refined accuracy data and pattern matching results .56
Figure 8. Low magnification ECCI revealing WC subgrains 59

Chapter 4

Figure 1. Identifying WC grains close to the **0001** sample normal.....67
Figure 2. Dislocations as revealed by ECCI in three grains 68

Figure 3. Dislocations as revealed by ECCI in a **0001** oriented grain..... 69
Figure 4. Dislocations as revealed by ECCI in a **1100** oriented grain 71
Figure 5. Dislocations as revealed by ECCI in a **1120** oriented grain 73
Figure 6. Dislocations revealed by EBSD using pattern matching.....76

Chapter 5

Figure 1. Identifying **0001**, **1100**, **1120** oriented grains 81
Figure 2. Indentation of the first **0001** oriented grain..... 84
Figure 3. Indentation of the second **0001** oriented grain..... 86
Figure 4. Indentation of the first **1010** oriented grain..... 89
Figure 5. Indentation of the second **1010** oriented grain..... 92
Figure 6. Indentation of the first **1120** oriented grain.....95
Figure 7. Indentation of the second **1120** oriented grain..... 98
Figure 8. Indentation of WC followed by ECCI analysis and FIB milling..... 100

Chapter 6

Figure 1. A twinned diamond's crystallographic faces 105
Figure 2. Optical micrographs of the diamonds in this study..... 105
Figure 3. ECCI of the twinning plane..... 106
Figure 4. The crystallography of twinning 107
Figure 5. The relationship between an octahedron and a triangular crystal face. 108
Figure 6 EBSD and CL data from diamond 617 111
Figure 7 EBSD and CL data from diamond 596 113
Figure 8 EBSD and CL data from diamond 625 115
Figure 9 CL spectra from diamonds 596, 625 and 617 115

List of Tables

Chapter 3

Table 1. Euler angle table for the parent grain and subgrain.....54

Chapter 4

Table 1. Summarizing $\boldsymbol{g} \cdot \boldsymbol{b}$ analysis for grain shown in Figure 3. 70
Table 2. Summarizing $\boldsymbol{g} \cdot \boldsymbol{b}$ analysis for grain shown in Figure 4. 72
Table 3. Summarizing $\boldsymbol{g} \cdot \boldsymbol{b}$ analysis for grain shown in Figure 5. 74

Chapter 6

Table 1. Absolute value of Euler angles between the two twins 117

References

A. Almond, E. (1983). *Science of Hard Materials*, Vol. edited by G.J. Viswanadham R.K., Rowcliffe D.J., pp. 517–561. Boston, MA: Springer.

Bachmann, F., Hielscher, R. & Schaeben, H. (2010). *Solid State Phenom.* **160**, 63–68.

Baumgart, F. (2000). *Injury*. **31**,.

Bestmann, M., Pennacchioni, G., Frank, G., Göken, M. & de Wall, H. (2011). *J. Struct. Geol. - J STRUCT GEOL.* **33**, 169–186.

Bilby, B. A. (1954). *Acta Crystallogr.* **7**, 522–523.

Bolton, J. D. & Redington, M. (1980). *J. Mater. Sci.* **15**, 3150–3156.

Bounhoure, V., Lay, S., Charlot, F., Antoni-Zdziobek, A., Pauty, E. & Missiaen, J. M. (2014). *Int. J. Refract. Met. Hard Mater.* **44**, 27–34.

Britannica, T. E. of E. B. (2017). Mohs hardness Encyclopedia Britannica.

Butler, J. & Oleynik, I. (2008). *Philos. Trans. A. Math. Phys. Eng. Sci.* **366**, 295–311; discussion 311.

Cahn, R. W. (1954). *Adv. Phys.* **3**, 363–445.

Chen, D. & Kuo, J.-C. (2010). *Ultramicroscopy*. **110**, 1297–1305.

Chen, Y. H., Park, S. U., Wei, D., Newstadt, G., Jackson, M. A., Simmons, J. P., De Graef, M. & Hero, A. O. (2015). *Microsc. Microanal.* **21**, 739–752.

Chinn, R. E. (2009). *Adv. Mater. Process.* 29–31.

Delanoë, A., Lay, S. & Missiaen, J.-M. (2007). *Mater. Sci. Forum - MATER SCI FORUM*. **534–536**, 1213–1216.

Duszová, A., Halgaš, R., Bľanda, M., Hvizdoš, P., Lofaj, F., Dusza, J. & Morgiel, J. (2013). *J. Eur. Ceram. Soc.* **33**, 2227–2232.

Edington, J. (1976). *Practical Electron Microscopy in Materials Science*, Vol. p. Eindhoven: Philips Technical Library.

Edwards, P. R., Jagadamma, L. K., Bruckbauer, J., Liu, C., Shields, P., Allsopp, D., Wang, T. & Martin, R. W. (2012). *Microsc. Microanal.* **18**, 1212–1219.

Edwards, P. R. & Martin, R. W. (2011). *Semicond. Sci. Technol.* **26**, 064005.

Everson, M. P., Tamor, M. A., Scholl, D., Stoner, B. R., Sahaida, S. R. & Bade, J.

P. (1994). *J. Appl. Phys.* **75**, 169–172.

Farooq, M.U.; Klement, U. (2004). *J. Microsc.* **213**, 306–312.

French, D.N. and Thomas, D. A. (1965). *Trans. Met. Soc. AIME*. **233**,.

Friedel, G. (1926). Lecons de Crystallographie Paris: Berger- Levrault.

Friedrich, T., Bochmann, A., Dinger, J. & Teichert, S. (2018). *Ultramicroscopy*. **184**, 44–51.

Fritsch, E. (1998). *Nat. Diamonds*. 23–47.

Gaft, M., Reisfeld, R. & Panczer, G. (2005). Modern Luminescence Spectroscopy of Minerals and Materials Verlag Berlin Heidelberg: Springer.

Gee, M., Mingard, K. & Roebuck, B. (2009). *Int. J. Refract. Met. Hard Mater.* **27**, 300–312.

Goldstein, J. I., Newbury, D. E., Echlin, P., Joy, D. C., Fiori, C. & Lifshin, E. (1981). *Scanning Electron Microscopy and X-Ray Microanalysis*, Vol. p. Boston, MA: Springer.

Greenwood, R. M., Loretto, M. H. & Smallman, R. E. (1982). *Acta Metall.* **30**, 1193–1196.

Gutierrez-Urrutia, I. & Raabe, D. (2012). *Scr. Mater.* **66**, 343–346.

Hall, E. O. (1951). *Proc. Phys. Soc. Sect. B*. **64**, 742–747.

Hibbs, M. K. & Sinclair, R. (1981). *Acta Metall.* **29**, 1645–1654.

Hielscher, R., Bartel, F. & Britton, T. (2019). *Microsc. Microanal.* **25**, 1954–1955.

Hielscher, R. & Schaeben, H. (2008). *J. Appl. Crystallogr.* **41**, 1024–1037.

Hirth, J. P., Lothe, J. & Lehmann, S. (1992). Theory of Dislocations.

Hull, D. & Bacon, D. (2001*a*). *Introduction to Dislocations (Fourth Edition)*, Vol. edited by D. Hull & D.J. Bacon, p. ix. Oxford: Butterworth-Heinemann.

Hull, D. & Bacon, D. J. (2001*b*). *Introduction to Dislocations (Fourth Edition)*, Vol. edited by D. Hull & D.J. Bacon, pp. 1–21. Oxford: Butterworth-Heinemann.

Hull, D. & Bacon, D. J. (2001*c*). *Introduction to Dislocations (Fourth Edition)*, Vol. edited by D. Hull & D.J. Bacon, pp. 42–61. Oxford: Butterworth-

Heinemann.

Humphreys, F. J., Bate, P. S. & Hurley, P. J. (2001). *J. Microsc.* **201**, 50–58.

Jablon, B. M., Mingard, K., Winkelmann, A., Naresh-Kumar, G., Hourahine, B. & Trager-Cowan, C. (2020). *Int. J. Refract. Met. Hard Mater.* **87**, 105159.

Jablon, B. M., Mingard, K., Winkelmann, A., Naresh-Kumar, G., Hourhaine, B. & Trager-Cowan, C. (2019). *Int. J. Refract. Met. Hard Mater.* 105159.

Jablon, B. M. & Navon, O. (2016). *Earth Planet. Sci. Lett.* **443**,.

Johannesson, T. & Lehtinen, B. (1971). *Philos. Mag.* **24**, 1079–1085.

Johannesson, T. & Lehtinen, B. (1973). *Phys. Status Solidi*. **16**, 615–622.

Joy, D. C., Newbury, D. E. & Davidson, D. L. (1982). *J. Appl. Phys.* **53**,.

Kim, H. T., Kim, J. S. & Kwon, Y. S. (2005). *Proceedings. The 9th Russian-Korean International Symposium on Science and Technology, 2005. KORUS 2005.*, Vol. pp. 458–461.

Kim, S., Han, S. H., Park, J. K. & Kim, H. E. (2003). *Scr. Mater.* **48**, 635–639.

Kong, B. H., Sun, Q., Han, J., Lee, I. H. & Cho, H. K. (2012). *Appl. Surf. Sci.* **258**, 2522–2528.

Kumar, V., Fang, Z. Z., Wright, S. I. & Nowell, M. M. (2006). *Metall. Mater. Trans. A Phys. Metall. Mater. Sci.* **37**, 599–607.

Kurat, G. & Dobosi, G. (2000). *Mineral. Petrol.* **69**, 143–159.

Kurlov, A. S. & Gusev, A. I. (2013). Tungsten Carbides: Structure, Properties and Application in Hardmetals.

L'hôte, G., Lafond, C., Steyer, P., Deschanel, S., Douillard, T., Langlois, C. & Cazottes, S. (2019). *Scr. Mater.* **162**, 103–107.

Lay, S. (2013). *Int. J. Refract. Met. Hard Mater.* **41**, 416–421.

Lay, S., Delavignette, P. & Vicens, J. (1985). **53**,.

Lay, S., H. Allibert, C., Christensen, M. & Wahnström, G. (2008). *Mater. Sci. Eng. A*. **486**, 253–261.

Lay, S. & Loubradou, M. (2003). *Philos. Mag.* **83**, 2669–2679.

Lay, S. & Missiaen, J.-M. (2014). *Comprehensive Hard Materials*, Vol. edited by D. Mari, L. Miguel & C. Nebel, pp. 91–117. Newnes.

Lee, H. C. & Gurland, J. (1978). *Mater. Sci. Eng.* **33**, 125–133.

Luyckx, S. B. (1970). *Acta Metall.* **18**, 233–236.

Machado, W., Moore, M. & Yacoot, A. (1998). *J. Appl. Crystallogr. - J APPL CRYST.* **31**, 777–782.

Mattheiss, L. F. & Hamann, D. R. (1984). *Phys. Rev. B.* **30**, 1731–1738.

Mingard, K. P. & Gee, M. G. (2007). *Wear*. **263**, 643–652.

MM Khrushchov, E. B. (1951). *Ind. Diamonds Rev.*

Moore, M. & Lang, A. R. (1974). *J. Cryst. Growth*. **26**, 133–139.

Naresh-Kumar, G., Hourahine, B., Edwards, P. R., Day, A. P., Winkelmann, A., Wilkinson, A. J., Parbrook, P. J., England, G. & Trager-Cowan, C. (2012). *Phys. Rev. Lett.* **108**, 1–5.

Nelson, S. A. (2013). Twinning, Polymorphism, Polytypism, Pesudomorphism.

Nolze, G. & Hielscher, R. (2016). *J. Appl. Crystallogr.* **49**, 1786–1802.

Nolze, G., Hielscher, R. & Winkelmann, A. (2017). *Cryst. Res. Technol.* **52**, 1–24.

Nolze, G., Winkelmann, A. & Boyle, A. (2015). *Ultramicroscopy*.

Orlov, Y. L. (1977). The Mineralogy of the Diamond New York: John Wiley.

Pascal, E., Hourahine, B., Naresh-Kumar, G., Mingard, K. & Trager-Cowan, C. (2018). *Mater. Today Proc.* **5**, 14652–14661.

Peck, D. & Ostrander, A. (2018). Crystallography: The Hexagonal System.

Pellan, M., Lay, S., Missiaen, J. M., Norgren, S., Angseryd, J., Coronel, E. & Persson, T. (2015). *J. Am. Ceram. Soc.* **98**, 3596–3601.

Picard, Y. N., Twigg, M. E., Caldwell, J. D., Eddy, C. R., Mastro, M. A. & Holm, R. T. (2009). *Scr. Mater.* **61**, 773–776.

Porat, R., Berger, S. & Rosen, A. (1996). *Nanostructured Mater.* **7**, 429–436.

Prakash, L. J. (1995). *Int. J. Refract. Met. Hard Mater.* **13**, 257–264.

Randle, V. (2000). *Electron Backscatter Diffraction in Materials Science*, Vol. edited by A. Schwartz, M. Kumar & B. Adams, pp. 19–30.

Roebuck, B. & A. Almond, E. (1988). *Int. Mater. Rev.* **33**, 90–112.

Roebuck, B., Klose, P. & Mingard, K. P. (2012). *Acta Mater.* **60**, 6131–6143.

Rowcliffe, D. J., Jayaram, V., Hibbs, M. K. & Sinclair, R. (1988). *Mater. Sci. Eng.*

A. **105–106**, 299–303.

Ruedl, E., Delavignette, P. & Amelinckx, S. (1962). *J. Nucl. Mater.* **6**, 46–68.

Sakharova, N. A., Fernandes, J. V., Antunes, J. M. & Oliveira, M. C. (2009). *Int. J. Solids Struct.* **46**, 1095–1104.

Schwarzer, R. A., Field, D. P., Adams, B. L., Kumar, M. & Schwartz, A. J. (2009). *Electron Backscatter Diffraction in Materials Science*, Vol. edited by A.J. Schwartz, M. Kumar, B.L. Adams & D.P. Field, pp. 1–20. Boston, MA: Springer US.

Seret, A., Moussa, C., Bernacki, M., Signorelli, J. & Bozzolo, N. (2019). *J. Appl. Crystallogr.* **52**, 548–563.

Shaffner, T. J. & Van Veld, R. D. (1971). *J. Phys. E.* **4**, 633–637.

Simkin, B. A. & Crimp, M. A. (1999). *Ultramicroscopy*. **77**, 65–75.

Smith, R. L. & Sandland, G. E. (1922). *Proc. Inst. Mech. Eng.* **1**, 623–641.

Sunagawa, I. (1984).

TACA Tungsten carbide hardfacts fact sheet.

Takahashi, T. & Freise, E. J. (1965). *Philos. Mag. A J. Theor. Exp. Appl. Phys.* **12**, 1–8.

Tamor, M. A. & Everson, M. P. (1994). *Mater. Res. Soc. Symp. - Proc.* **349**, 391–402.

Tappert, R. & Tappert, M. C. (2011). Diamonds in Nature Springer-Verlag Berlin Heidelberg.

Thomsen, K., Mehnert, K., Trimby, P. W. & Gholinia, A. (2017). *Ultramicroscopy*. **182**, 62–67.

Trimby, P. W. & Prior, D. J. (1999). *Tectonophysics*. **303**, 71–81.

Vicens, J., Laurent-Pinson, E., Chermant, J. L. & Nouet, G. (1988). *Le J. Phys. Colloq.* **49**, C5-271-C5-276.

Wang, X., Fang, Z. Z. & Sohn, H. Y. (2008). *Int. J. Refract. Met. Hard Mater.* **26**, 232–241.

Weidow, J. (2010). Effect of metal and cubic carbide additions on interface chemistry, phase composition and grain growth in WC-Co based

cemented carbides.

Weidow, J. & Andrén, H.-O. (2011). *Int. J. Refract. Met. Hard Mater.* **29**, 38–43.

Wild, C., Herres, N. & Koidl, P. (1990). *J. Appl. Phys.* **68**, 973–978.

Wilkinson, A. J. & Hirsch, P. B. (1997). *Micron*. **28**, 279–308.

Williams, D. B. & Carter, C. B. (2009). *Transmission Electron Microscopy: A Textbook for Materials Science*, Vol. pp. 441–461. Boston, MA: Springer US.

Winkelmann, A., Jablon, B. M., Tong, V. S., Trager-Cowan, C. & Mingard, K. P. (2020). *J. Microsc.* **277**, 79–92.

Wright, S. I., Nowell, M. M. & Field, D. P. (2011). *Microsc. Microanal.* **17**, 316–329.

Yacobi, B. G. & Holt, D. B. (1990). *Cathodoluminescence Microscopy of Inorganic Solids*, Vol. p. Boston, MA: Springer.

Yacoot, A., Moore, M. & Machado, W. G. (1998). *J. Appl. Crystallogr.* **31**, 767–776.

Yu, H., Liu, J., Karamched, P., Wilkinson, A. J. & Hofmann, F. (2019). *Scr. Mater.* **164**, 36–41.

Zaefferer, S. & Elhami, N. N. (2014). *Acta Mater.* **75**, 20–50.

Zhimin, Y., Changhui, M., Jun, D., Daniel, M., Yannick, C., Serge, H. & Martin, H. (2000). *MRS Proc.* **634**, B8.7.1.

Zhong, Y., Zhu, H., Shaw, L. L. & Ramprasad, R. (2011). *Acta Mater.* **59**, 3748–3757.

Zhou, Weilie and Wang, Z. L. (2006). *Scanning Microscopy for Nanotechnology*, Vol. pp. 41–75.